2019

Efficient response models for rigid airfield pavement systems design

Adel Rezaei Tarahomi
Iowa State University

Efficient response models for rigid airfield pavement systems design

by

Adel Rezaei Tarahomi

A dissertation submitted to the graduate faculty

in partial fulfillment of the requirements for the degree of

DOCTOR OF PHILOSOPHY

Major: Civil Engineering (Intelligent Infrastructures Engineering)

Program of Study Committee:
Halil Ceylan, Major Professor
Ashraf Bastawros
Bora Cetin
In-Ho Cho
Kasthurirangan Gopalakrishnan
Kristen Sara Cetin
Sunghwan Kim

The student author, whose presentation of the scholarship herein was approved by the program of study committee, is solely responsible for the content of this dissertation. The Graduate College will ensure this dissertation is globally accessible and will not permit alterations after a degree is conferred.

Iowa State University

Ames, Iowa

2019

DEDICATION

To my wonderful wife and best friend, Zahra, who always inspires me with love, kindness, patient, and confidence.

To my beloved father and mother whose endless love, encouragement, prays of day and night, and supports make me thankful and satisfied with my achievements.

TABLE OF CONTENTS

Page

LIST OF FIGURES

Page

LIST OF TABLES

Page

NOMENCLATURE

AAE	Absolute average error
AI	Artificial intelligence
ANN	Artificial neural network
CDF	Cumulative damage factor
CGB	Conjugate Gradient_ Powell-Beale Restarts
CGF	Conjugate Gradient_Fletcher-Reeves Update
CGP	Conjugate Gradient_ Polak-Ribiére Update
DF	Design factor
ETG	Equivalent temperate gradient
FAA	Federal aviation administration
FAARFIELD	FAA rigid and flexible iterative elastic layered design
FEAFAA	Finite element analysis-FAA
FEM	Finite element model
LLNL	Lawrence Livermore National Laboratory
LM	Levenberg-Marquardt
MAE	Maximum absolute error
MEPDG	Mechanistic-Empirical Pavement Design Guide
MSE	Mean squared error
NCHRP	National Cooperative Highway Research Program

NSI	Normalized sensitivity index
OAT	One at a time
OSS	One-step Secant
PCC	Portland cement concrete
RMSE	Root mean squared error
SA	Sensitivity analysis
TCDF	Total cumulative damage factor
ΔT	Temperature difference
$\sigma_{XX\text{-}Max\text{-}Top\text{-}Tens.}$	Maximum tensile stress responses at top of the slab in *X* direction
$\sigma_{YY\text{-}Max\text{-}Top\text{-}Tens.}$	Maximum tensile stress responses at top of the slab in *Y* direction
$\sigma_{1\text{-}Max\text{-}Top\text{-}Tens.}$	Maximum principal tensile stress responses at top of the slab
$\sigma_{XX\text{-}Max\text{-}Bottom\text{-}Tens.}$	Maximum tensile stress responses at bottom of the slab in *X* direction
$\sigma_{YY\text{-}Max\text{-}Bottom\text{-}Tens.}$	Maximum tensile stress responses at bottom of the slab in *Y* direction
$\sigma_{1\text{-}Max\text{-}Bottom\text{-}Tens.}$	Maximum principal tensile stress responses at bottom of the slab
σ_{xx}	Normal stress in *X* direction
σ_{yy}	Normal stress in *Y* direction
σ_{zz}	Normal stress in *Z* direction
σ_{xy}	Shear stress at *XY* plane
σ_{yz}	Shear stress at *YZ* plane
σ_{zx}	Shear stress at *ZX* plane

σ_{Mises}	Von Mises stress
σ_1	Maximum principal stress
σ_2	Minimum principal stress
Θ_p	Corresponding principal stress angle to σ_1 and σ_2
Θ_g	Loading gear angle
$\mathbf{B_1}$, $\mathbf{B_2}$, $\mathbf{B_3}$	Artificial neural networks (ANNs) biases matrices
$\mathbf{LW_1}$	ANNs hidden layer one's weight matrix
$\mathbf{LW_2}$	ANNs hidden layer two's weight matrix
IW	ANNs input weight matrix
Tansig	Hyperbolic tangent sigmoid transfer function
Inputsnor	Normalized inputs between (-1, 1)
Y	Network output of interest
X_k	Baseline value of input k
ΔX_k	Change in input k about the base line
ΔY_j	Change in output J corresponding to ΔX_k
Y_K	Baseline value of output J
n	Data set's element number
j	Case number in the data set
$y^{solution}$	FEAFAA outputted critical pavement responses
$y^{prediction}$	ANN models predicted critical pavement responses
R	Number of elements in input vector

S_1	Number of neurons in first hidden layer
S_2	Number of neurons in second hidden layer

ACKNOWLEDGMENTS

I would like to express my sincere gratitude to my advisor Prof. Halil Ceylan for the continuous support of my Ph.D. study and related research, for his patience, motivation, and immense knowledge. I am particularly grateful for the assistance and support given by Dr. Sunghwan Kim whose guidance helped me in all the time. I would also like to thank Dr. Kasthurirangan Gopalakrishnan, for his advice and assistance in starting of this study and helping my progress.

I should thank Orhan Kaya who had a great contribution to this research and helped me to carry on the finite element simulations for this study.

I thank my nice friend, Ramin Giahi for his great help and collaboration in doing the most important part of this study and for his great knowledge in optimization which helped me accomplishing the last chapter of this study.

I gratefully acknowledge the Federal Aviation Administration (FAA) for supporting and funding this study. My special appreciation is for Dr. David R. Brill who supervised this study and enriched this research by his priceless comments and guidance.

I would like to thank my committee members, In-Ho Cho, Ashraf Bastawros, Kristen Sara Cetin, and Bora Cetin for their guidance and support throughout the course of this research.

In addition, I would also like to thank my friends, colleagues, the department faculty and staff for making my time at Iowa State University a wonderful experience.

ABSTRACT

The Federal Aviation Administration (FAA) has recognized that its current rigid pavement design model, reflecting a single slab loaded at one edge by a single aircraft landing gear, does not adequately account for top-down cracking, meaning that one of the major observed failure modes for rigid pavements is poorly accounted for in the rigid pavement design procedure FAA Rigid and Flexible Iterative Elastic Layer Design (FAARFIELD). To expand the FAARFIELD design model beyond the currently-used reduced one-slab model, since practical alternatives to running the 3D-FEM stress computation as client software are needed, this study seeks to fill this research gap by developing a surrogate computational response model or procedure (suitable for implementation in FAARFIELD 1.4-TDC) that returns a close estimate of the top-down bending stress computed by the 3D-FE model for combined vehicle and temperature loading of rigid airport pavements.

A synthetic database has been generated by conducting batch runs of FAA finite-element analysis software (FEAFAA 2.0), and this database contains data from thousands of multiple-slab rigid pavement cases with associated critical tensile stresses at the slab top induced by either mechanical-only or combined mechanical and temperature loading, with critical responses that include tensile stresses in both x and y directions along with principal tensile stresses. Artificial neural networks (ANNs) have been employed to develop a surrogate top-down slab bending-stress prediction model using non-linear input-output mapping of the database. Surrogate response models were trained for each of the Airbus and Boeing aircraft provided in the FEAFAA 2.0 library. This has been accomplished by developing software for automating entry of the database obtained by

conducting FEAFAA batch runs, to train the ANN models using different architectures and algorithms, to control the ANN input parameters, and to collect training results. Both accuracy and robustness of the models were validated through independent testing and sensitivity testing. A new ANN tool for rapid analysis of nine-slab rigid airfield pavements that replicates the top-down critical stresses obtained from direct finite element solutions was developed. In addition, a new airfield pavement design approach was proposed which employs Bayesian optimization along with the trained ANN models.

CHAPTER 1. INTRODUCTION

Background

Airport pavements are designed to withstand repeated loadings imposed by aircraft, to resist detrimental effects of such traffic, and to endure deterioration induced by adverse weather conditions (e.g., extreme hot or cold weather) and other influences. Since a typical civil airport serves a fleet of aircraft with different weights and gear configurations, the airport pavement must thus be designed to withstand repeated traffic loading by not just the heaviest aircraft, but aircraft over a very wide entire range [1], over a span of many years. Historical airport pavement design methodologies have typically been based on simplified formulas (California Bearing Ratio (CBR), Westergaard equations) combined with observations of field performance. With the arrival of New Large Aircraft (NLA) (e.g., B747, B777, and A380-800) and associated pavement design challenges, including increasing aircraft weights and complex gear configurations, the FAA has adopted layered elastic theory for flexible airport pavement design and three-dimensional finite element (3D-FE) procedures for rigid airport pavement design. These mechanistic-empirical design methodologies, implemented in the FAA Rigid and Flexible Iterative Elastic Layer Design (FAARFIELD) program, are robust and can be adapted to addressing future gear configurations without modifying the underlying procedures [1].

For rigid pavement design, FAARFIELD uses a 3D-FE computer program called NIKE3D_FAA to compute the maximum horizontal stress at the bottom edge of a Portland Cement Concrete (PCC) slab as a pavement structural life predictor. NIKE3D_FAA is a modification of the NIKE3D program originally developed by the Lawrence Livermore National Laboratory (LLNL) of the U.S. Department of Energy [2], [3].

By limiting horizontal stress at the bottom of the PCC slab, cracking of the surface layer, (the only rigid pavement failure mode considered by FAARFIELD), can be controlled; FAARFIELD does not currently consider subbase and subgrade layer failure for rigid airport pavements. For a given aircraft traffic mix over a particular subgrade/subbase, FAARFIELD provides a value for the required rigid pavement slab thickness [4] The FAA has also developed FEAFAA (Finite Element Analysis – FAA), that makes use of NIKE3D as a stand-alone tool for 3D FE analysis of multiple-slab rigid airport pavements and overlays. It computes accurate responses (deflections, stresses, and strains) of rigid pavements to individual aircraft landing gear loads. While FEAFAA is a research and analysis tool, it is not a full-fledged design tool because it lacks the empirical components of FAARFIELD, and FEAFAA allows more options and greater configurability than the standard 3D-FE mesh implemented in FAARFIELD.

Motivation

The FAA's current rigid pavement design model that considers only a single slab loaded at one edge by a single aircraft gear does not adequately account for top-down cracking, so one of the major observed rigid-pavement failure modes is poorly accounted for in the FAARFIELD rigid design procedure. To account for the influence of top-down cracking in thickness design, a research version of the FAARFIELD design software has been developed in which the single-slab three-dimensional finite-element (3D-FE) response model is replaced by a 4-slab 3D-FE model with initial temperature curling and variable joint spacing (FAARFIELD 1.4-TDC). However, the long and unpredictable run times associated with the 4-slab model and curled slabs make routine design with this model impractical. To expand the FAARFIELD design model beyond the current one-slab model, the FAA is seeking practical alternatives to running the 3D-FEM stress computation as client software.

Artificial intelligence (AI) based alternatives such as artificial neural networks (ANNs) have great potential for producing accurate stress predictions using only a fraction of the time of those produced by traditional FE-based design programs, so ANNs could be practical alternatives to full 3D-FE computation that requires excessively long computation times.

ANNs were selected as a first choice [5], [6] for developing a surrogate model using AI techniques, and use of ANNs as a faster and robust alternative to time-consuming and complex FE-based structural modeling has been successfully demonstrated in airport and highway concrete pavement analysis and design applications [7]–[9]. Since this concept of surrogate response modeling has provided rapid solutions in terms of concrete pavement critical responses (close estimates of ISLAB 2000 solutions) for various combinations of input parameters, it was also adopted in the development of Mechanistic-Empirical Pavement Design Guide (MEPDG) [10], presently marketed as AASHTOWare Pavement ME [11], ANNs were the first choice for this project because of their versatility and proven success in surrogate pavement response modeling.

The significant potential of AI techniques in solving resource-intensive complex problems has led to increased interest in using such methods in different engineering areas, especially in civil engineering fields such as structural engineering, environmental and water resources engineering, traffic engineering, geotechnical engineering, and pavement engineering. Over recent decades, use of ANNs as an AI technique has become popular both in research activities and in commercial applications.

ANNs have been used to address a wide variety of pavement engineering issues associated with design, analysis, distress evaluation, performance, maintenance, rehabilitation, and management of both highway and airport pavements (flexible, rigid, and

composite). Utilizing ANN in a number of research studies related to the pavement engineering field has demonstrated that ANN shows promise for use in investigating, modelling, and generally achieving better understanding of complex and non-linear pavement engineering problems and mechanisms, even for some not yet well-understood or formulated [7], [8], [12]–[17].

Neural networks have been found to be very reliable and versatile computational tools for determining and predicting future conditions and performance of existing pavement systems, taking into account maintenance and rehabilitation decision-making actions for deteriorated pavement sections, developing cost-effective prediction models to estimate future condition of pavement sections, predicting pavement layer and surface properties, and understanding and characterizing both Portland cement and asphalt concrete mixture design and behavior [5], [6]. Moreover, the capability of ANN-based surrogate response models for successfully computing all components of tensile stress as well as deflections at the bottom of jointed concrete airfield pavements has been illustrated through many studies [7], [8], [15], [16]. Some of the input parameters used in those response models were type, level, and location of an applied gear load, along with slab thickness, slab modulus, subgrade support, pavement temperature gradient, and load transfer efficiencies of the joints.

Among the various types of ANNs, backpropagation ANNs are popular learning methods capable of handling complexity of large learning problems. The term "backpropagation network" actually refers to a multi-layered, feed-forward neural network trained using an error backpropagation algorithm (see Figure 1.1). The learning process performed by this algorithm is called backpropagation learning and is mainly an error-minimization technique [18]–[22].

As with many ANNs, connection weights in backpropagation ANNs are initially randomly selected, and inputs from the mapping examples are propagated forward through each layer of the network to eventually emerge as outputs. Errors between those outputs and the known correct answers are then propagated backward through the network and connection weights individually adjusted to reduce the error. After many examples (training patterns) have been propagated through the network many times, the mapping function becomes learned within some specified error tolerance; this is called supervised learning because the network must be shown the correct answers in order for it to learn. Backpropagation networks excel at data modeling because of their superior function approximation capabilities [18].

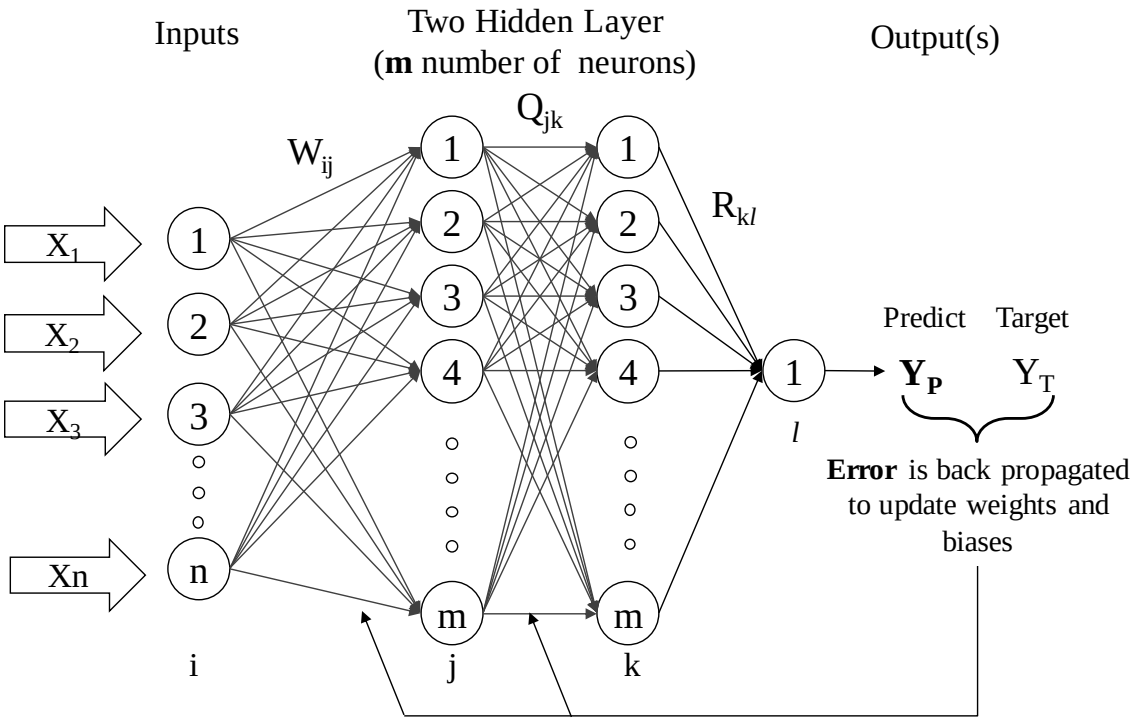

Figure 1.1 *Schematic of a typical backpropagation ANN architecture.*

Many previous examples [5], [6], [8], [9], [12], [13], [17], [23] where ANNs were successfully used in pavement engineering demonstrate that the deployment of ANN

algorithms is a practical alternative to 3D FE solutions for predicting critical top-down tensile stresses, and can reduce computer run time for multiple-slab simulation to mere seconds. Incorporation of the ANN surrogate response models in the pavement design process can also significantly reduce iteration time for calculation of critical responses for each type of aircraft involved in mixed aircraft traffic loading and simultaneously help with implementing the whole design process more efficiently.

Research Objectives

The objective of this research was to develop a surrogate computational response model or procedure (suitable for implementation in FAARFIELD 1.4-TDC) capable of returning a close estimate of the top-down bending stress computed by NIKE3D both for mechanical-only and combined vehicle and temperature loading of rigid airport pavements. This will enable faster 3D-FE computation of design stresses in FAARFIELD 1.4-TDC, making it suitable for use in routine design.

The overall research approach involves the following six major steps: (1) generate a synthetic database through batch runs of FEAFAA 2.0 (9-slab model); (2) employ ANN to develop a surrogate top-down slab-bending stress-prediction model through nonlinear input-output mapping of the database; (3) verify the accuracy and robustness of the surrogate response prediction model; (4) perform model evaluation and validation; (5) develop a new ANN tool for analyzing a multiple slab (9-slab) model for rigid airfield pavements, including all types of aircraft included in FEAFAA 2.0 software; (6) demonstrate how the developed ANN model could actually be implemented into airport rigid pavement design along with reliability concept.

Dissertation Organization

This dissertation, presenting detailed steps for developing surrogate critical response models based on a synthetic database of 3D-FEM solutions for rigid airfield pavements, includes six chapters:

Chapter 1 (Introduction) presents background, motivation, research objectives, and dissertation organization.

Chapter 2 (Sensitivity Quantification of Airport Concrete Pavement Stress Responses Associated with Top-Down and Bottom-Up Cracking) discusses sensitivity evaluation of the critical responses in rigid airfield pavements and also presents the most significant NIKE3D-FAA input parameters.

Chapter 3 (Development of Rapid Analysis Tool for Rigid Airfield Pavement Systems) discusses database and ANN model development approaches, and tools and methods developed or utilized in this study.

Chapter 4 (ANN Model Accuracy Assessments) describes accuracy assessment criteria and performance results obtained by the ANN response models and discusses the effects of rigid pavement's most important characteristics on the critical tensile stresses predicted by the ANN response models.

Chapter 5 (Reliability-Based Design Optimization of Airports Concrete Pavement) proposed new designing approaches for airfield concrete pavements. In this chapter ANN is used with simulation optimization to find the optimum thickness by given reliability level.

Chapter 6 (Conclusions, Recommendations and Contributions of This Study) presents a summary of the research approach used and the key findings of this study, along with recommendations for future study and the contribution of this study to the pavement-engineering field.

References

[1] FAA, “Advisory Circular: Airport Design,” Federal Aviation Administration (FAA), 2014.

[2] D. R. Brill, “Development of Advanced Computational Models for Airport Pavement Design,” no. August, 1998.

[3] D. R. Brill, “Field verification of a 3D finite element rigid airport pavement model,” 2000.

[4] FAA, “Airport Pavement Design and Evaluation. AC 150/5320-6E,” 2009.

[5] K. Gopalakrishnan, H. Ceylan, and N. O. Attoh-Okine, *Intelligent and soft computing in infrastructure systems engineering: recent advances*, vol. 259. Springer, 2009.

[6] H. Ceylan, M. B. Bayrak, and K. Gopalakrishnan, “Neural networks applications in pavement engineering: A recent survey,” *Int. J. Pavement Res. Technol.*, vol. 7, no. 6, pp. 434–444, 2014.

[7] H. Ceylan, E. Tutumluer, and E. Barenberg, “Artificial Neural Networks for Analyzing Concrete Airfield Pavements Serving the Boeing B-777 Aircraft,” *Transp. Res. Rec. J. Transp. Res. Board*, vol. 1684, no. 99, pp. 110–117, 1999.

[8] H. Ceylan, “Analysis and design of concrete pavement systems using artificial neural networks,” University of Illinois at Urbana-Champaign, 2002.

[9] H. Ceylan, E. Tutumluer, and E. Barenberg, “Artificial neural networks for analyzing concrete airfield pavements serving the Boeing B-777 aircraft,” *Transp. Res. Rec. J. Transp. Res. Board*, no. 1684, pp. 110–117, 1999.

[10] *2002 Design Guide: Design of New and Rehabilitated Pavement Structures. Draft Final Report for NCHRP Study 1-37A*. Washington, D.C.: NCHRP, Transportation Research Board of the National Academies, 2004.

[11] AASHTO, *Mechanistic-Empirical Pavement Design Guide, Interim Edition: A Manual of Practice*. Washington, D.C: American Association of State Highway and Transportation Officials (AASHTO), 2008.

[12] H. Ceylan and K. Gopalakrishnan, “Neural Networks Based Models for Mechanistic-Empirical Design of Rubblized Concrete Pavements,” *Geotech. Spec. Publ. No. 169, Soil Mater. Inputs Mech. Pavement Des. ASCE*, pp. 1–10, 2007.

[13] O. Elbagalati, M. A. Elseifi, K. Gaspard, and Z. Zhang, “Development of an artificial neural network model to predict subgrade resilient modulus from continuous deflection testing,” *Can. J. Civ. Eng.*, vol. 44, no. 9, pp. 700–706, 2017.

[14] H. Ceylan, S. Kim, K. Gopalakrishnan, C. W. Schwartz, and R. Li, "Sensitivity quantification of jointed plain concrete pavement mechanistic-empirical performance predictions," *Constr. Build. Mater.*, vol. 43, pp. 545–556, 2013.

[15] O. Kaya, A. Rezaei-Tarahomi, H. Ceylan, K. Gopalakrishnan, S. Kim, and D. R. Brill, "Neural Network--Based Multiple-Slab Response Models for Top-Down Cracking Mode in Airfield Pavement Design," *J. Transp. Eng. Part B Pavements*, vol. 144, no. 2, p. 4018009, 2018.

[16] A. Rezaei-Tarahomi, O. Kaya, H. Ceylan, K. Gopalakrishnan, S. Kim, and D. R. Brill, "Neural networks prediction of Critical Responses Related to Top-Down and Bottom-Up Cracking in Airfield Concrete Pavement," in *10th International Conference on the Bearing Capacity of Roads, Railways and Airfields*, 2017.

[17] A. R. Ghanizadeh and M. R. Ahadi, "Application of Artificial Neural Networks for Analysis of Flexible Pavements under Static Loading of Standard Axle," vol. 3, no. 1, 2016.

[18] S. Haykin, "Neural networks: a comprehensive foundation," *Mc Millan, New Jersey*, 1999.

[19] R. Hecht-Nielsen, "Neurocomputers." Addison-Wesley, Massachusetts, 1990.

[20] D. B. Parker and T. Learning Logic, "Report TR-47. MIT," *Cent. Comput. Res. Econ. Manag. Sci. MIT, Cambridge, MA*, 1985.

[21] D. E. Rumelhart, G. E. Hinton, and R. J. Williams, "Learning representations by back-propagating errors," *Nature*, vol. 323, no. 6088, p. 533, 1986.

[22] P. Werbos, "Beyond regression: new fools for prediction and analysis in the behavioral sciences," *PhD thesis, Harvard Univ.*, 1974.

[23] A. Rezaei-Tarahomi, O. Kaya, H. Ceylan, S. Kim, K. Gopalakrishnan, and D. R. Brill, "Development of rapid three-dimensional finite-element based rigid airfield pavement foundation response and moduli prediction models," *Transp. Geotech.*, vol. 13, pp. 81–91, 2017.

CHAPTER 2. SENSITIVITY QUANTIFICATION OF AIRPORT CONCRETE PAVEMENT STRESS RESPONSES ASSOCIATED WITH TOP-DOWN AND BOTTOM-UP CRACKING

Abstract

This study evaluated the sensitivity of NIKE3D-FAA rigid pavement responses with respect to top-down and bottom-up cracking. The analysis was conducted by positioning a Boeing 777-300ER (B777-300ER) aircraft at different locations (critical, corner, and edge of slab) as baseline while varying other NIKE3D-FAA inputs, including rigid pavement geometric features, mechanical properties of paving and foundation materials, equivalent temperature gradient and thermal coefficient of Portland Cement Concrete (PCC) layers. Several sensitivity charts were developed by examining the sensitivity of critical pavement responses to each input variation. Sensitivity evaluations were performed using a normalized sensitivity index (NSI) as the quantitative metric. Using such sensitivity evaluation, the most significant NIKE3D-FAA input parameters for generating an effective synthetic database that will lower computational cost for future modeling developments were identified.

Introduction

Finite Element Analysis - FAA (FEAFAA) program, which makes use of NIKE3D, as a stand-alone tool for 3D FE analysis, predicts design stresses associated with the top-down cracking mode, typically the maximum tensile stress occurring on the top surface of the Portland cement concrete (PCC) slab for a given combination of gear load and initial temperature-induced curling. There are numerous explicit inputs to FEAFAA that must be considered in developing the surrogate stress response prediction model using ANN. To understand which of these inputs are most important and how the critical responses are sensitive to the inputs, it is necessary to perform a sensitivity analysis.

Sensitivity analysis (SA) has become a useful tool in analyzing many engineering problems that involve a large number of interacting variables, including in pavement design and analysis [1]–[6]. For instance, National Cooperative Highway Research Program (NCHRP) 01-47 project [4], [7] was conducted to evaluate local and global sensitivity of pavement performance predicted by the MEPDG [8].

In this study, SA was used to:

- Identify critical control points and prioritize additional data collection or research,
- Focus on those design inputs that have the greatest influence on airport rigid pavement design thickness,
- Identify the most significant input parameters to generate an effective synthetic database that will facilitate lower computational costs for future modeling developments, and
- Identify significant deviations between the model and a real structure.

Preliminary sensitivity studies on the 4-slab 3D FE model employed in FAARFIELD 1.4-TDC have been carried out by Chen, et al., [9], [10] as part of their effort to identify the critical aircraft gear (single-gear and multiple-gear) loading position that would induce the most critical tensile stresses. Their study evaluated the effect of elastic modulus and thickness of each pavement layer and joint stiffness on the critical tensile stresses and the critical top-to-bottom tensile stress ratio (t/b ratio). They used a three-layered pavement structure (PCC surface, granular subbase, and subgrade) for a 25-ft (7.6 m) PCC slab under restricted loading conditions (i.e., A380 aircraft load with an assumed equivalent thermal gradient (ETG) of -1.25 °F/in. (-0.2 °C/cm). These studies [9], [10] reported that the critical

top-to-bottom tensile stress ratio (t/b ratio) was sensitive to the PCC slab thickness and the modulus of the subgrade variation, but not sensitive to variation in subbase thickness, the PCC modulus, or the subbase modulus. Further investigations of interest included consideration of different cases, including a four-layered pavement structure, different loading conditions, and different load locations.

In this study, the sensitivity of the NIKE3D model was evaluated for two aircraft types, B787-8 and B777-300 ER. These aircraft have been selected as representative of wide types of new generation large aircraft with multiple wheel gears. A four-layered pavement structure (PCC surface, cement-treated base, granular subbase, and subgrade) with 9 slabs was modeled to represent a typical airport pavement structure. The 9-slab 3D-FE model is better for simulating the real continuous jointed slabs conditions than the 4-slab 3D-FE model and also more suitable for accommodation of multiple gear aircraft. Three load locations were selected: critical location, slab edge, and slab corner (Figure 2.1). Two load cases were considered for each load location: (1) mechanical loading only and (2) simultaneous mechanical and thermal loading. A one-at-a-time (OAT) SA was implemented using a baseline limit normalized sensitivity index (NSI) to provide quantitative sensitivity information. The procedure and the results of the sensitivity analysis are discussed in the next sections. The discussion in this study highlights the significant analysis input properties required for generating an effective synthetic database for facilitating the computational efficiency of future modeling developments.

Pavement Model

The remainder of this section presents the results for the B777-300 ER aircraft. The B777 was chosen for the SA because this aircraft is representative of new generation heavy

and complex gear aircraft that can cause high stresses on tops and bottoms of concrete slabs in rigid airfield pavements.

In the FEAFAA 3D mesh, structural layers and the topmost layers of the subgrade use standard eight-node solid hexahedral elements. The bottommost layer of elements in the subgrade consists of 8-noded "infinite" elements to represent the assumed infinite subgrade. The number of mesh elements for the concrete slab and foundation layers (base, subbase, and subgrade) was 30 at each side, i.e., each slab had 900 elements and 1,922 nodes. Since the total number of elements for the pavement structure was 12,600 and the total number of nodes was 23,064, if a slab with dimensions of 25×25 ft. (7.6×7.6 m) is used, mesh size will be 10×10 in (25.4×25.4 cm).

The Boeing B777-300ER aircraft gear has three dual (3D) gears in tandem. The total weight on the gear is 1,641.73 kN approximated in the model in a uniform contact pressure 1,523.7 kPa distributed over six rectangular areas of 0.18 m^2 each. These areas were positioned at a tandem spacing of 146.3 cm and a dual spacing of 139.7 cm.

Figure 2.1 is a sketch of the 9-slab 3D-FE pavement model showing the positions of the B777-300 ER 6-wheel gear. Three load locations were considered for sensitivity analysis in this study: corner, edge, and critical (see Figure 2.1). Critical loading is the case in which one line of wheels is on the edge of the slab and the other is on the adjacent slab. This load location was identified as the most critical by Chen, et.al, [9] in an analysis of critical stress of large aircraft on airport rigid pavement using FEAFAA.

The sensitivity of input parameters was evaluated by considering their effects on the critical responses corresponding to top-down and bottom-up cracking. Figure 2.2 shows the overall SA process employed in this study.

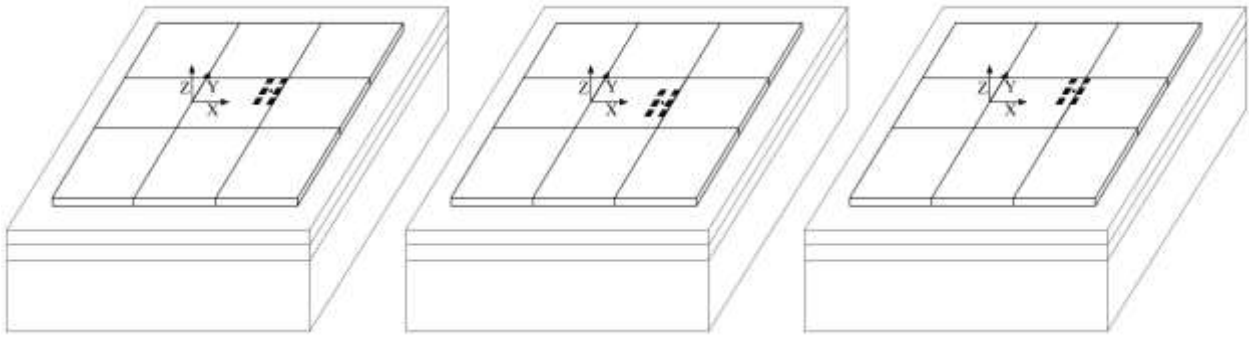

Figure 2.1 *Sketch of 3D-FE model of a 9-slab rigid pavement showing the position of the B777-300 ER gear load. Coordinates are with respect to the origin indicated by the 3D triad.*

The OAT SA was carried out using FEAFAA 2.0 software by varying one parameter at a time while holding the others fixed. This analysis was useful for identifying the most significant inputs. However, the sensitivity of all the inputs could not be evaluated using the OAT method because some are interrelated, while others (e.g., mesh fineness, expressed as the number of elements) are used for FE modeling only. Some inputs (e.g., Poisson ratio, equivalent boundary stiffness) are assumed, based on engineering judgment and pre-parametric sensitivity analysis, to have only minor influence. Constant values were assigned to those inputs.

The goal was to evaluate the sensitivity of the most critical responses to those input parameters judged to be most important for analyzing and designing airfield concrete pavements. A detailed summary of ranges of the inputs to be varied as well as the assumed-constant inputs are shown in Table 2.1. Each evaluated input was varied within its recommended range to determine its effect on critical responses (maximum tensile stress and shear stress at top/bottom of the slab) while assigning base-case values to all other input parameters.

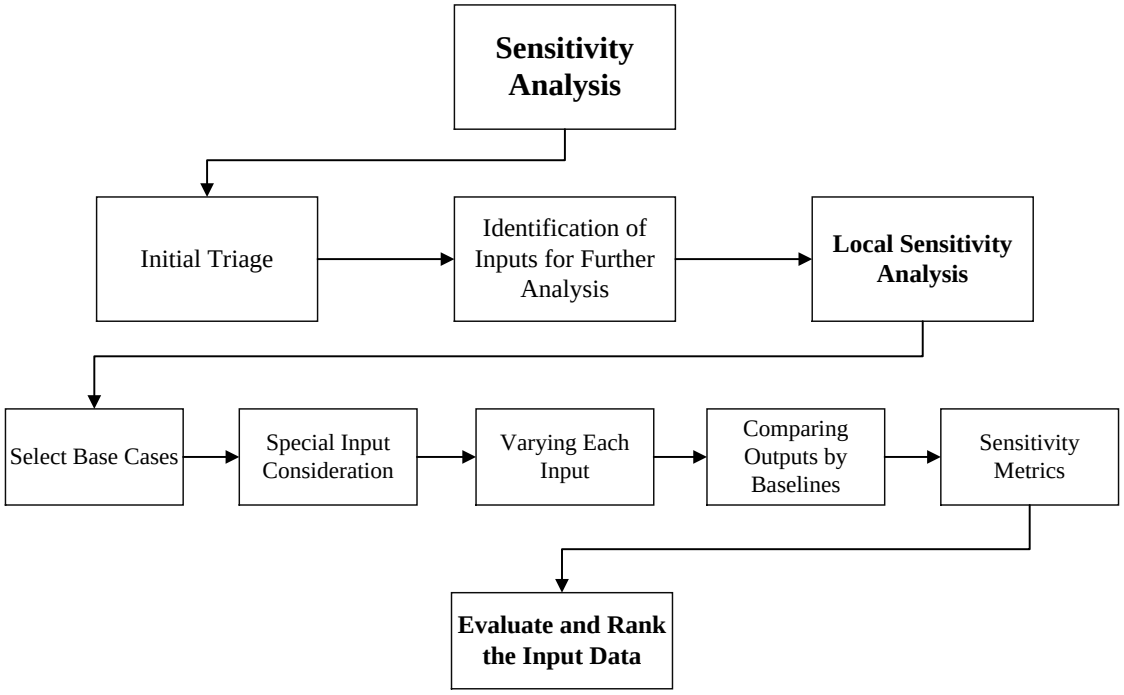

Figure 2.2 *Simplified flow chart for local sensitivity analysis of FEAFAA.*

In FEAFAA, joints are modeled as continuous linear elastic shear springs connecting the slabs. The springs, acting only in the vertical direction, represent the action of dowel bars. Dowel bar data are accepted by the program, but converted to equivalent linear springs for actual analysis. To evaluate the sensitivity of stress responses to joint properties, equivalent joint stiffness was used. The equivalent joint stiffness ranges are shown in Table 2.1.

To determine the number of elements for mesh modeling, a pre-parametric sensitivity analysis was carried out. Figure 2.3 shows the changes in stress responses with respect to a varying number of elements for both slabs (Figure 2.3 (a)) and foundation layers (Figure 2.3 (b)). As the number of elements increases, the stresses converge to a specific value. From this figure, it is obvious that for fewer than 30 elements the results are not constant, while for more than 30 elements the results stay the same. However, since increasing the number of elements can dramatically increase the run time of NIKE3D (i.e., from about 16 min. for 30

elements to about 50 min. for 50 elements), an optimum number of 30 elements could be selected for meshing both the slab and foundation without sacrificing result accuracy while at the same time not being too computationally intensive. Furthermore, if 30 elements were used, there was no need to refine the mesh near the loading positions because the slab mesh size (25.4×25.4 cm) are smaller than the tire foot-print (60.5×37.6 cm), so the FE model could promise accurate results.

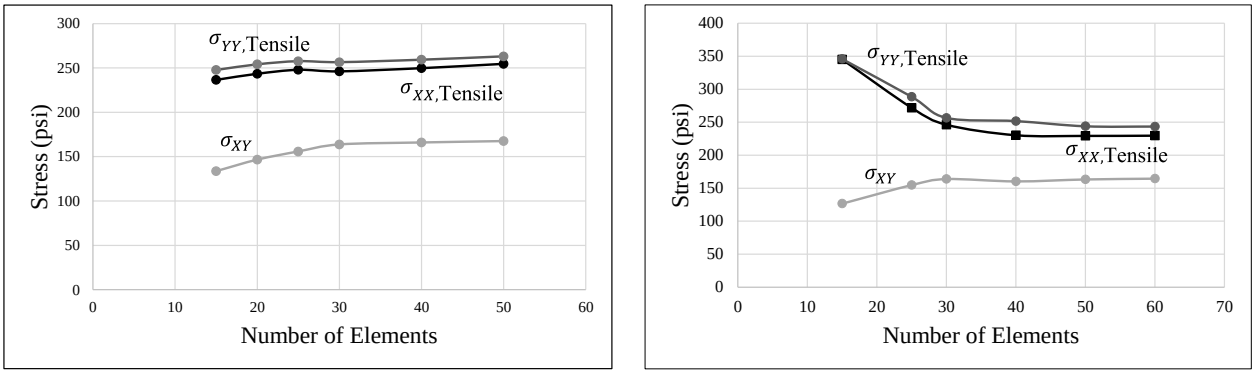

Figure 2.3 *Sensitivity of top tensile and shear stresses to the (a) slabs (b) foundation layers number of elements for NIKE3D-FAA solutions under B777-300 ER loading.*

To represent the sensitivity of each parameter, a normalized sensitivity index (NSI) has been adopted as a quantitative metric.

$$\boldsymbol{NSI} = \frac{\Delta \boldsymbol{Y_j}}{\Delta \boldsymbol{X_k}} \frac{\boldsymbol{X_k}}{\boldsymbol{Y_K}} \tag{3}$$

Where:

$\boldsymbol{X_k}$ = Baseline value of input k

$\Delta \boldsymbol{X_k}$ = Change in input k about the base line

$\Delta \boldsymbol{Y_j}$ = Change in output j corresponding to $\Delta \boldsymbol{X_k}$

$\boldsymbol{Y_K}$ = Baseline value of output j.

Table 2.1 *Ranges of inputs for sensitivity analysis of FEAFAA.*

Inputs Category	Inputs		Range			Base case
			Min	Baseline	Max	
Pavement structure inputs	PCC Slab	Modulus, psi (GPa)	3×10^6 (20.7)	5×10^6 (34.5)	7×10^6 (48.3)	4×10^6 (27.6)
		Thickness, in. (cm)	10 (25.4)	17 (43.2)	24 (61)	14 (35.6)
		Poisson Ratio	0.15			
	Cement Treated Base	Modulus, psi (GPa)	2.5×10^5 (1.7)	1.125×10^6 (7.8)	2×10^6 (13.8)	5×10^5 (3.5)
		Thickness, in. (cm)	6 (15.2)	18 (45.7)	30 (76.2)	8 (20.3)
		Poisson Ratio	0.15			
	Granular Subbase	Modulus, psi (GPa)	15,000 (1×10^{-1})	45,000 (3.1×10^{-1})	75,000 (5.2×10^{-1})	75,000 (5.2×10^{-1})
		Thickness, in. (cm)	6 (15.2)	18 (45.7)	30 (76.2)	12 (30.5)
		Poisson Ratio	0.35			
	Subgrade	Modulus, psi (GPa)	3,000 (2.1×10^{-2})	16,500 (1.1×10^{-1})	30,000 (2.1×10^{-1})	3,000 (2.1×10^{-2})
		Poisson Ratio	0.4			
	Slab Dimension, ft. (m)		25 (7.6)			
	Slab Number of Elements		30			
	Number of Slabs		9			
	Foundation Number of Elements		30			
Aircraft inputs	Aircraft parameters		B777-300ER: Gross weight=777,000 (lb), %GW= 95%, No. Main Gears=2, Wheels on Main Gears=6, Tire Pressure (psi)=221			
Loading inputs	Loading Angle Θ_g		0			
	Loading Position		Critical/Mid Slab Edge/Corner			
	Equivalent Temperature Gradient, ^{o}F/in. (^{o}C/cm)		2 (0.26)	2.5 (0.37)	3 (0.48)	2.3 (0.33)
	Thermal Coefficient, 1/^{o}F (1/^{o}C)		4.1×10^{-6} (7.6×10^{-6})	5.5×10^{-6} (9.9×10^{-6})	7×10^{-6} (12.2×10^{-6})	5×10^{-6} (9×10^{-6})
Joint modeling inputs	Equivalent Joint Stiffness, psi/in (GPa/m)		1,000 (2.7×10^{-1})	100,000 (27.1)	300,000 (81.3)	144,798 (39.2)

Based on the results obtained in this study and sensitivity rankings based on NSI in authors' previous studies [3], [4], sensitivity ranking can be categorized as very sensitive ($0.5 \leq NSI < 3$), sensitive ($0.1 \leq NSI < 0.5$), and low sensitive ($NSI < 0.1$).

As mentioned earlier, three load locations were considered for sensitivity analysis: critical, edge, and corner. For each location, analysis was carried out for two load types: mechanical loading only and simultaneous mechanical and thermal loading. Six stresses considered as critical were used as outputs for the NSI calculation:

- Maximum tensile stress at the top of the slab (Top tensile stress)
- Maximum tensile stress at the bottom of the slab (Bottom tensile stress)
- Maximum shear stress at top of the slab (Top shear stress)
- Maximum shear stress at bottom of the slab (Bottom shear stress)
- Maximum principal tensile stress at the top of the slab (Top principal stress)
- Maximum principal tensile stress at bottom of the slab (Bottom principal stress)

Critical Loading Position

Figures 2.4 and 2.5 show sensitivity of critical stresses with respect to different inputs when the aircraft is located at the critical loading position.

Mechanical Loading Only

Figure 2.4 (a) shows that PCC thickness has the most influence on the responses at the top and bottom of the slab (i.e., top tensile stress, bottom tensile stress, and bottom shear stress). The subgrade modulus has the next highest influence on the top tensile stress. Sensitivity indices of base thickness and PCC modulus show that all stress responses are sensitive to changes in these input variables. The inputs to which the responses are either insensitive or 'very low sensitive' are base modulus, equivalent joint stiffness, and subbase

modulus. Most effective inputs except slab thickness and subgrade modulus, had higher NSI values for the top tensile stress than for the bottom tensile stress, and NSI of all inputs for top shear stress were close to those for bottom shear stress.

Figure 2.5 displays the sensitivity of principal stresses with respect to different input variations. Figure 2.5 (a) shows that, under mechanical loading only, the critical principal stress at the bottom of the PCC slab is most sensitive to the PCC slab thickness (NSI=1.36), while the principal stress at the top of the PCC slab is more sensitive to base layer thickness (NSI=0.92) than PCC slab thickness (NSI=0.88). Figure 2.5 (a) also illustrates that, next to PCC slab thickness, the critical principal stress at the bottom of the PCC slab is most sensitive to the subgrade modulus (NSI=0.67).

Simultaneous Mechanical and Thermal Loading

Figure 2.4 (b) depicts sensitivity analysis results for the case in which both critical mechanical loading and temperature loading were applied to the modeled pavement structure. FEAFAA considers both temperature curling and concrete shrinkage effects by introducing the concept of equivalent temperature gradient (ETG) [11]. Because of temperature gradient and shrinkage effects, the initial concrete slab shape affects responses of the PCC slab to aircraft gear loading. The use of a simple compensation term applied to ETG can change the initial slab shape from circular to catenary, thereby significantly improving the computational results [11]. All analyses related to the temperature-loading cases were conducted using a catenary shape to represent slab curling. As shown in Figure 2.4 (b), the bottom tensile stresses are more sensitive to slab thickness (NSI=2.04) than the other inputs, showing the importance of this input for studying bottom-up cracking in concrete pavement. Figure 2.4 (b) shows that the bottom tensile stress is also sensitive to subgrade modulus (NSI=1.29) and

thermal coefficient (NSI=0.59), followed by base layer thickness, ETG, PCC modulus, and subbase thickness.

Variations in thermal coefficients and ETG have high impact with respect to tensile stresses at the top of the slab. High sensitivity to temperature-loading-related inputs for top tensile stresses indicate the importance of curling analysis for top-down cracking model development.

Figure 2.4 (b) indicates that shear stress is most sensitive to base thickness and PCC slab modulus (NSI=0.58) followed by slab thickness, subgrade modulus, thermal coefficient, subbase thickness, and ETG. Figure 2.4 (b) also shows that changes in base and subbase modulus and equivalent joint stiffness have the lowest effects on all stress responses.

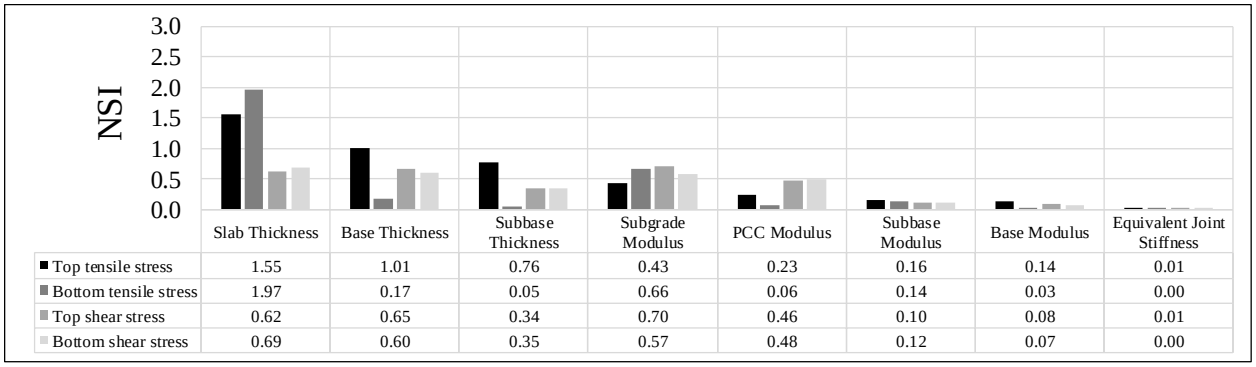

	Slab Thickness	Base Thickness	Subbase Thickness	Subgrade Modulus	PCC Modulus	Subbase Modulus	Base Modulus	Equivalent Joint Stiffness
Top tensile stress	1.55	1.01	0.76	0.43	0.23	0.16	0.14	0.01
Bottom tensile stress	1.97	0.17	0.05	0.66	0.06	0.14	0.03	0.00
Top shear stress	0.62	0.65	0.34	0.70	0.46	0.10	0.08	0.01
Bottom shear stress	0.69	0.60	0.35	0.57	0.48	0.12	0.07	0.00

(a)

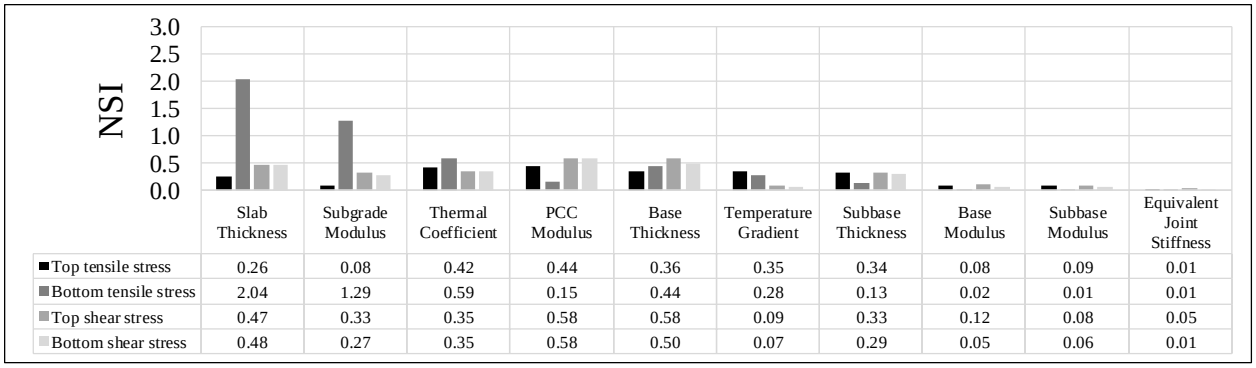

	Slab Thickness	Subgrade Modulus	Thermal Coefficient	PCC Modulus	Base Thickness	Temperature Gradient	Subbase Thickness	Base Modulus	Subbase Modulus	Equivalent Joint Stiffness
Top tensile stress	0.26	0.08	0.42	0.44	0.36	0.35	0.34	0.08	0.09	0.01
Bottom tensile stress	2.04	1.29	0.59	0.15	0.44	0.28	0.13	0.02	0.01	0.01
Top shear stress	0.47	0.33	0.35	0.58	0.58	0.09	0.33	0.12	0.08	0.05
Bottom shear stress	0.48	0.27	0.35	0.58	0.50	0.07	0.29	0.05	0.06	0.01

(b)

Figure 2.4 *NSI of different input values vs. critical responses for (a) critical-mechanical loading and (b) critical-mechanical loading with temperature loading.*

Figure 2.5 (b) shows that, under simultaneous mechanical and temperature loading, the critical principal stress at the bottom of the PCC slab is most sensitive to PCC slab thickness (NSI=1.5), subgrade modulus and base layer thickness. The principal stress at the top of the PCC slab is most sensitive to PCC slab modulus (NSI=0.54), thermal coefficient, base-layer thickness, and temperature gradient. Unlike for mechanical loading only, under simultaneous mechanical and temperature loading, top tensile stress has very low sensitivity to slab thickness (NSI=0.03) and subgrade modulus (NSI=0.17).

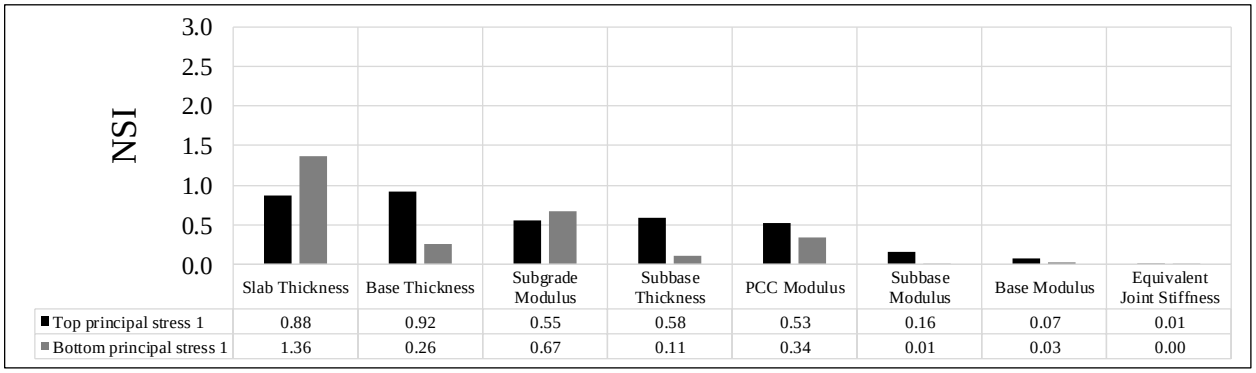

(a)

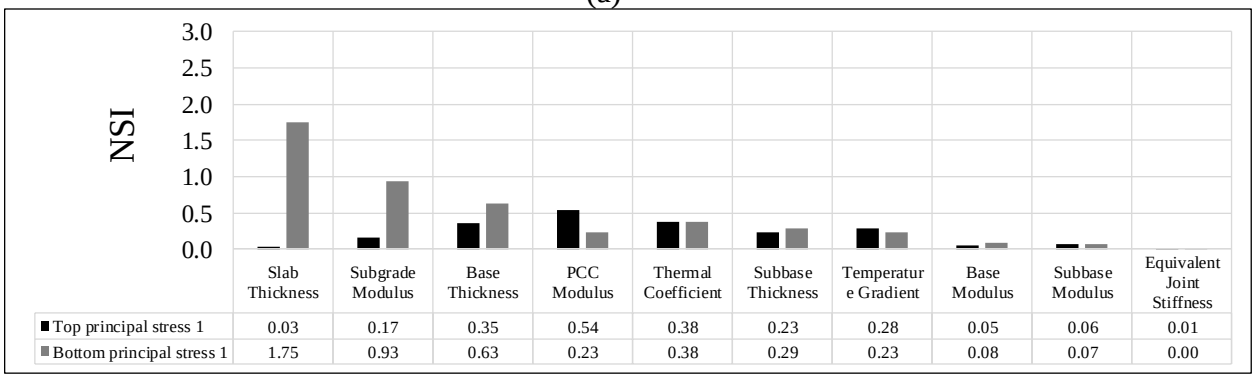

(b)

Figure 2.5 *NSI of different input values vs. critical principal stresses for (a) edge mechanical loading and (b) edge mechanical loading with temperature loading.*

Edge Loading

For rigid pavement design, the FAA uses the maximum tensile stress at the bottom edge of the PCC slab as a predictor of pavement structural life. The maximum tensile stress for design is determined using an edge loading condition. Figure 2.6 shows sensitivities

computed for edge loading only as well as edge loading in combination with temperature loading.

Mechanical Loading Only

Figure 2.6 (a) displays the sensitivity analysis results for different inputs when the load is centered on one edge of the middle slab. Again, PCC slab thickness is the most effective input for top and bottom tensile stresses. Top tensile stresses, unlike bottom tensile stresses, exhibit significant sensitivity to the base and subbase thickness. Variations in modulus of PCC, base, and subbase have less effect on bottom tensile stresses, but subgrade modulus has a large effect on all stress responses. The big difference between NSI of top and bottom tensile stresses is because of normalized ratio of variations. For instance, by increasing the base layer thickness from 6 to 30 in, top tensile stress decreases from 241 to 70 psi (171 psi variation) (NSI=1.0) while bottom tensile stress decreases from 602 to 448 psi (154 psi variation) (NSI=0.19). Although the variation are very close for both case, the ratio is different.

Top tensile stresses exhibit considerable sensitivity to most inputs, while bottom tensile stresses have considerable sensitivity to just two inputs (PCC thickness and subgrade modulus). It can be noted in Figure 2.6 that the inputs associated with the greatest effect on shear stresses are thickness of PCC, base and subbase; subgrade modulus; and PCC modulus. Similar to previous cases, the stress responses are not sensitive to subbase/base modulus and equivalent joint stiffness (lowest NSI).

Figure 2.7 (a) shows that, under mechanical-only loading the critical principal stress at the top of the PCC slab is most sensitive to PCC slab thickness (NSI=1.38) and the base and subbase layers thickness. The principal stress at the bottom of the PCC slab is most sensitive to the slab thickness (NSI=1.22), subgrade modulus, and PCC modulus.

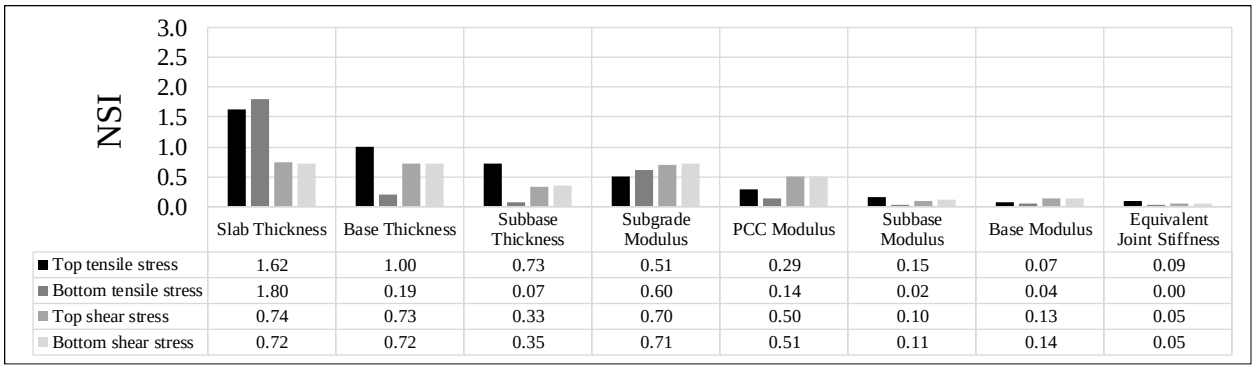

	Slab Thickness	Base Thickness	Subbase Thickness	Subgrade Modulus	PCC Modulus	Subbase Modulus	Base Modulus	Equivalent Joint Stiffness
Top tensile stress	1.62	1.00	0.73	0.51	0.29	0.15	0.07	0.09
Bottom tensile stress	1.80	0.19	0.07	0.60	0.14	0.02	0.04	0.00
Top shear stress	0.74	0.73	0.33	0.70	0.50	0.10	0.13	0.05
Bottom shear stress	0.72	0.72	0.35	0.71	0.51	0.11	0.14	0.05

(a)

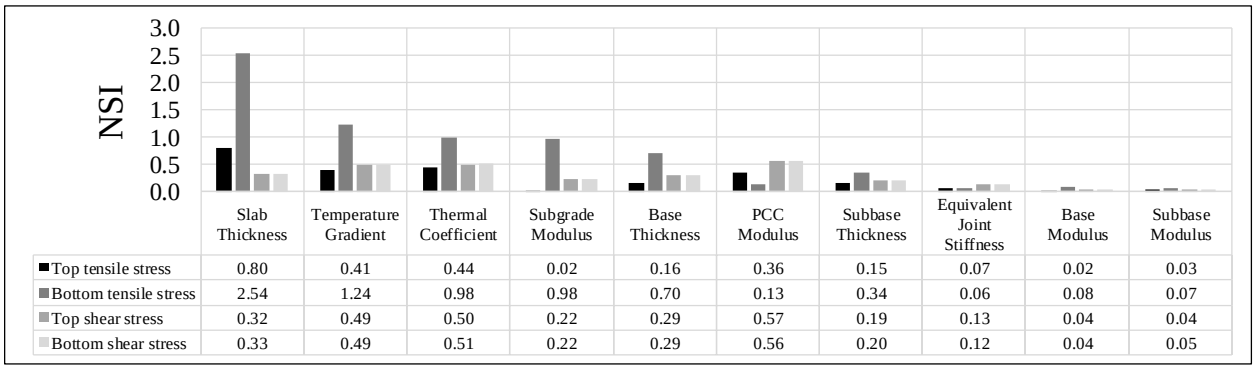

	Slab Thickness	Temperature Gradient	Thermal Coefficient	Subgrade Modulus	Base Thickness	PCC Modulus	Subbase Thickness	Equivalent Joint Stiffness	Base Modulus	Subbase Modulus
Top tensile stress	0.80	0.41	0.44	0.02	0.16	0.36	0.15	0.07	0.02	0.03
Bottom tensile stress	2.54	1.24	0.98	0.98	0.70	0.13	0.34	0.06	0.08	0.07
Top shear stress	0.32	0.49	0.50	0.22	0.29	0.57	0.19	0.13	0.04	0.04
Bottom shear stress	0.33	0.49	0.51	0.22	0.29	0.56	0.20	0.12	0.04	0.05

(b)

Figure 2.6 *NSI of different input values vs. critical responses for (a) edge mechanical loading and (b) edge mechanical loading with temperature loading.*

Simultaneous Mechanical and Thermal Loading

Analysis results for this case are presented in Figure 2.6 (b), where it can be seen that top and bottom tensile stresses exhibit higher sensitivity to PCC slab thickness than other inputs. Temperature-loading-related inputs (ETG and thermal coefficient) also exhibit sensitivity for both tensile stresses. Most notably, higher NSI values for these inputs were observed for bottom tensile stresses than for top tensile stresses.

Similarly, bottom tensile stresses show higher sensitivity than top tensile stresses to subgrade modulus, base thickness, and subbase thickness. It can also be noted that top tensile stress is not sensitive to the subgrade modulus input, while top tensile stresses have higher sensitivity than bottom tensile stresses to the PCC modulus.

The ETG, thermal coefficient, PCC slab thickness and modulus, subgrade modulus, base thickness, and subbase thickness are all effective inputs for both top and bottom shear stresses.

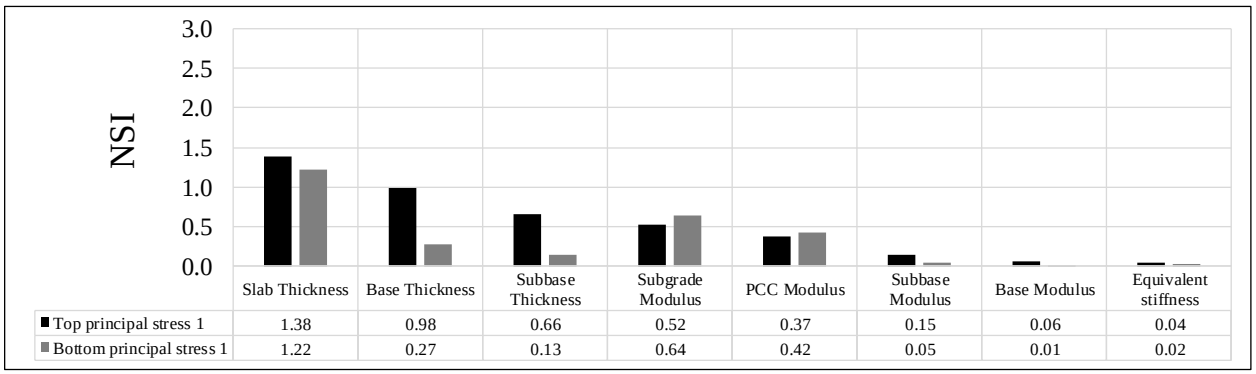

	Slab Thickness	Base Thickness	Subbase Thickness	Subgrade Modulus	PCC Modulus	Subbase Modulus	Base Modulus	Equivalent stiffness
Top principal stress 1	1.38	0.98	0.66	0.52	0.37	0.15	0.06	0.04
Bottom principal stress 1	1.22	0.27	0.13	0.64	0.42	0.05	0.01	0.02

(a)

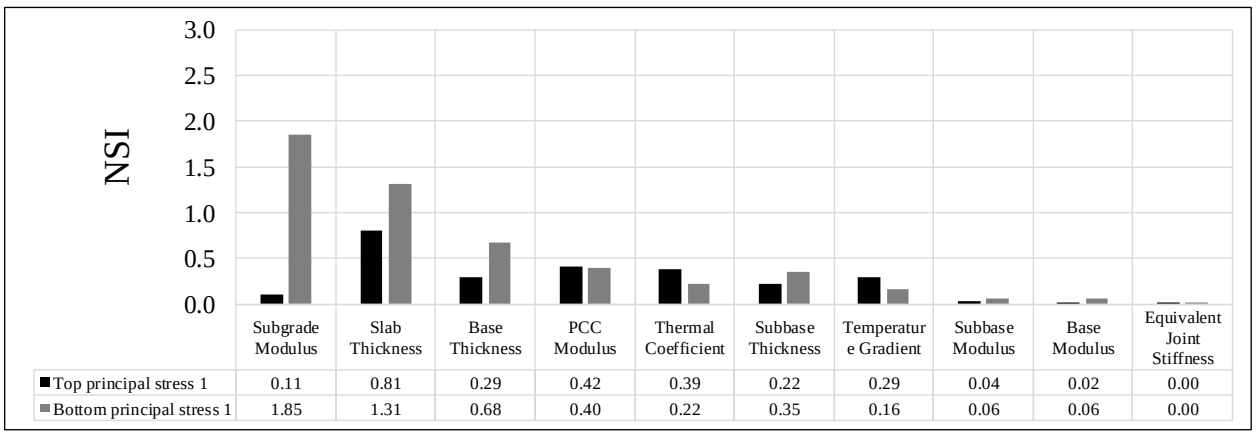

	Subgrade Modulus	Slab Thickness	Base Thickness	PCC Modulus	Thermal Coefficient	Subbase Thickness	Temperature Gradient	Subbase Modulus	Base Modulus	Equivalent Joint Stiffness
Top principal stress 1	0.11	0.81	0.29	0.42	0.39	0.22	0.29	0.04	0.02	0.00
Bottom principal stress 1	1.85	1.31	0.68	0.40	0.22	0.35	0.16	0.06	0.06	0.00

(b)

Figure 2.7 *NSI of different input values vs. critical principal stresses for (a) edge mechanical loading and (b) edge mechanical loading with temperature loading.*

Figure 2.7 (b) shows the sensitivity of critical principal stress at the bottom of the PCC slab to the properties of the pavement under simultaneous mechanical and temperature loading. As shown in Figure 2.7 (b), bottom principal stress is most sensitive to the subgrade modulus (NSI=1.85). Figure 2.7 (b) also illustrates that, next to subgrade modulus, critical bottom principal stress has significant sensitivity to both slab thickness (NSI=1.31) and base-layer thickness (NSI=0.68). The principal stress at the top of the PCC slab is most sensitive

to PCC slab thickness (NSI=0.81). After PCC slab thickness, top principal stress is more sensitive to the PCC slab modulus (NSI=0.42), thermal coefficient (NSI=0.39), temperature gradient (NSI=0.29), base-layer thickness (NSI=0.29), subbase thickness (NSI=0.22), and subgrade modulus (NSI=0.11).

Corner Loading

In this case, sensitivity analysis was conducted for the B777-300 ER gear located at the corner of the slab. Corner loading is important for analysis and design purposes because of major observed failures that have occurred at this location and because of load transfer issues arising from joints.

Mechanical Loading Only Case

Figure 2.8 (a) illustrates how critical stress responses are sensitive to the various inputs. Again, PCC slab thickness exhibited the highest NSI for top and bottom tensile stresses (NSI=1.28 and 1.51, respectively). Base and subbase thickness exhibited high NSI values for top tensile stresses (NSI=1.03 and 0.76) but low NSI values for bottom tensile stresses (NSI=0.19 and 0.05), while subgrade modulus and PCC modulus are effective inputs for both types of tensile stresses. Figure 2.8 (a) also shows that shear stresses are somewhat sensitive to subgrade modulus, PCC modulus, PCC slab thickness, base thickness, and subbase thickness, and less sensitive to base modulus, subbase modulus, and equivalent joint stiffness.

Figure 2.9 (a) shows that, under mechanical-only loading, the critical top principal stress is most sensitive to base layer thickness (NSI=0.90) and also to the slab thickness (NSI=0.86). Furthermore, the principal stress at the bottom of the PCC slab is most sensitive to slab thickness (NSI=1.62) and the subgrade modulus (NSI=0.60).

Simultaneous Mechanical and Thermal Loading Case

Figure 2.8 (b) shows that, among all inputs, PCC slab thickness has the highest NSI for top and bottom tensile stresses. Much higher NSI values of PCC slab thickness were observed for bottom tensile stresses (NSI=2.12) than for top tensile stresses (NSI=0.59). Thermal coefficient is the second effective input for bottom tensile stresses, while other inputs to which bottom tensile stresses are sensitive are base thickness, subbase thickness, and subgrade modulus. Top tensile stresses have low sensitivity to PCC modulus and ETG.

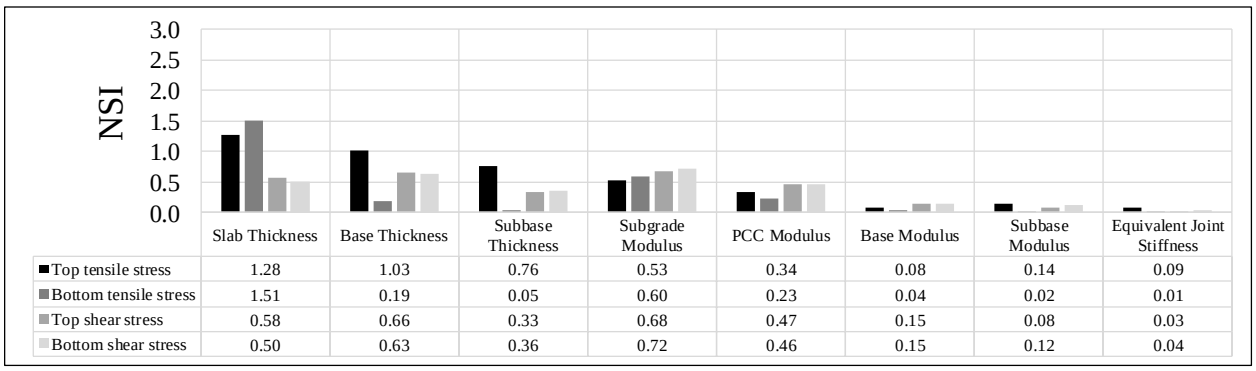

	Slab Thickness	Base Thickness	Subbase Thickness	Subgrade Modulus	PCC Modulus	Base Modulus	Subbase Modulus	Equivalent Joint Stiffness
Top tensile stress	1.28	1.03	0.76	0.53	0.34	0.08	0.14	0.09
Bottom tensile stress	1.51	0.19	0.05	0.60	0.23	0.04	0.02	0.01
Top shear stress	0.58	0.66	0.33	0.68	0.47	0.15	0.08	0.03
Bottom shear stress	0.50	0.63	0.36	0.72	0.46	0.15	0.12	0.04

(a)

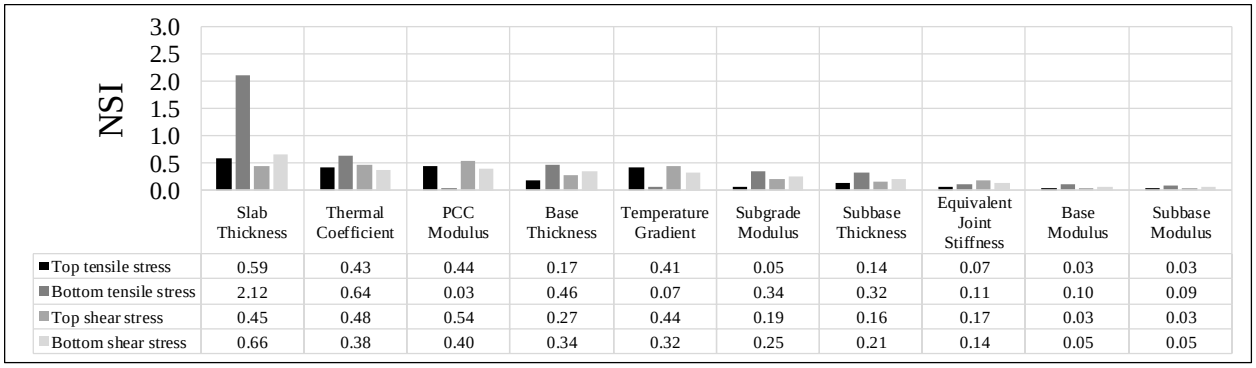

	Slab Thickness	Thermal Coefficient	PCC Modulus	Base Thickness	Temperature Gradient	Subgrade Modulus	Subbase Thickness	Equivalent Joint Stiffness	Base Modulus	Subbase Modulus
Top tensile stress	0.59	0.43	0.44	0.17	0.41	0.05	0.14	0.07	0.03	0.03
Bottom tensile stress	2.12	0.64	0.03	0.46	0.07	0.34	0.32	0.11	0.10	0.09
Top shear stress	0.45	0.48	0.54	0.27	0.44	0.19	0.16	0.17	0.03	0.03
Bottom shear stress	0.66	0.38	0.40	0.34	0.32	0.25	0.21	0.14	0.05	0.05

(b)

Figure 2.8 *NSI of different input values vs. critical responses for (a) corner-mechanical loading and (b) corner-mechanical loading with temperature loading.*

Figure 2.9 (b) shows the sensitivity of critical principal stresses to pavement properties under simultaneous mechanical and temperature loading. The bottom principal stress is most sensitive to the slab thickness (NSI=2.27). Next to slab thickness, critical

bottom principal stress has significant sensitivity to subgrade modulus. The principal stress at the top of the PCC slab is most sensitive to PCC slab thickness (NSI=0.58) and PCC slab modulus (NSI=0.53).

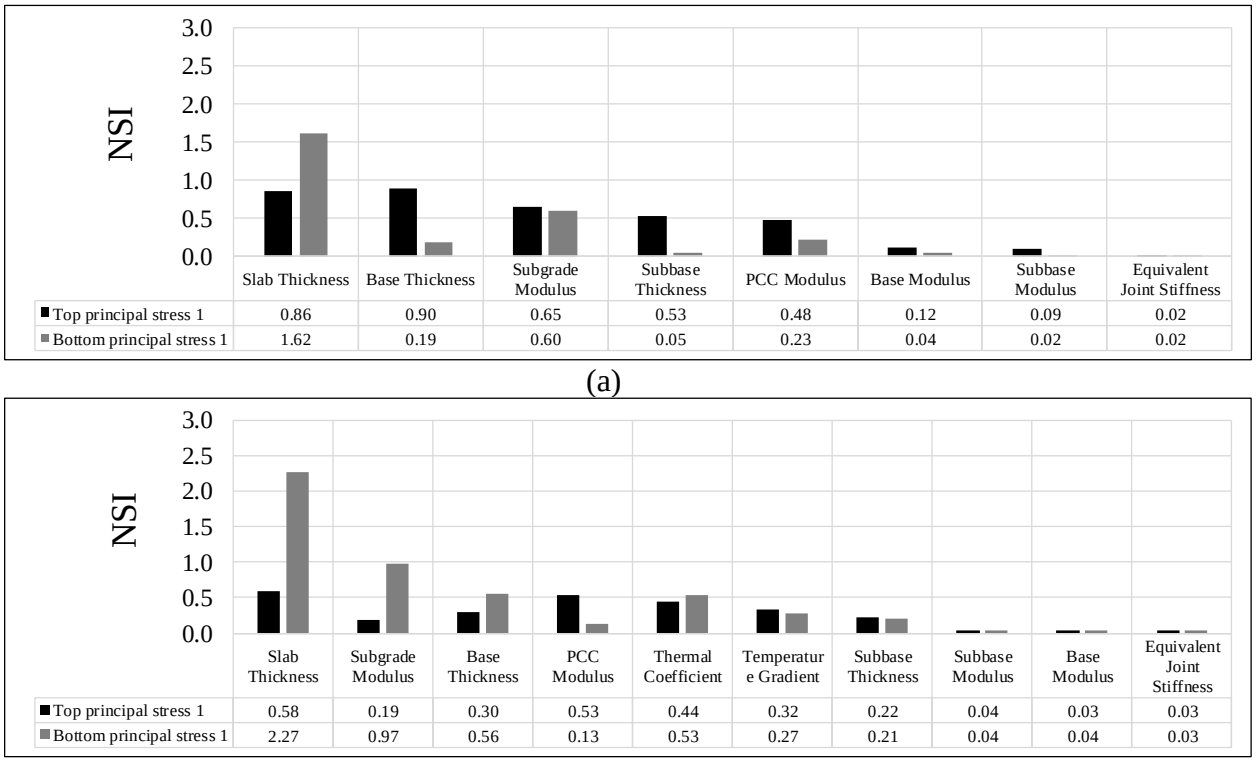

Figure 2.9 *NSI of different input values vs. critical principal stresses for (a) corner-mechanical loading and (b) corner-mechanical loading with temperature loading.*

Discussion of Sensitivity Results

Tables 2.2 to 2.5 summarize maximum NSI values of each input for all loading conditions, with inputs ranked separately for each stress response. Shear stress entries combine top and bottom shear stress since both have similar sensitivity levels with respect to all inputs. Tables 2.2 and 2.3 rank the sensitivity to various inputs of stress responses under mechanical loading only. Input rankings were obtained quite similarly in Tables 2.2 and 2.3. The three most effective inputs for top and bottom axial stresses are the same as three most effective inputs for the top and bottom principal stresses, respectively. Subgrade modulus has

greater effect on bottom tensile stress and shear stress than top tensile stress. Inputs categorized as insensitive for all stress responses are equivalent joint stiffness, base modulus, and subbase modulus.

Table 2.2 *Sensitivity ranking for stress responses to mechanical loading.*

Inputs	**NSI**	**Inputs**	**NSI**	**Inputs**	**NSI**
	Top tensile stress		**Bottom tensile stress**		**Shear stress**
PCC Thickness	1.62	PCC Thickness	1.97	PCC Thickness	0.74
Base Thickness	1.03	Subgrade Modulus	0.66	Base Thickness	0.73
Subbase Thickness	0.76	PCC Modulus	0.23	Subgrade Modulus	0.70
Subgrade Modulus	0.53	Base Thickness	0.19	PCC Modulus	0.50
PCC Modulus	0.34	Subbase Modulus	0.14	Subbase Thickness	0.34
Subbase Modulus	0.16	Subbase Thickness	0.07	Base Modulus	0.15
Base Modulus	0.14	Base Modulus	0.04	Subbase Modulus	0.10
Equivalent Stiffness	0.09	Equivalent Stiffness	0.01	Equivalent Stiffness	0.05

Table 2.3 *Sensitivity ranking for principal stress responses to mechanical loading.*

Inputs	**NSI**	**Inputs**	**NSI**
	Top principal stress (1)		**Bottom principal stress (1)**
PCC Thickness	1.38	PCC Thickness	1.62
Base Thickness	0.98	Subgrade Modulus	0.67
Subbase Thickness	0.66	PCC Modulus	0.42
Subgrade Modulus	0.65	Base Thickness	0.27
PCC Modulus	0.53	Subbase Thickness	0.13
Subbase Modulus	0.16	Subbase Modulus	0.05
Base Modulus	0.12	Base Modulus	0.04
Equivalent Stiffness	0.04	Equivalent Stiffness	0.02

Tables 2.4 and 2.5 show input sensitivity rankings for stress responses under simultaneous mechanical and temperature loading. Based on the NSI values shown in these tables, the top five most influential properties of the rigid pavement with respect to top tensile and top principal stress are PCC thickness, PCC modulus, thermal coefficient, temperature gradient, and base thickness, while the top five most influential properties for bottom tensile stress are PCC thickness, subgrade modulus, thermal coefficient, base

thickness, and temperature gradient. For bottom principal stress, while temperature gradient is not among the top five properties, PCC modulus is included. For shear stresses, the most influential parameters are base thickness, PCC modulus, PCC thickness, thermal coefficient, and subgrade modulus.

Table 2.4 *Sensitivity ranking for stress responses to combined mechanical and temperature loading.*

Inputs	NSI Top tensile stress	Inputs	NSI Bottom tensile stress	Inputs	NSI Shear stress
PCC Thickness	0.96	PCC Thickness	2.73	Base Thickness	0.58
PCC Modulus	0.44	Subgrade Modulus	1.62	PCC Modulus	0.58
Thermal Coefficient	0.42	Thermal Coefficient	0.62	PCC Thickness	0.55
Temperature gradient	0.38	Base Thickness	0.55	Thermal Coefficient	0.39
Base Thickness	0.36	Temperature gradient	0.28	Subgrade Modulus	0.33
Subbase Thickness	0.34	Subbase Thickness	0.20	Subbase Thickness	0.33
Subgrade Modulus	0.15	PCC Modulus	0.15	Base Modulus	0.12
Subbase Modulus	0.09	Subbase Modulus	0.03	Temperature gradient	0.09
Base Modulus	0.08	Base Modulus	0.03	Subbase Modulus	0.08
Equivalent Stiffness	0.03	Equivalent Stiffness	0.02	Equivalent Stiffness	0.07

Table 2.5 *Sensitivity ranking for principal stress responses to combined mechanical and temperature loading.*

Inputs	NSI Top principal stress (1)	Inputs	NSI Bottom principal stress (1)
PCC Thickness	0.81	PCC Thickness	2.27
PCC Modulus	0.54	Subgrade Modulus	1.85
Thermal Coefficient	0.44	Base Thickness	0.68
Base Thickness	0.35	Thermal Coefficient	0.53
Temperature gradient	0.32	PCC Modulus	0.40
Subbase Thickness	0.23	Subbase Thickness	0.35
Subgrade Modulus	0.19	Temperature gradient	0.27
Subbase Modulus	0.06	Base Modulus	0.08
Base Modulus	0.05	Subbase Modulus	0.07
Equivalent Stiffness	0.03	Equivalent Stiffness	0.03

Summary and Conclusions

The primary objective of the sensitivity study was to quantify sensitivity of stress responses to various inputs required in NIKE3D with respect to critical stress outputs at different loading locations and different load case scenarios for a B777-300ER aircraft. A four-layered pavement structure (PCC surface, cement treated base, granular subbase, and subgrade) used in 9 slabs was modeled to represent typical and realistic airport pavement structure. The OAT SA was implemented using a baseline limit normalized sensitivity index (NSI) to provide quantitative sensitivity information on each stress response output for different loading conditions. Through the SA, critical input parameters that have an influence on FEAFAA outputs were identified. Results show:

- The maximum stress response solutions by NIKE3D-FAA are the most sensitive to the Portland cement concrete (PCC) slab thickness, followed by base and subbase thicknesses for top tensile stress, and subgrade modulus for bottom tensile stresses and shear stresses.
- Top tensile stress is more sensitive to thermal coefficient variation than equivalent temperature gradient (ETG) variation, while bottom tensile stress shows higher sensitivity to ETG variation than thermal coefficient. In other words, thermal coefficient may make greater contribution to top-down cracking progress than ETG, even though ETG contributes more to bottom-up cracking development.
- Equivalent joint stiffness, base modulus, and subbase modulus Inputs are categorized as insensitive for all stress responses under different loading conditions, showing that the variation of these input parameters has less significant effect than other parameters on either top-down or even bottom-up cracking.

- For the mechanical-loading-only case under critical loading conditions, the critical principal stress at the bottom of the PCC slab is most sensitive to PCC slab thickness.
- For the simultaneous mechanical and thermal loading case under critical loading conditions, the ETG, thermal coefficient, PCC slab thickness and modulus, subgrade modulus, base thickness, and subbase thickness are all effective inputs for both top and bottom shear stresses.
- PCC thickness, base thickness, subbase thickness, subgrade modulus, and PCC modulus are the five most effective input parameters for tensile stresses at top of the slab ($\sigma_{XX\text{-}Max\text{-}Top\text{-}Tens.}$, $\sigma_{YY\text{-}Max\text{-}Top\text{-}Tens.}$, and $\sigma_{1\text{-}Max\text{-}Top\text{-}Tens.}$) under mechanical loading only; the least effective input parameter is equivalent joint stiffness.
- For simultaneous temperature and mechanical loading conditions, PCC thickness, PCC modulus, thermal coefficient, temperature gradient, and base thickness are the five most effective parameters for top tensile stresses. For combined loading conditions PCC slab properties and the temperature inputs make the greatest contribution, and for mechanical loading only the PCC slab properties and sublayer thickness variation make a significant contribution to top-down cracking advancement.

References

[1] H. Ceylan, S. Kim, K. Gopalakrishnan, C. W. Schwartz, and R. Li, "Sensitivity Analysis Frameworks for Mechanistic-Empirical Pavement Design of Continuously Reinforced Concrete Pavements," Constr. Build. Mater. vol. 73, pp. 498–508, 2014.

[2] H. Ceylan, S. Kim, K. Gopalakrishnan, C. W. Schwartz, and R. Li, "Sensitivity quantification of jointed plain concrete pavement mechanistic-empirical performance predictions," Constr. Build. Mater. vol. 43, pp. 545–556, 2013.

[3] C. Schwartz, R. Li, H. Ceylan, S. Kim, and K. Gopalakrishnan, "Global sensitivity analysis of mechanistic-empirical performance predictions for flexible pavements," Transp. Res. Rec. J. Transp. Res. Board, no. 2368, pp. 12–23, 2013.

[4] C. W. Schwartz, R. Li, S. Kim, H. Ceylan, and K. Gopalakrishnan, "Sensitivity evaluation of MEPDG performance prediction," 2011.

[5] T. Merhej and D. Feng, "Parameter Sensitivity Analysis of Airport Rigid Pavement Thickness Using FAARFIELD Program," Adv. Mater. Res., pp. 243–249, 2011.

[6] A. Guclu, H. Ceylan, K. Gopalakrishnan, and S. Kim, "Sensitivity Analysis of Rigid Pavement Systems Using the Mechanistic-Empirical Design Guide Software," J. Transp. Eng. ASCE, vol. 8, pp. 555–562, 2009.

[7] H. Ceylan, K. Gopalakrishnan, S. Kim, C. Schwartz, and R. Li, "Global sensitivity analysis of jointed plain concrete pavement mechanistic-empirical performance predictions," Transp. Res. Rec. J. Transp. Res. Board, no. 2367, pp. 113–122, 2013.

[8] 2002 Design Guide: Design of New and Rehabilitated Pavement Structures. Draft Final Report for NCHRP Study 1-37A. Washington, D.C.: NCHRP, Transportation Research Board of the National Academies, 2004.

[9] Y. Chen, Q. Wang, and D. R. Brill, "Critical Stress Analysis of Large Aircraft on Airport Rigid Pavement Using FEAFAA," in 10th International Conference on Concrete PavementsInternational Society for Concrete PavementsHolcim (Canada) Transports Quebec, 2012.

[10] Y. Chen, "4-Slab Three Dimensional Finite Element Method Model in FAARFIELD," 2014.

[11] Q. Wang and Y. Chen, "Improvements to Modeling of Concrete Slab Curling by Using NIKE3D Finite Element Program," Transp. Res. Rec. J. Transp. Res. Board, vol. 2226, no. 1, pp. 71–81, 2011.

CHAPTER 3. DEVELOPMENT OF RAPID ANALYSIS TOOL FOR RIGID AIRFIELD PAVEMENT SYSTEMS

Abstract

Three-dimensional Finite Element (3D-FE) stress computations involved in the current rigid airport pavement design methodology (i.e., the FAA Rigid and Flexible Iterative Elastic Layered Design (FAARFIELD) software), are time consuming when considering top-down cracking failure mode, so ongoing studies at Iowa State University (ISU) are developing surrogate response models using Artificial Neural Networks (ANNs) to replace such 3D-FE computations. In this study, ANN models are integrated into a tool called ANN based FAA rigid pavement analysis tool (ANNFAA) with a user-friendly Graphical-User Interface (GUI). ANNFAA makes use of the best ANN models developed in MATLAB for 156 different airplanes without requiring any additional software installation or cumbersome learning of a new program. Within ANNFAA development, about 4,000 of 3D-FE simulations and many ANN models have been developed for each of these airplanes. Three useful tools were also created using C# and MATLAB for implementing the 3D-FE analysis, post-processing the results, training the ANN models, and determining accuracy and performance of the ANN models. ANNFAA provides an accurate and very fast procedure for practitioners, engineers, and researchers for computing the most critical stress responses associated with top-down cracking in multiple-slab rigid airfield pavements. This should help make pavement design and analysis more practical, especially when a significantly large number of different cases that include top-down cracking failure mode are investigated, as well as when bottom-up cracking mode currently used in the FAA standard rigid pavement design procedures is being considered in a design.

Introduction

The significant potential of artificial intelligence (AI) techniques in solving resource-intensive complex problems has increased interest in using such methods in different engineering areas, including civil engineering fields such as structural engineering, environmental and water resources engineering, traffic engineering, geotechnical engineering, and pavement engineering. During recent decades, artificial neural networks (ANN) is an AI technique that has become popularly used not only in research activities but also in commercial applications.

ANN has been addressed to a wide variety of pavement engineering issues associated with design, analysis, distress evaluation, performance, maintenance, rehabilitation, and management of both highway and airport pavements (flexible, rigid, and composite) [1]–[9]. Use of ANN in many research studies related to pavement engineering has shown that ANN holds promise for use in investigating, modelling, and seeking better understanding of many complex and non-linear pavement engineering problems and mechanisms, including some that have not yet been well understood and formulated [1]–[9]. Neural networks have been found to be very reliable and versatile computational tools for determining and predicting future condition and performance of existing pavement systems related to maintenance and rehabilitation decision making actions for deteriorated pavement sections, developing cost-effective prediction models for estimating the future condition of a pavement section, predicting properties of pavement layers and pavement surfaces, and understanding and characterizing Portland cement concrete (PCC) and asphalt cement concrete (ACC) design and behavior [9], [10].

One reason for using ANN is to try to avoid long and unpredictable analysis running times associated with the multiple-slab model and curled slabs addressed in a 3D-finite

element (FE) computer program called NIKE3D_FAA [11], [12], currently employed in the FAA Rigid and Flexible Iterative Elastic Layered Design (FAARFIELD) software for rigid pavement design. Note that FAARFIELD 1.42 is the latest version of standard thickness design software accompanying AC 150/5320-6F Airport Pavement Design and Evaluation [11], and NIKE3D_FAA is a modification of the NIKE3D program originally developed by the Lawrence Livermore National Laboratory (LLNL) of the U.S. Department of Energy [11], [12]. The FAA has also developed Finite Element Analysis FAA (FEAFAA) software that makes use of NIKE3D_FAA as a stand-alone tool for 3D-finite element (3D-FE) analysis of multiple-slab rigid airport pavements and overlays. Incorporating ANN surrogate response models into the rigid pavement design process can significantly reduce the iteration time for calculating critical responses of each type of aircraft in mixed aircraft traffic loading and significantly help with more efficient implementation of the whole routine design process.

The primary objective of this chapter is to develop a comprehensive tool employing the surrogate computational response models published by the authors in previous studies [6], [7], and [13]. This new tool will be suitable for implementation in next generation of FAA thickness design software, FAARFIELD 2.0, and it will also provide a close estimate of the top-down bending stress computed by NIKE3D_FAA both for mechanical loading only and combined airplane and temperature loading of rigid airport pavements. This will enable faster 3D-FE computations of design stresses in FAARFIELD 2.0. Figure 3.1 simply demonstrates the contribution of this study's outcomes in the iterative process of the rigid airfield pavement thickness design in the FAARFIELD. The new ANN based FAA rigid pavement analysis tool (ANNFAA) developed in this study can be used in the design process

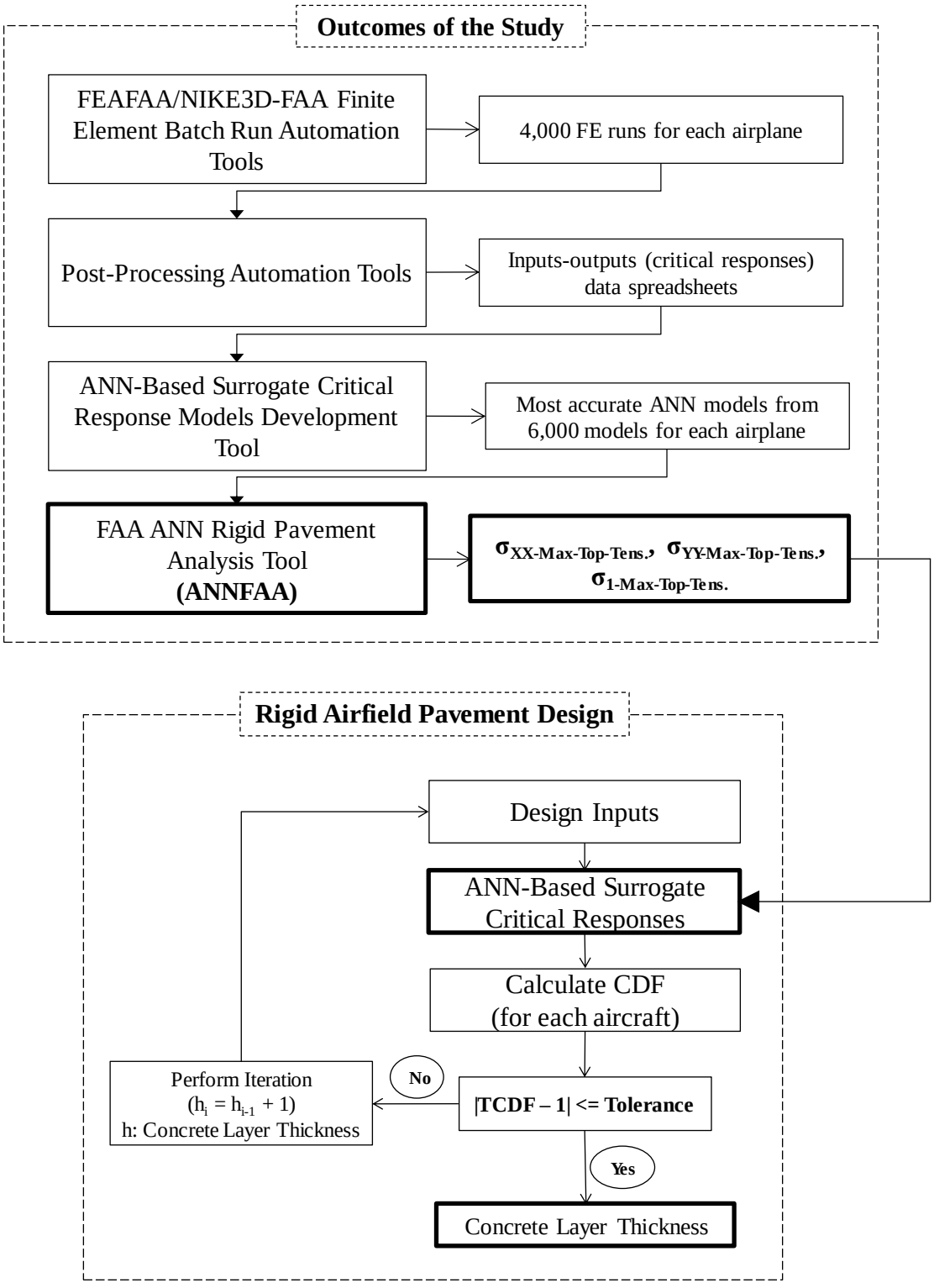

Figure 3.1 *Flowchart displaying the contribution of this study in FAA rigid airfield pavement design.*

instead of 3D-FE analysis can predict the critical stresses, i.e., the maximum horizontal stresses at the slab surfaces. The damage factor (DF), the ratio of tensile strength (R) to the critical stress value, is then determined, followed by computation of a cumulative damage factor (CDF) for each type of aircraft in the applied aircraft traffic mix. The desired design thickness is achieved when the total CDF (TCDF) either reaches 1 or meets the tolerance; otherwise the PCC thickness is incremented ($h_i = h_i + 1$) and another iteration performed.

Synthetic Database Development

A synthetic database consisting of FEAFAA input parameters and associated critical pavement responses was created as part of ANN-based surrogate computational response model development using the following automated process:

Step 1: Generate several cases with randomly generated FEAFAA input parameters within specified ranges

Step 2: Run FEAFAA one case at a time

Step 3: Extract critical pavement responses from FEAFAA output file

Step 4: Enter the extracted critical pavement responses into the database

Step 5: Repeat steps 2-4 for all the cases generated in step 1

In the FEAFAA batch runs, ANN models were developed for two different load cases: Case 1: mechanical-load-only, and Case 2: simultaneous mechanical and temperature loading.

Finite Element Mesh Size

Before developing a data base for each type of aircraft sensitivity analysis was carried out to determine the suitable number of elements for finite element modelling by NIKE3D-FAA. Figure 3.2 shows the changes in maximum tensile stress responses at top of the slab ($\sigma_{XX\text{-}Max\text{-}Top\text{-}Tens.}$) with respect to variation in number of elements for slab and foundation

layers. Figure 3.2 (a) shows the stress variation under A380-800 gear loading (only a six wheel-gear) and Figure 3.2 (b) displays the stress variation under B777-300 ER loading. As the number of elements of both the foundation and the slab increases, the stresses converge to a specific value. From Figure 3.2 (a), it is obvious that, for fewer than 30 foundation elements, the results are not constant, but for more than 30 the results converge. From Figure 3.2 (b), it can be determined that, for 25 to 45 foundation elements and 30 to 50 slab elements the stress value is approximately constant.

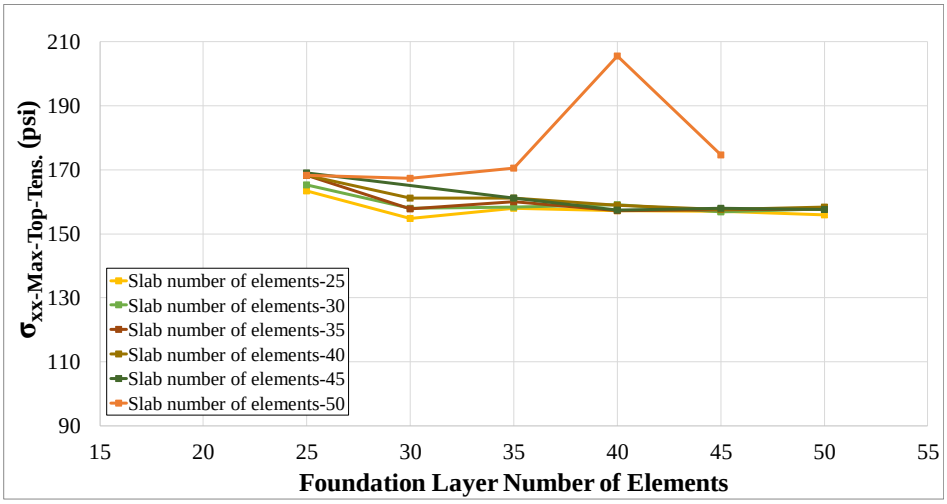

(a)

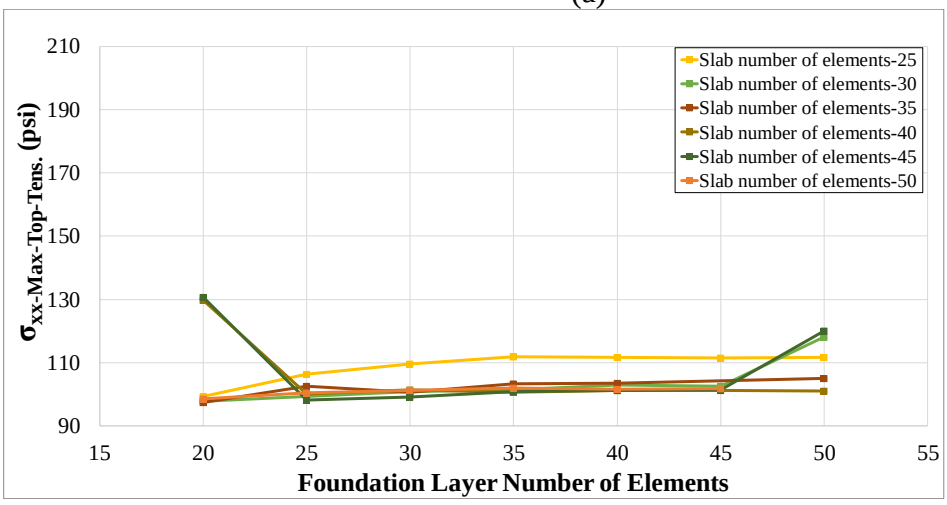

(b)

Figure 3.2 *$\sigma_{XX\text{-}Max\text{-}Top\text{-}Tens.}$ changes vs. foundation number of elements and slab number of elements for (a) A380-800 and (b) B777-300 ER mechanical loading only.*

Figure 3.3 shows $\sigma_{XX\text{-}Max\text{-}Top\text{-}Tens.}$ variation with respect to changes in number of elements for slabs and foundation layers under simultaneous temperature and mechanical loading Figure 3.3 (a) shows stress variation under A380-800 gear loading and Figure 3.3 (b) shows stress variation under B777-300 ER loading. Figure 3.3 (a) shows that, for 30 to 45 foundation elements and 25 to 45 slab elements, the critical stress converges to a constant value. Figure 3.3 (b) also shows that, for 30 to 50 foundation elements and 25 to 40 slab elements, the stress does not appreciably change.

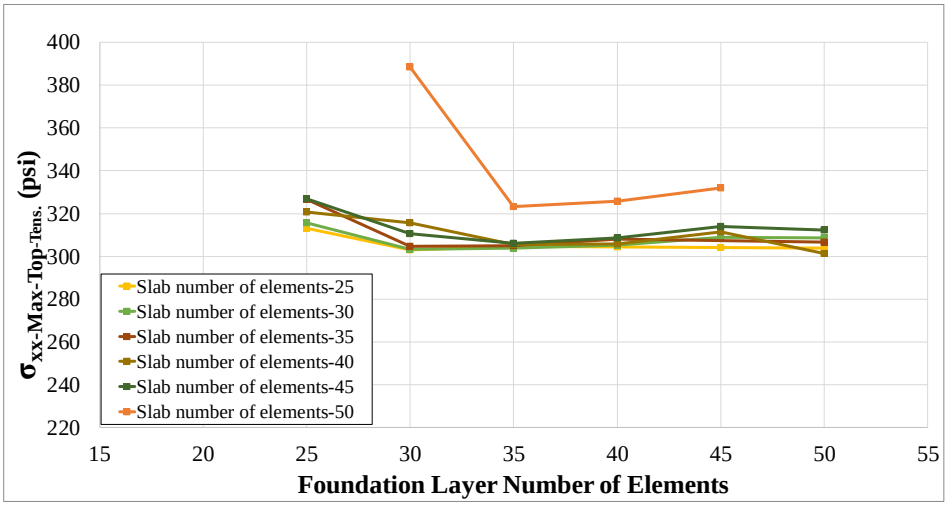

(a)

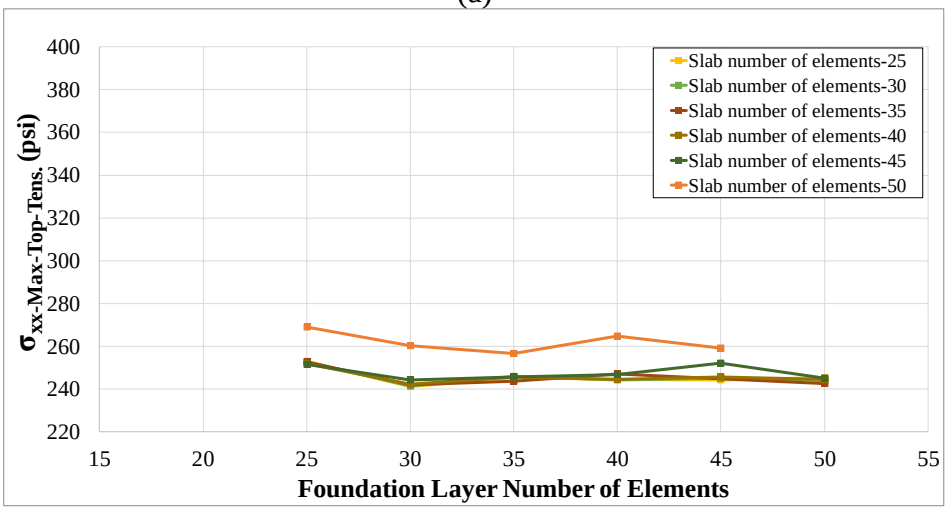

(b)

Figure 3.3 *$\sigma_{XX\text{-}Max\text{-}Top\text{-}Tens.}$ changes vs. foundation number of elements and slab number of elements for simultaneous (a) A380-800 and (b) B777-300 ER mechanical loading and temperature loading.*

Table 3.1 presents the average computation time required for mesh generation and analysis for 30 and 40 elements for foundation and slab. Increasing the number of elements can dramatically increase NIKE3D run time. An optimum number of 30 elements was selected for meshing both the slab and foundation as a compromise between speed and accuracy.

Table 3.1 *Mesh size vs. average computation time.*

Case Type		**Mechanical Loading Only Case**		**Temperature + Mechanical Loading Case**	
		Slab Number of Element: 30 Foundation, Number of Element: 30	**Slab Number of Element: 40, Foundation Number of Element: 40**	**Slab Number of Element: 30, Foundation Number of Element: 30**	**Slab Number of Element: 40, Foundation Number of Element: 40**
Average Computation Time for One Case (Minutes)	Input Generation	1.1	1.7	1.3	2.3
	Output Generation	2.5	6.2	7.7	28.0
	Total	3.6	7.9	9.0	30.7

Finite-Element-Based Database Development

In developing the database, 2,000 samples (cases) were populated with randomly-assigned numbers within predefined ranges for each input parameter. The next sections discuss in detail how the required case numbers were determined and populated. The predefined ranges were based on a combination of FEAFAA's hard-coded ranges and engineering judgment. Table 3.2 shows the inputs and their ranges used in the development of the finite-element-based knowledge database. The loading angle in Table 3.2 is the angle of inclination between the aircraft gear and the Y-axis (see Figure 3.4).

In reality, most random numbers used in computer programs are pseudo-random, meaning that they are generated in a predictable fashion using a mathematical formula, and artificial neural networks can easily learn the underlying structure of a data set created by predictable pseudo-random numbers. Using a random seed number and differing functions for generating random numbers will help create true random numbers.

MATLAB includes different random number generators such as: Mersenne Twister (twister), SIMD-oriented Fast Mersenne Twister (simdTwister), Combined Multiple Recursive (combRecursive), Multiplicative Lagged Fibonacci (multFibonacci), Legacy MATLAB 5.0 uniform generator (v5uniform), and Legacy MATLAB 4.0 generator (v4).

During random number generation, the starting point in the sequence is determined by a seeds, and if the same seed is used each time, it will yield the same sequence of "random numbers". To address this issue, in this study different seeds based on the time of the computer system were generated for each random number sequence. Tables3.3 and 3.4 show correlation of the randomly generated inputs for mechanical only loading and temperature-mechanical loading cases, respectively. The correlation values show that the random generation technique used in this study works well so that it can make really independent inputs. Correlation coefficient range is between -1 to 1, where correlation coefficient value of 1 means that inputs are highly correlated, whereas correlation coefficient value of 0 means that there is no correlation. Based on the inputs correlation presented in Table 3.3, the inputs that has correlation coefficient less than 0.1 are assumed effectively independent.

Table 3.2 *Ranges of input parameters used for producing finite element analysis runs.*

Inputs		**Ranges**	
		Min	**Max**
PCC Slab	Modulus (GPa) (psi)	20.7 (3×10^6)	48.3 (7×10^6)
	Thickness (cm.) (in.)	15.2 (6)	60.9 (24)
	Poisson Ratio	0.10	0.20
Base	Modulus (GPa) (psi)	1.4 (2×10^5)	13.8 (2×10^6)
	Thickness (cm.) (in.)	10.0 (4)	76.2 (30)
	Poisson Ratio	0.15	0.25
Granular Subbase	Modulus (GPa) (psi)	1×10^{-1} (15,000)	5.2×10^{-1} (75,000)
	Thickness (cm.) (in.)	15.2 (6)	127 (50)
	Poisson Ratio	0.20	0.40
Subgrade	Modulus (GPa) (psi)	2.1×10^{-2} (3,000)	3.4×10^{-1} (50,000)
	Poisson Ratio	0.30	0.45
Slab Dimension (m.) (ft.)		4.6 (15)	9.1 (30)
Slab Number of Elements		30	
Number of Slabs		9	
Foundation Number of Elements		30	
Loading Angle Θ_g		0	90
Temperature Gradient (°C/cm) (°F/in.)		-0.3 (-2)	+0.3 (2)
Thermal Coefficient (1/ °C) (1/°F)		7.4×10^{-6} (4.1×10^{-6})	12.9×10^{-6} (7.2×10^{-6})
Equivalent Joint Stiffness (GPa/m) (psi/in)		2.7×10^{-1} (1.0×10^3)	162.6 (6.0×10^5)

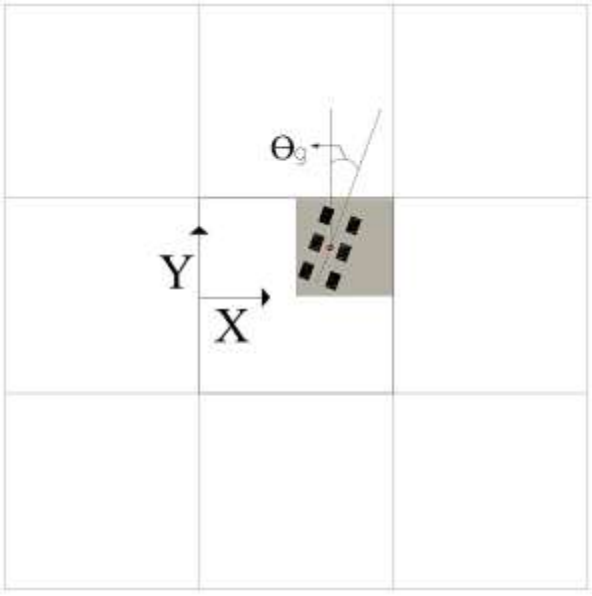

Figure 3.4 *Load position and slabs configuration.*

Table 3.3 *Correlation of the inputs for mechanical only loading case.*

	PCC Slab Modulus	PCC Slab Poisson Ratio	PCC Slab Thickness	Subbase1 Modulus	Subbase1 Poisson Ratio	Subbase1 Thickness	Subbase2 Modulus	Subbase2 Poisson Ratio	Subbase2 Thickness	Subgrade Modulus	Subgrade Poisson Ratio	X Dimension	Y Dimension	Loading Angel	X-offset	Y-offset	JointSX
PCC Slab Modulus	1	-0.010	0.022	-0.040	-0.002	-0.030	-0.048	-0.023	0.011	0.015	-0.020	-0.012	0.018	0.015	-0.003	-0.053	-0.034
PCC Slab Poisson Ratio	-0.010	1	0.013	-0.023	0.010	-0.014	-0.003	0.031	-0.010	0.013	0.015	-0.023	-0.050	-0.014	-0.013	-0.019	-0.011
PCC Slab Thickness	0.022	0.013	1	-0.022	0.028	-0.046	0.003	0.001	-0.013	0.093	0.032	0.035	0.021	-0.037	0.023	0.011	0.073
Subbase1 Modulus	-0.040	-0.023	-0.022	1	0.005	-0.012	-0.018	-0.014	-0.040	0.015	0.029	0.004	-0.005	0.053	0.015	0.040	-0.006
Subbase1 Poisson Ratio	-0.002	0.010	0.028	0.005	1	0.021	-0.042	0.025	-0.002	-0.043	0.038	-0.040	-0.014	-0.023	-0.029	0.020	-0.013
Subbase1 Thickness	-0.030	-0.014	-0.046	-0.012	0.021	1	-0.016	-0.041	-0.026	0.016	0.045	0.056	0.035	0.025	0.034	0.023	-0.007
Subbase2 Modulus	-0.048	-0.003	0.003	-0.018	-0.042	-0.016	1	0.004	-0.052	0.133	0.015	0.027	0.013	-0.015	-0.024	0.028	-0.017
Subbase2 Poisson Ratio	-0.023	0.031	0.001	-0.014	0.025	-0.041	0.004	1	-0.028	-0.019	0.062	-0.008	0.005	-0.018	0.014	0.009	-0.027
Subbase2 Thickness	0.011	-0.010	-0.013	-0.040	-0.002	-0.026	-0.052	-0.028	1	0.039	-0.021	-0.005	-0.013	-0.019	0.019	-0.017	-0.019
Subgrade Modulus	0.015	0.013	0.093	0.015	-0.043	0.016	0.133	-0.019	0.039	1	-0.014	0.045	0.023	0.011	0.010	0.021	-0.005
Subgrade Poisson Ratio	-0.020	0.015	0.032	0.029	0.038	0.045	0.015	0.062	-0.021	-0.014	1	-0.016	-0.010	0.010	-0.013	-0.037	0.032
X Dimension	-0.012	-0.023	0.035	0.004	-0.040	0.056	0.027	-0.008	-0.005	0.045	-0.016	1	0.599	-0.004	0.637	0.154	-0.041
Y Dimension	0.018	-0.050	0.021	-0.005	-0.014	0.035	0.013	0.005	-0.013	0.023	-0.010	0.599	1	0.025	0.378	0.273	-0.041
Loading Angel	0.015	-0.014	-0.037	0.053	-0.023	0.025	-0.015	-0.018	-0.019	0.011	0.010	-0.004	0.025	1	-0.010	0.022	-0.011
X-offset	-0.003	-0.013	0.023	0.015	-0.029	0.034	-0.024	0.014	0.019	0.010	-0.013	0.637	0.378	-0.010	1	-0.051	-0.024
Y-offset	-0.053	-0.019	0.011	0.040	0.020	0.023	0.028	0.009	-0.017	0.021	-0.037	0.154	0.273	0.022	-0.051	1	-0.013
JointSX	-0.034	-0.011	0.073	-0.006	-0.013	-0.007	-0.017	-0.027	-0.019	-0.005	0.032	-0.041	-0.041	-0.011	-0.024	-0.013	1

To develop an extensive database of input-output records from FEAFAA 2.0, automation programs were required to reduce required time, increase accuracy, and decrease human interaction. Two tools were developed: one for batch runs of NIKE3D-FAA, and one for post-processing the results (where post-processing means using the raw output files generated by NIKE3D and NIKE-Plot to find maximum and minimum responses and their locations).

Table 3.4 *Correlation of the inputs for temperature + mechanical loading case.*

	PCC Slab Modulus	PCC Slab Poisson Ratio	PCC Slab Thickness	Subbase1 Modulus	Subbase1 Poisson Ratio	Subbase1 Thickness	Subbase2 Modulus	Subbase2 Poisson Ratio	Subbase2 Thickness	Subgrade Modulus	Subgrade Poisson Ratio	X Dim.	Y Dim.	Loading Angel	X-off.	Y-off.	Temperature Gradient	Thermal Coefficient	JointSX
PCC Slab Modulus	1	-0.016	0.022	-0.047	0.001	-0.044	-0.046	-0.002	0.005	0.021	-0.023	-0.004	0.021	0.004	-0.021	-0.008	-0.019	0.028	-0.019
PCC Slab Poisson Ratio	-0.016	1	-0.003	-0.026	-0.003	0.001	0.003	0.021	-0.005	0.028	0.008	0.002	-0.029	-0.009	0.014	0.006	-0.003	-0.015	-0.013
PCC Slab Thickness	0.022	-0.003	1	-0.010	0.016	-0.006	0.004	-0.010	0.008	0.033	0.015	0.010	-0.002	-0.028	0.024	0.015	0.013	-0.011	0.055
Subbase1 Modulus	-0.047	-0.026	-0.010	1	0.004	0.008	-0.015	0.008	-0.034	-0.007	0.021	-0.006	-0.021	0.054	0.015	0.024	0.041	0.018	0.016
Subbase1 Poisson Ratio	0.001	-0.003	0.016	0.004	1	0.023	-0.035	0.015	-0.005	-0.059	0.022	-0.042	-0.027	-0.033	-0.032	0.011	0.033	-0.010	-0.006
Subbase1 Thickness	-0.044	0.001	-0.006	0.008	0.023	1	-0.041	-0.039	0.006	-0.048	0.028	0.040	0.023	0.033	0.025	-0.003	0.028	0.005	-0.020
Subbase2 Modulus	-0.046	0.003	0.004	-0.015	-0.035	-0.041	1	-0.011	-0.074	0.157	0.016	0.030	0.013	-0.010	0.025	-0.013	0.015	0.027	-0.008
Subbase2 Poisson Ratio	-0.002	0.021	-0.010	0.008	0.015	-0.039	-0.011	1	-0.010	-0.028	0.059	-0.001	0.013	-0.013	0.022	0.034	0.023	-0.034	-0.028
Subbase2 Thickness	0.005	-0.005	0.008	-0.034	-0.005	0.006	-0.074	-0.010	1	-0.015	-0.024	-0.014	-0.025	-0.006	0.011	-0.015	-0.021	-0.035	-0.025
Subgrade Modulus	0.021	0.028	0.033	-0.007	-0.059	-0.048	0.157	-0.028	-0.015	1	0.012	0.065	0.053	-0.004	0.045	0.013	-0.011	0.038	0.003
Subgrade Poisson Ratio	-0.023	0.008	0.015	0.021	0.022	0.028	0.016	0.059	-0.024	0.012	1	-0.020	0.000	0.021	-0.016	-0.032	0.001	0.019	0.021
X Dimension	-0.004	0.002	0.010	-0.006	-0.042	0.040	0.030	-0.001	-0.014	0.065	-0.020	1	0.602	0.003	0.716	0.199	-0.031	0.019	-0.047
Y Dimension	0.021	-0.029	-0.002	-0.021	-0.027	0.023	0.013	0.013	-0.025	0.053	0.000	0.602	1	0.022	0.436	0.315	-0.018	0.028	-0.041
Loading Angel	0.004	-0.009	-0.028	0.054	-0.033	0.033	-0.010	-0.013	-0.006	-0.004	0.021	0.003	0.022	1	-0.008	0.014	-0.016	0.015	-0.016
X-offset	-0.021	0.014	0.024	0.015	-0.032	0.025	0.025	0.022	0.011	0.045	-0.016	0.716	0.436	-0.008	1	0.158	-0.029	0.012	-0.024
Y-offset	-0.008	0.006	0.015	0.024	0.011	-0.003	-0.013	0.034	-0.015	0.013	-0.032	0.199	0.315	0.014	0.158	1	-0.010	0	-0.024
Temperature Gradient	-0.019	-0.003	0.013	0.041	0.033	0.028	0.015	0.023	-0.021	-0.011	0.001	-0.031	-0.018	-0.016	-0.029	-0.010	1	-0.030	0
Thermal Coefficient	0.028	-0.015	-0.011	0.018	-0.010	0.005	0.027	-0.034	-0.035	0.038	0.019	0.019	0.028	0.015	0.012	0	-0.030	1	0.008
JointSX	-0.019	-0.013	0.055	0.016	-0.006	-0.020	-0.008	-0.028	-0.025	0.003	0.021	-0.047	-0.041	-0.016	-0.024	-0.024	0	0.008	1

Batch Run Automation

Suitable automation programs were selected based on features needed and capabilities of the software in performing batch runs. Since the automation program chosen should be able to simulate mouse movements and keyboard operations and should also be easy to run on a wide variety of computers, capability of compilation to an executable (exe.) file is necessary. Among the various software types mentioned above, AutoIt [14] was identified as meeting major requirements for FEAFAA's batch runs.

To establish an integrated platform for the automation program devising a powerful automation program scheme, AutoIt library was combined in C# programming language. The final product of this combination can automatically perform FEAFAA, save input files, run NIKE3D, and save the output files for each case. It can execute several NIKE3D task, simultaneously. The graphical interface for the batch run program is shown in Figure 3.5.

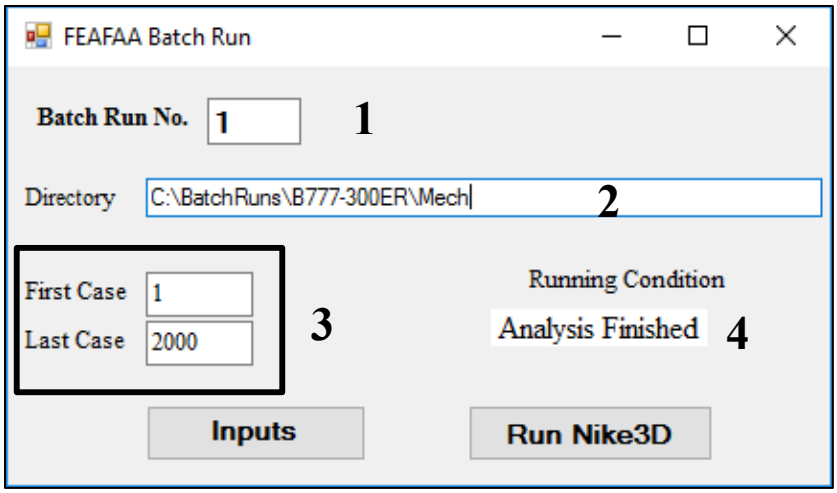

1. Batch run number for multiple runs
2. Directory of FEAFAA, inputs, and outputs
3. Range of cases for running in FEAFAA
4. Shows which case is running or finished

Figure 3.5 *Graphical interface of batch run program.*

A post processing program, also written in C#, is able to analyze all output values, calculate maximum and minimum stresses components and deflection for each case, and find critical response locations.

NIKE3D generates two files, *n3dhsp* and *Nike3d.txt*. Output file *n3dhsp* contains all input and output data, including pavement stress responses at element integration points and nodal displacements. The FEAFAA installation package contains a post-analysis processing program called NIKEPLOT that reads the *n3dhsp* output file and extrapolates the computed stresses to the nodal points. NIKEPLOT generates new data files in a simple format that can be easily read and displayed by commercial 3D finite-element post-processing programs, such as TecPlot 360 EX [15] (Figure 3.7). The two data files in ASCII-format are

model_load.dat and *model_stress_1.dat*. The first file contains all information about the 3D model, including geometric data, load, and boundary conditions. The second file also contains the geometric data, as well as the 6 components of computed stress (extrapolated to the nodes) and the von Mises stress (a stress invariant). The developed post processing utility can determine critical stresses by reading the *model_stress_1.dat* file then gather all information into a excel spreadsheet. The top and bottom slab responses are separated, and the critical responses and their locations can be separately determined for top or bottom. In addition, for each case, the sign of critical normal stresses, tensile or compressive, is reported. Figure 3.6 shows the graphical interface of the post-processing utility and Table 3.5 presents a list of all critical responses provided by the post-processing utility.

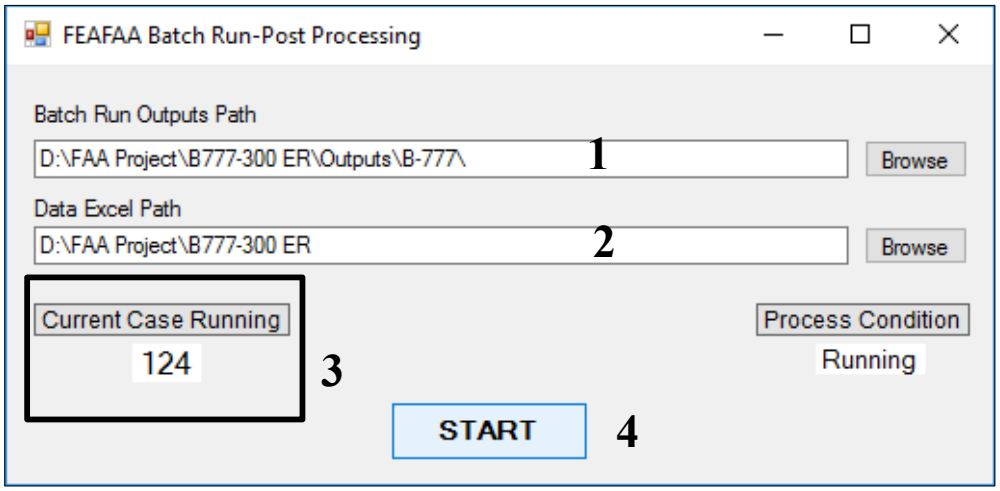

1. Directory of output files generated by NIKEPLOT
2. Directory of datasets spreadsheet
3. Currently running case
4. Start post-processing

Figure 3.6 *GUI of FEAFAA batch run post-processing utility.*

Table 3.5 *Post-processing outcomes.*

Response	**Definition/Symbol**	
Deflection	Maximum	D_{Max}
	Minimum	D_{Min}
Maximum Normal Stresses	Tensile	$\sigma_{xx\text{-}Max\text{-}Tens.}$
	Compressive	$\sigma_{xx\text{-}Max\text{-}Com.}$
	Tensile	$\sigma_{yy\text{-}Max\text{-}Tens.}$
	Compressive	$\sigma_{yy\text{-}Max\text{-}Com.}$
	Tensile	$\sigma_{zz\text{-}Max\text{-}Tens.}$
	Compressive	$\sigma_{zz\text{-}Max\text{-}Com.}$
Maximum Shear Stresses	Maximum	$\sigma_{xy\text{-}Max}$
	Minimum	$\sigma_{xy\text{-}Min}$
	Maximum	$\sigma_{yz\text{-}Max}$
	Minimum	$\sigma_{yz\text{-}Min}$
	Maximum	$\sigma_{zx\text{-}Max}$
	Minimum	$\sigma_{zx\text{-}Min}$
Maximum Von Mises		$\sigma_{Mises\text{-}Max}$
Maximum Principals Stresses	Tensile	$\sigma_{1\text{-}Max\text{-}Tens.}$
	Compressive	$\sigma_{1\text{-}Max\text{-}Com.}$
	Tensile	$\sigma_{2\text{-}Max\text{-}Tens.}$
	Compressive	$\sigma_{2\text{-}Max\text{-}Com.}$

Principal stresses (σ_1 and σ_2) are first calculated at each nodal point of the finite element model, followed by determination of maximum principal stresses at top and bottom of the slab and corresponding principal stress angle Θ_p.

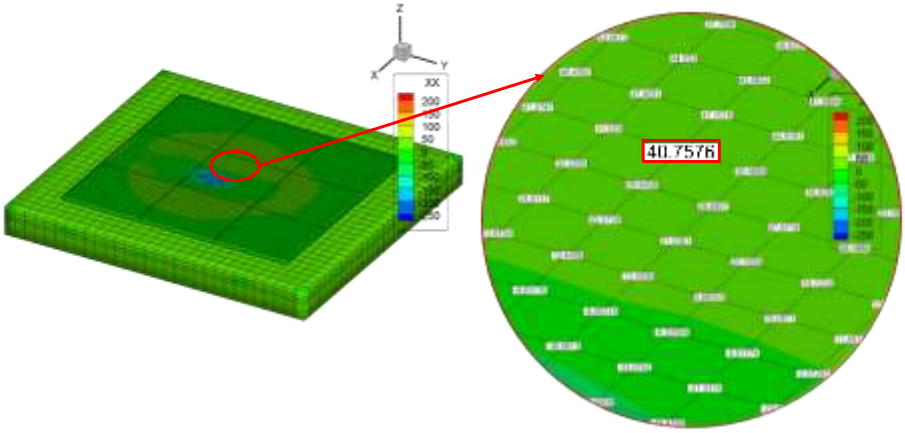

Figure 3.7 *3D finite element model of the pavement structure used in NIKE3D plotted by TecPlot 360 EX.*

ANN Model Development Approaches

The project team trained artificial neural network response models by using various architectures and training algorithms. Both one and two hidden layer architectures with numbers of neurons varying from 5 to 50, and five different algorithms were used. In order to avoid being caught at a local minimum, the training process of each ANN model were restarted at 10 different initial conditions. It leads the ANN to start from a new point in the error surface and consequently to find the desired global minimum error on the entire error domain. Otherwise, ANN will be trapped in a minimum error at the near neighborhood called local minimum.

Considering various algorithms and architectures, totally 1,000 ANN models were developed for each critical response ($\sigma_{XX\text{-}Max\text{-}Top\text{-}Tens.}$, $\sigma_{YY\text{-}Max\text{-}Top\text{-}Tens.}$, and $\sigma_{1\text{-}Max\text{-}Top\text{-}Tens.}$). Since two loading conditions were used, ultimately 6,000 ANN models (number of responses × loading condition× ANN models developed for each response = 3 × 2× 1,000) were developed for each aircraft loading. To generate this number of ANN models for each of the 156 aircraft provided in FEAFAA 2.0, an ANN model development tool was created in MATLAB.

The project team wrote a utility program in MATLAB to import data, train the models, and export and find the optimum models. Automating data import significantly reduces the chance of mistakes during manually data entry.

Some features of the ANN model development tool are:

- Creating a database of all trained ANN models
- Training ANN models using various algorithms
- Including a range of hidden layer sizes

- Developing ANN models in both single mode and batch mode
- Developing any single ANN model (e.g., for any response and a specific algorithm and hidden layer size)
- Developing several different ANN models (e.g., for all responses with different algorithm and various hidden layer sizes)
- Calculating accuracy parameters (R^2, RMSE, AAE) for each ANN model, to be compared with NIKE3D solutions for selecting the most accurate model for each response
- Exporting the most accurate ANN model results into spreadsheets.

The utility program executes three main steps:

- Step1: Creating workspace for all inputs and outputs
- Step2: Training ANN models
- Step3: Optimizing and exporting the data

Creating Workspace

The first step in developing the ANN models is to create the input and output matrix. Figure 3.8 displays the graphical user interface of the computer program the project team wrote for this purpose. The source file used for creating the inputs and outputs matrix is the spreadsheet obtained from post-processing of FE analysis outputs. Since there are 17 inputs for mechanical-loading-only cases, and 19 inputs for simultaneous mechanical and temperature loading, the type of loading must first be specified to determine the number of inputs. At the first step, a matrix of all cases used for developing ANN models is created and a specified percentage of all cases is randomly chosen for independent testing purposes. The first step is terminated when a MATLAB file (workspace)containing input and output

matrices both for developing ANN models and independent testing has been created. Results obtained by conducting subsequent steps are saved in the workspace created during the first step.

Training ANN Models

The second step for developing ANN models is training the ANN models. Figure 3.8 displays all actions required for training ANNs by the program. Before starting training, the responses for which the ANN model is being developed are selected. There are 12 critical responses available in the program to for developing ANN models: Critical tensile stresses at *x* and *y* directions (σ_{xx}, σ_{yy}), Von Mises, deflection, and principal stresses (σ_1 and σ_2) at top and bottom of the PCC slab.

Another important option provided in the program is a training algorithm. As illustrated in Figure 3.8, from 10 different algorithms considered for training the neural network models, five high-performance backpropagation training algorithms were used to develop the models (Table 3.6). These algorithms use standard numerical optimization techniques such as Conjugate Gradient (Fletcher-Reeves Update (CGF), Polak-Ribiére Update (CGP), and Powell-Beale Restarts (CGB)), One-step Secant (OSS), and Levenberg-Marquardt (LM) algorithms. In the basic backpropagation algorithm, the weights are adjusted along the steepest descent (negative gradient), while in the conjugate gradient algorithms a search is performed along conjugate directions, producing generally faster convergence than steepest descent [16].

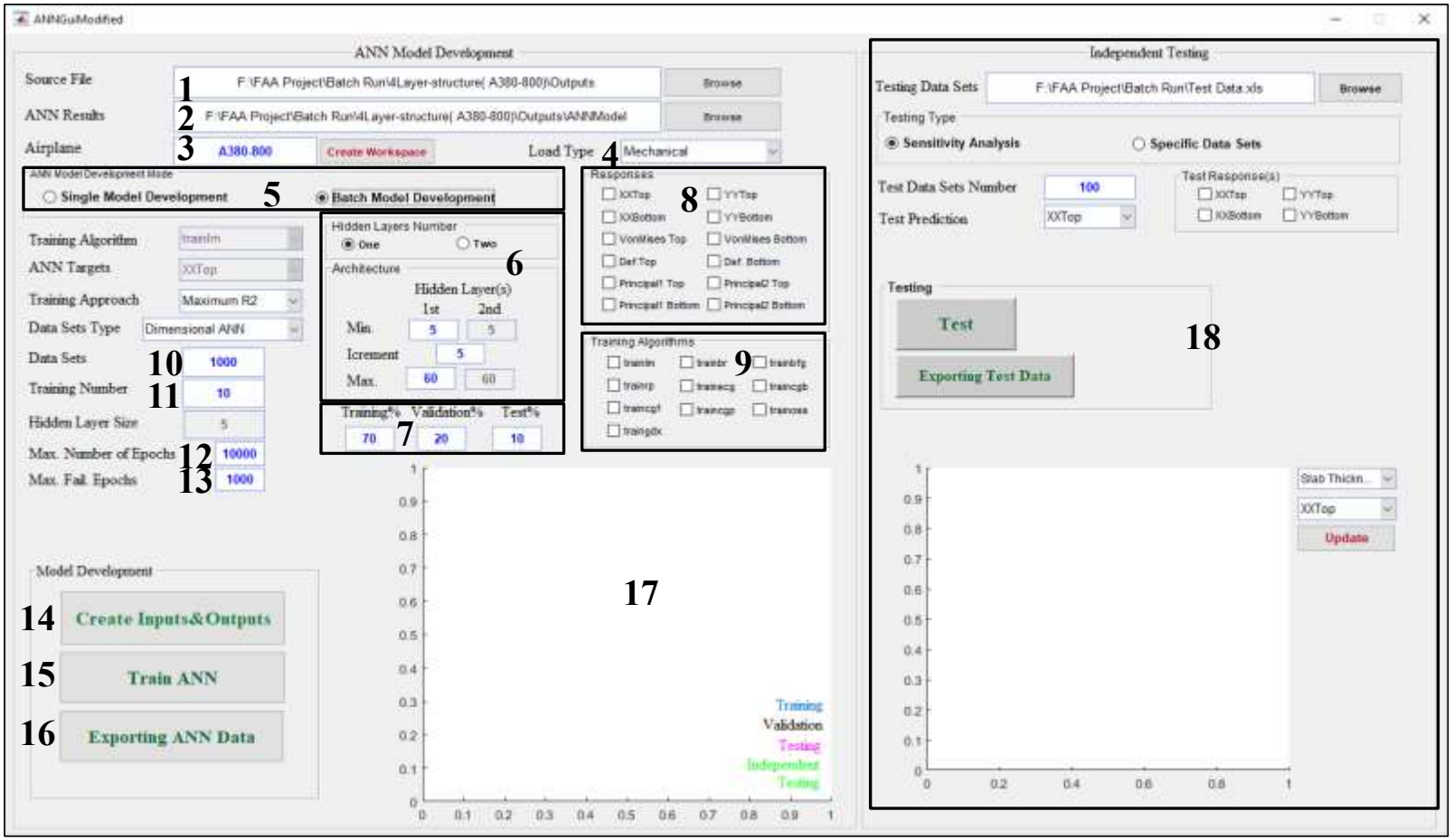

1. Data set spread sheets directory
2. ANN models saving file directory
3. Airplane type selection
4. Loading type selection
5. Single/Batch mode for developing ANN models
6. Model architecture determination
7. Data set dividing ratio
8. Critical responses selection
9. ANN training algorithms
10. Data set size
11. ANN model retraining number
12. Maximum number of epochs
13. Number of epochs for validation checks
14. Importing and dividing data set
15. Start ANN model development
16. Exporting ANN models spread sheet
17. ANN models regression plots
18. Test ANN models with new data sets

Figure 3.8 *ANN model development program.*

In this study three different conjugate gradient algorithms methods have been used for evaluating prediction accuracy improvement: Fletcher-Reeves Update (CGF), Polak-Ribiére Update (CGP), and Powell-Beale Restarts (CGB) [16], [17]. The various versions of conjugate gradient algorithms are distinguished by the method through which the ratio between the current and the previous gradient is computed in determining a new search direction [16].

The OSS method attempts to compromise between full quasi-Newton algorithms and conjugate gradient algorithms. It has the additional advantage that a new search direction can be calculated without computing a matrix inverse, and it requires slightly more storage and computation per training repetitions (epoch) than the conjugate gradient algorithms [16]. The LM algorithm is the fastest method for training, but it requires more storage than variable-learning-rate backpropagation and conjugate gradient algorithms.

Table 3.6 *Training algorithms used for developing ANN models.*

Acronym	**Algorithm**	**Description**
LM	trainlm	Levenberg-Marquardt
CGB	traincgb	Conjugate Gradient with Powell/Beale Restarts
OSS	trainoss	One Step Secant
CGF	traincgf	Fletcher-Powell Conjugate Gradient
CGP	traincgp	Polak-Ribiére Conjugate Gradient

Most practical neural networks have just two or three layers (one and two hidden layers and one output layer) [18]. To investigate which of two and three-layer networks work best for developing ANN model in this project, both architectures were tried for training ANN models and the best models were presented in this dissertation. Determination of an optimal number of neurons needed in a hidden layer is an active area of research that must be studied for each problem. While the global approach tends to require fewer neurons in the

hidden layer because each neuron contributes to the response over a large part of the input space, if the number of neurons is small, the network may not adequately fit the training data and result in under-fitting (Figure 3.9). Also, if more neurons, and therefore more parameters, are used, the network will have greater flexibility because using a network with more parameters to optimize creates a greater likelihood that the network will exhibit training data overfitting and fail to generalize well to new situations [18].

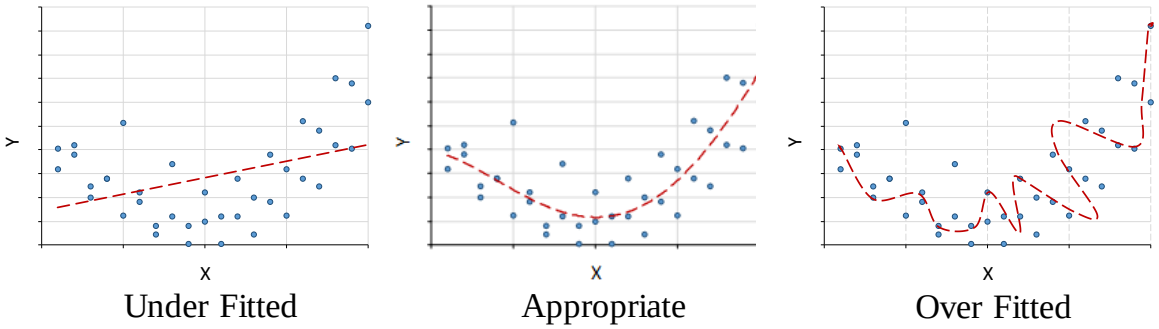

Figure 3.9 *Effect of flexibility of a model on prediction.*

As shown in Figure 3.8, the number of hidden layers and range of neurons in each layer can be defined in the ANN model development program. For determining the optimal number of neurons for evaluating prediction accuracy improvement, the networks were trained using between 5 and 50 neurons in a hidden layer. The architectures used for training ANN models for mechanical-loading-only cases are shown in Figure 3.10 and Figure 3.11. Figure 3.10 shows an architecture with one hidden layer with 17 predictors and one output layer, with the number of neurons (n) in the hidden layer varying from 5 to 50. Figure 3.11 shows an architecture with two hidden layers with 17 predictors and one output layer, with the number of neurons (n) in each hidden layer varying from 5 to 50. Figure 3.12 and Figure 3.13 illustrate the architectures used for training ANN models for simultaneous mechanical and temperature loading cases. Figure 3.12 shows an architecture with one hidden layer, 19 predictors, and one output layer, and the number of neurons (n) in the hidden layer varying

from 5 to 50. Figure 3.13 also displays an architecture with two hidden layers, 19 predictors and one output layer, and the number of neurons (n) in each hidden layer varying from 5 to 50.

Regularization and early stopping techniques are approaches that can be used for training neural networks to prevent overfitting and improve generalization. Although these two methods are very different, they both improve generalization by restricting network weights and thereby produce a network with fewer effective parameters. Early stopping restricts the network weights by stopping the training before the weights have converged to the minimum of the squared error. Regularization restricts the weights by adding a term to the squared error that penalizes large weights [18]. In this study the early stopping technique was used since this technique is automatically provided for all of the supervised network creation functions in MATLAB, including the backpropagation network creation functions [18].

The idea behind early stopping method is that, as training progresses, the complexity of the resulting network is increased. If training is stopped before the minimum of the error surface reached, the network will effectively be using fewer parameters and be less likely to over-fit [18]. As shown in Figure 3.8, a maximum number of epochs for training (i.e. 10,000) and a maximum number of allowable iterations for validation check (i.e. 1,000) have been provided in the program's GUI in order to apply early stopping. The maximum number of allowable iterations for validation check is used to stop training if the error on the validation set has failed to improve.

For developing ANNs using MATLAB, the available data is divided into three parts: a training set, a validation set, and a testing set. The training set is used to compute gradients

or Jacobians and to determine the weight update at each iteration. The validation set is an indicator of what is happening to the network function “in between” the training points, and its error is monitored during the training process. When the error on the validation set goes up over several iterations, the training is stopped, and the weights that produced the minimum error on the validation set are used as the final trained network weights [18].

The program requires the user to set the number of restarts for model retraining. This step is part of the training process to ensure that the training process does not fall into a local minimum. A single training run may not produce optimal performance because of local minimum on the performance surface, so it is best to restart the training at several different initial conditions and select the network that produces the best performance. Five to ten restarts will almost always produce a global optimum [19]. In this study 10 different initial conditions have been considered for each ANN model architecture.

All trained ANN models are stored in the workspace created at the step 1. In the next step, the stored models are evaluated to find the optimal model.

Export Optimum ANN Model

The program computes several measures of accuracy prediction (MSE, RMSE, R^2 and AAE), which are started in the workspace along with the trained ANNs. The optimal model is defined as the model with the lowest RMSE among those considered. In step three the optimum model results, the targets and predictions, and all prediction accuracy measures, are exported to a spreadsheet.

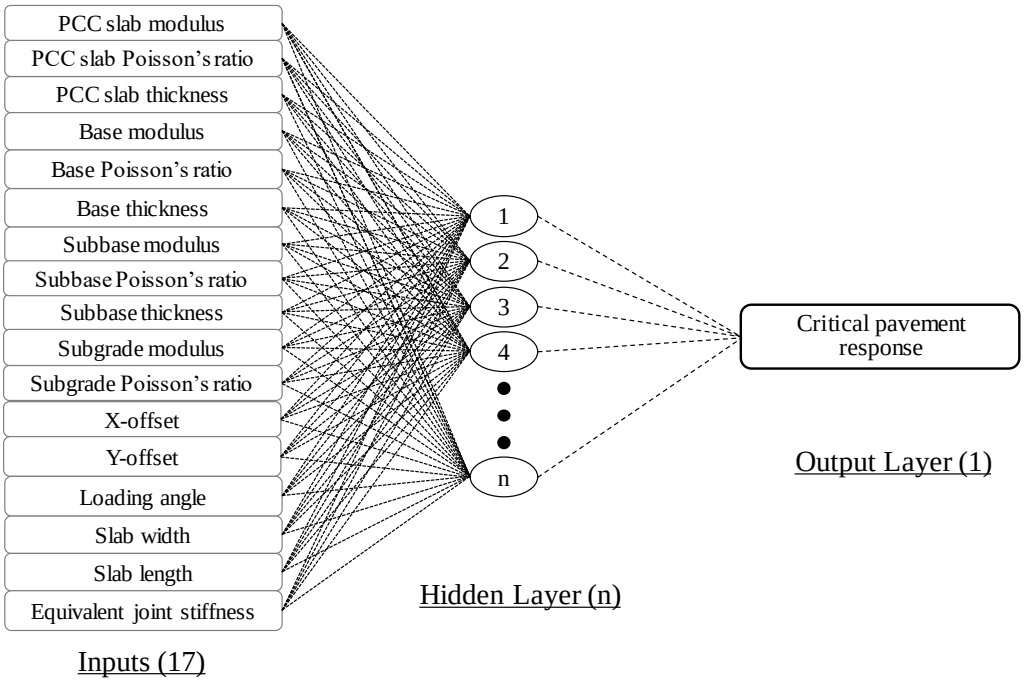

Figure 3.10 *Two-layer ANN model architecture for mechanical loading only cases.*

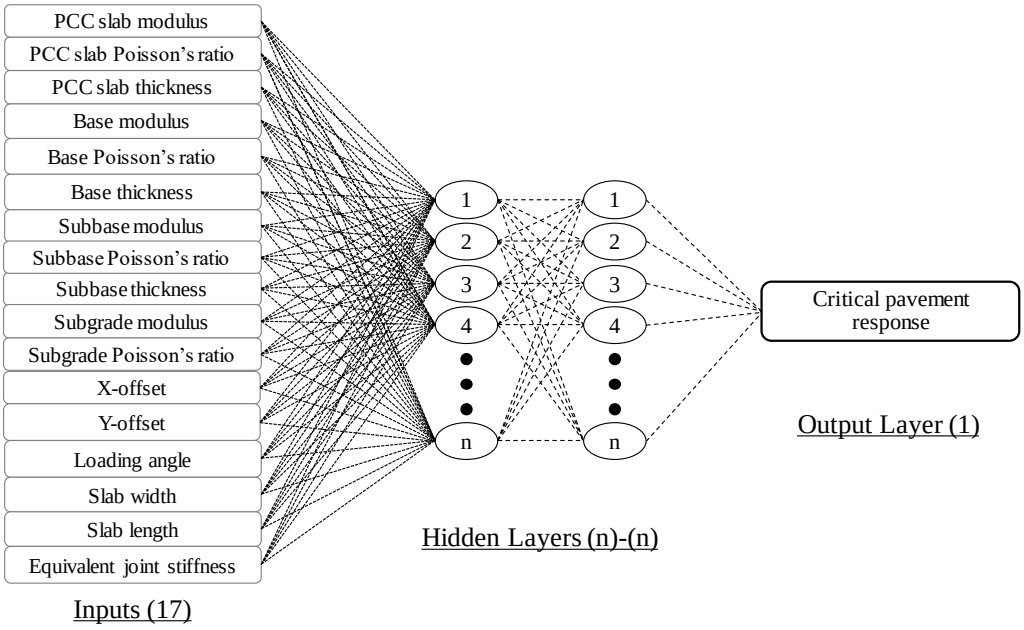

Figure 3.11 *Three-layer ANN model architecture for mechanical loading only cases.*

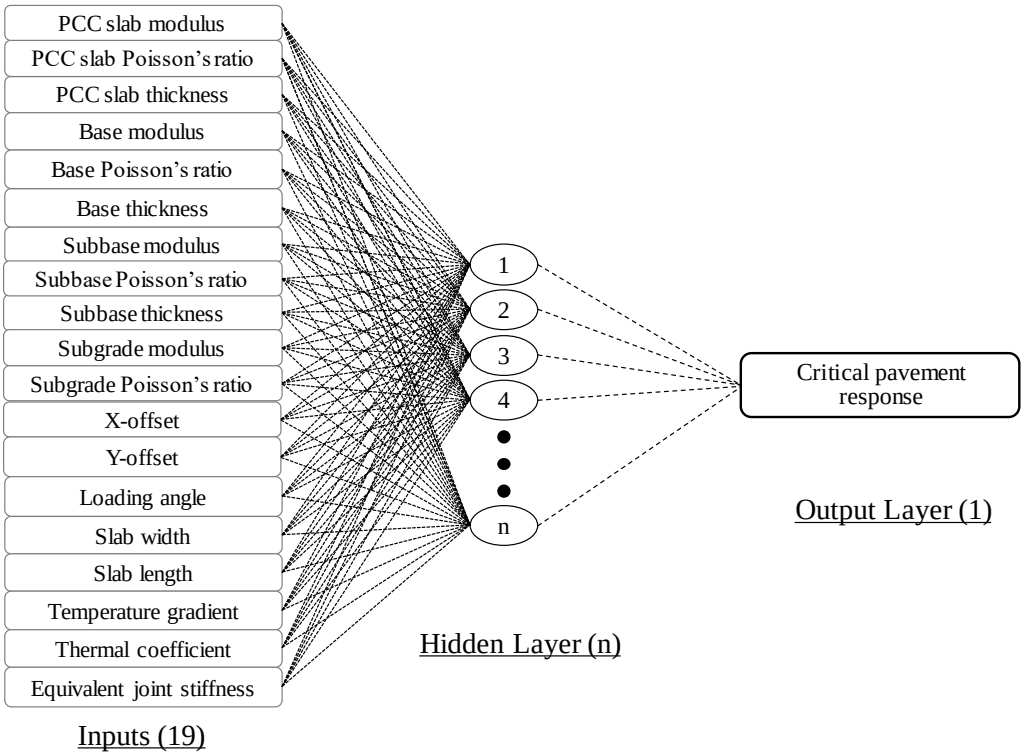

Figure 3.12 *Two-layer ANN model architecture for simultaneous temperature and mechanical loading cases.*

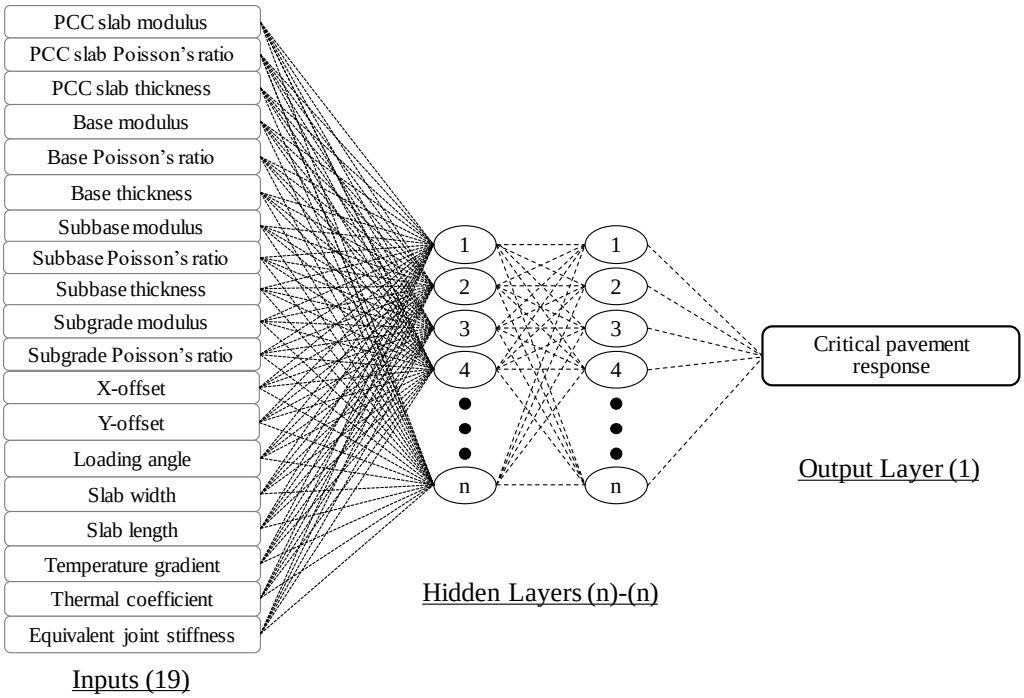

Figure 3.13 *Three-layer ANN model architecture for simultaneous temperature and mechanical loading cases.*

ANNFAA: FAA ANN Rigid Pavement Analysis Tool

The project team developed new artificial neural network-based analysis program (ANNFAA) to replicate maximum stress responses on top and bottom of slabs in rigid airfield pavements. This program is based on the ANN models trained in the last section. Figure 3.15 shows the user interface. Working with the program is similar to using FEAFAA, although in the new program creating a mesh and running NIKE3D are not required. The same inputs as in FEAFAA are defined for ANNFAA (Figure 3.15 (a)), and a set of inputs can be imported into ANNFAA. Results are predicted for all input sets at once. ANNFAA uses weights and biases matrices exported from the neural networks trained in MATLAB. Equation (1) shows the calculation used within the program for predicting the critical stresses. Weight matrices (**IW** and **LW**) and biases ($\mathbf{B_1}$ and $\mathbf{B_2}$) are obtained from the optimal ANN models for each aircraft. Equation (1) is used by ANNFAA if the optimum ANN model for the aircraft and response of interest has one hidden layer, while if the model has two hidden layers Equation (2) is used.

$$Y = \mathbf{B_2} + \mathbf{LW_1} \times tansig\,(\mathbf{B_1} + \mathbf{IW} \times \mathbf{Inputsnor}) \quad (1)$$

$$Y = \mathbf{B_3} + \mathbf{LW_2} \times tansig\,((\mathbf{LW_1} \times tansig(\mathbf{B_1} + \mathbf{IW} \times \mathbf{Inputsnor})) + \mathbf{B_2}) \quad (2)$$

Where:

$\mathbf{B_1}$, $\mathbf{B_2}$, and $\mathbf{B_3}$ = Biases matrices

$\mathbf{LW_1}$ = Weight matrix (layer 1)

$\mathbf{LW_2}$ = Weight matrix (layer 2)

IW = Input weight matrix

tansig = Hyperbolic tangent sigmoid transfer function (see Figure 3.14)

Inputsnor = Matrix of normalized inputs between (-1, 1)

Y = Network output of interest

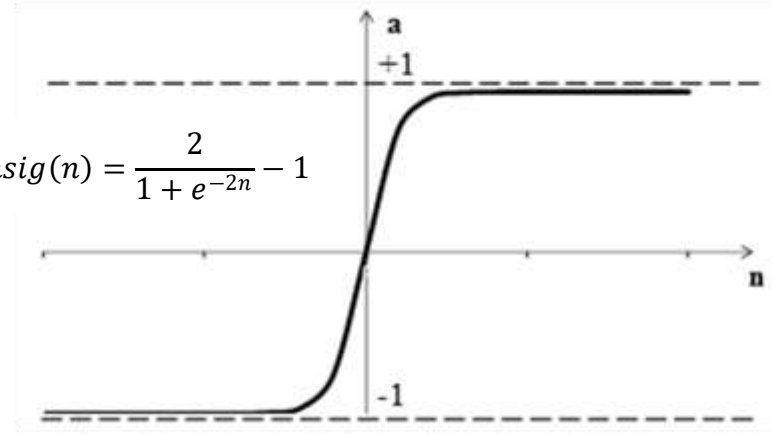

Figure 3.14 *Hyperbolic tangent sigmoid transfer function.*

Inputsnor includes the normalized inputs value obtained by Equation (3):

$$\text{Normalized } X_i = 2\times \frac{(X_i - X^i_{min})}{(X^i_{max} - X^i_{min})} - 1 \qquad (3)$$

Where Xi is the actual value of the input i, X^i_{min} is the minimum of the input i in the dataset, and X^i_{max} is the maximum of the input i in the dataset. The matrix size of **IW** ($S_1 \times R$) is determined by number of elements R in the **Inputsnor** and the number of neurons in the first hidden layer (S_1), and the size of the weight matrices is determined by the number of neurons in each layer (S_1 and S_2). For a one-hidden-layer ANN architecture the $\mathbf{LW_1}$ size is $1\times S_1$, while for a two-hidden-layer architecture the size of $\mathbf{LW_1}$ is $S_1\times S_2$ and $\mathbf{LW_2}$ is $1\times S_2$. The bias matrix size for $\mathbf{B_1}$ is S×1 and for $\mathbf{B_2}$ is 1×1 for one hidden layer. For an architecture with two hidden layers the sizes of $\mathbf{B_1}$ and $\mathbf{B_2}$ are $S_1\times 1$ and $S_2\times 1$, respectively, and $\mathbf{B_3}$ is 1×1 in this study.

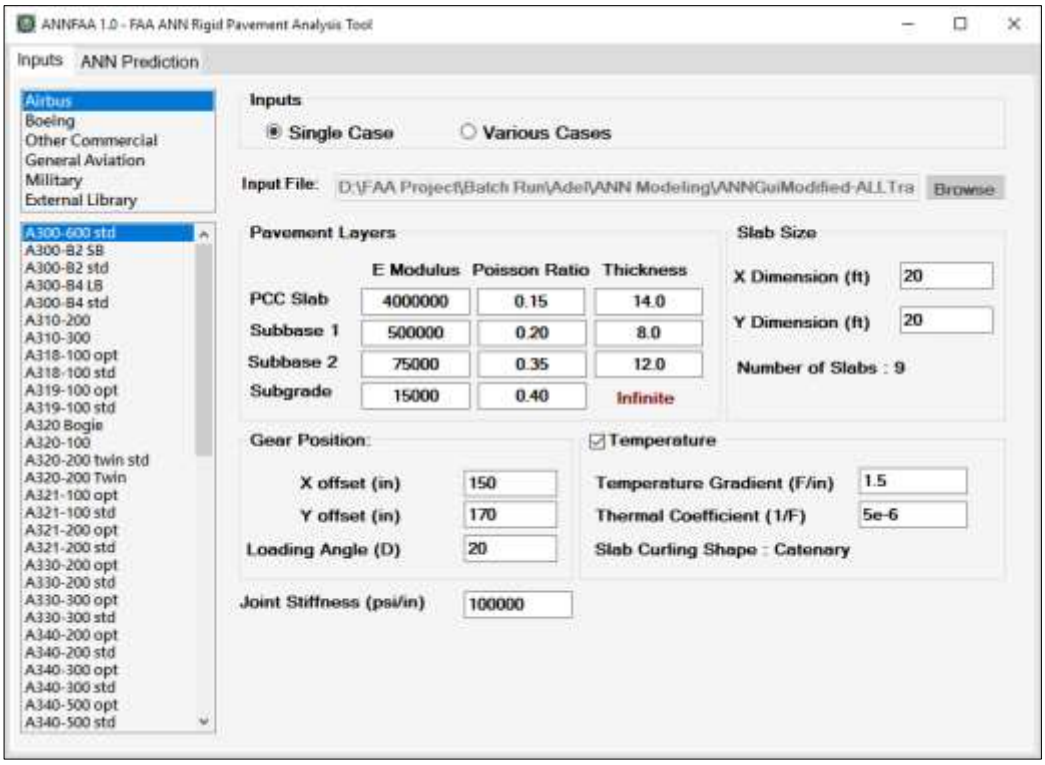

(a)

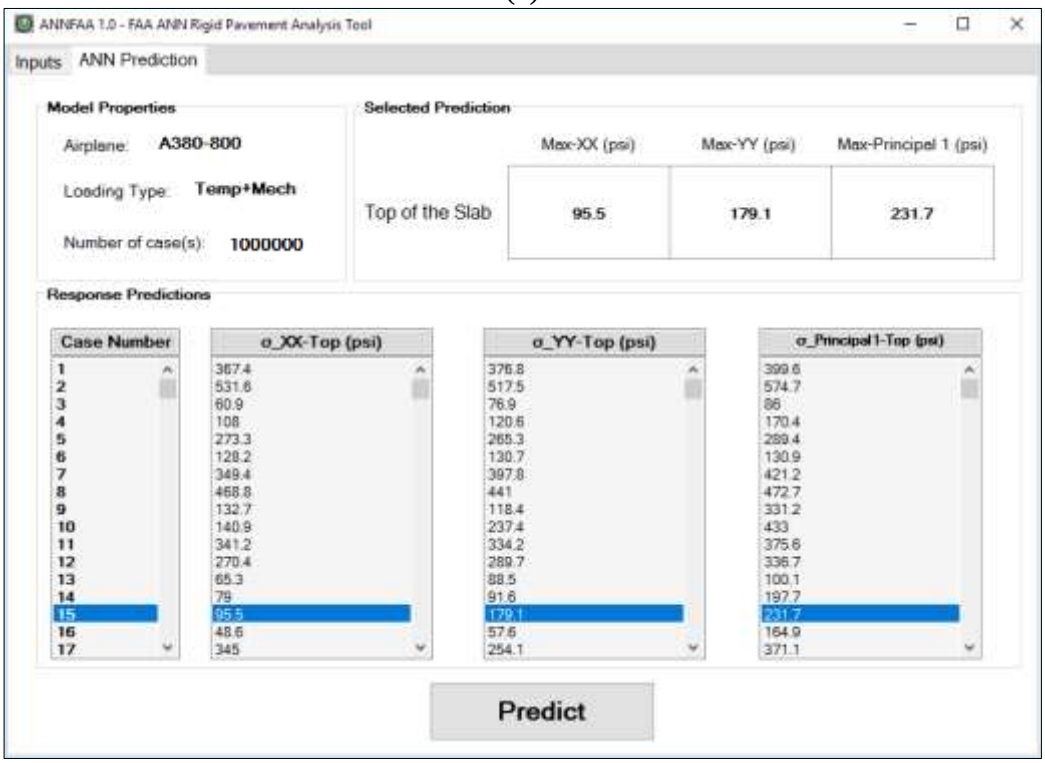

(b)

Figure 3.15 *ANNFAA user interface. (a) Input and (b) Prediction tabs.*

Table 3.7 shows the execution time for ANNFAA to predict one critical response. As shown in the table, for 1 million cases, it takes 18.8 seconds to obtain the inputs, weights, and bias matrices from text files, and 6.3 seconds to compute the critical responses ($\sigma_{XX\text{-}Max\text{-}Top\text{-}Tens.}$, $\sigma_{YY\text{-}Max\text{-}Top\text{-}Tens.}$, or $\sigma_{1\text{-}Max\text{-}Top\text{-}Tens.}$) for all cases of a one-hidden-layer ANN model, while the same process for a two-hidden-layer ANN model takes 18.4 and 15.9 seconds, respectively, to import data and compute the critical responses.

In the ANNFAA program the matrix multiplication is performed in parallel so the full processor capacity is utilized. Such parallel computation significantly increases program execution speed and decreases run time to less than one-third that of a non-parallel program execution.

Table 3.7 *ANNFAA computation run times for different data set sizes.*

Data set size (Cases)	**Run Time (Second)**			
	One Hidden Layer		**Two Hidden Layers**	
	Importing inputs, weights and biases matrices	**Prediction computation**	**Importing inputs, weights and biases matrices**	**Prediction computation**
5,000	0.08	0.10	0.38	0.15
500,000	9.43	3.43	9.36	7.71
1,000,000	18.84	6.33	18.37	15.89

Summary and Conclusions

The main objective of this chart was to create a process for developing and using critical stress response prediction models for multiple slab-rigid airfield pavements and also to generate software for rapid analysis of the rigid pavements. A batch run automation tool for implementing 3D-finite element (3D-FE) simulation and post-processing the outputs has been created. An extensive database of input-output records from NIKE3D-FAA FE analysis

have been obtained for each aircraft and for each loading condition. Moreover, an ANN model-development tool was created in MATLAB to facilitate the process of ANN model development and enhance the speed of importing data, training models, and exporting and determining the optimum models. Furthermore, a new tool, ANN based FAA rigid pavement analysis tool (ANNFAA), has been developed using C# programming to replicate maximum stress responses at slab tops of rigid airfield pavements for all types of aircraft provided by Finite Element Analysis FAA (FEAFAA) version 2.0 software that makes use of NIKE3D_FAA as a stand-alone tool for 3D-FE analysis of multiple-slab rigid airport pavements and overlays. The major conclusions of this study are:

- The optimum mesh size for both slab and foundation was 30 elements in each direction.
- An automation program was developed in order to perform FEAFAA, save input files, run NIKE3D, and save the output files for each case, automatically. It also facilitated and handled creation of a synthetic database consisting of FEAFAA input parameters and associated critical pavement responses.
- The program provided a very easy-to-use platform for post-processing the data and gathering all the data required for further ANN development.
- Use of the automation program significantly increased the efficiency of the batch run execution by decreasing the number of mistakes and time required for performing the finite-element analysis for 156 different types of airplanes.
- The MATLAB ANN model development tool supported development of a total of 6,000 ANN models for mechanical and simultaneous mechanical and temperature loading conditions for each type of aircraft.

- The rapid rigid airfield pavement analysis tool ANNFAA can predict critical tensile stresses for 1 million cases in 6 to 16 seconds, while executing the same cases by NIKE3D-FAA would take several weeks.
- Transforming all the ANN model data from MATLAB workspaces into text files and making them ready to for use in an executive program like ANNFAA is a very useful, fast, and easy method for utilizing the developed ANN models for all aircraft.
- The ANNFAA tool can be used as a tool for testing ANN models during further investigation and model development.
- Critical response surrogate models are very useful alternatives for use in design iterative processes, making routine design more efficient and practical while taking into account more failure modes during design.
- Since the models developed in this study are for rigid pavements consisting of nine multiple slabs, the critical responses of the pavement systems with some other number of slabs might not be correctly predicted by the models presented in this study.

References

[1] H. Ceylan, E. Tutumluer, and E. Barenberg, "Artificial Neural Networks for Analyzing Concrete Airfield Pavements Serving the Boeing B-777 Aircraft," Transp. Res. Rec. J. Transp. Res. Board, vol. 1684, no. 99, pp. 110–117, 1999.

[2] H. Ceylan, "Analysis and design of concrete pavement systems using artificial neural networks," University of Illinois at Urbana-Champaign, 2002.

[3] H. Ceylan and K. Gopalakrishnan, "Neural Networks Based Models for Mechanistic-Empirical Design of Rubblized Concrete Pavements," Geotech. Spec. Publ. No. 169, Soil Mater. Inputs Mech. Pavement Des. ASCE, pp. 1–10, 2007.

[4] O. Elbagalati, M. A. Elseifi, K. Gaspard, and Z. Zhang, "Development of an artificial neural network model to predict subgrade resilient modulus from continuous deflection testing," Can. J. Civ. Eng., vol. 44, no. 9, pp. 700–706, 2017.

[5] H. Ceylan, S. Kim, K. Gopalakrishnan, C. W. Schwartz, and R. Li, "Sensitivity quantification of jointed plain concrete pavement mechanistic-empirical performance predictions," Constr. Build. Mater., vol. 43, pp. 545–556, 2013.

[6] O. Kaya, A. Rezaei-Tarahomi, H. Ceylan, K. Gopalakrishnan, S. Kim, and D. R. Brill, "Neural Network--Based Multiple-Slab Response Models for Top-Down Cracking Mode in Airfield Pavement Design," J. Transp. Eng. Part B Pavements, vol. 144, no. 2, p. 4018009, 2018.

[7] A. Rezaei-Tarahomi, O. Kaya, H. Ceylan, K. Gopalakrishnan, S. Kim, and D. R. Brill, "Neural networks prediction of Critical Responses Related to Top-Down and Bottom-Up Cracking in Airfield Concrete Pavement," in 10th International Conference on the Bearing Capacity of Roads, Railways and Airfields, 2017.

[8] A. R. Ghanizadeh and M. R. Ahadi, "Application of Artificial Neural Networks for Analysis of Flexible Pavements under Static Loading of Standard Axle," vol. 3, no. 1, 2016.

[9] H. Ceylan, M. B. Bayrak, and K. Gopalakrishnan, "Neural networks applications in pavement engineering: A recent survey," Int. J. Pavement Res. Technol., vol. 7, no. 6, pp. 434–444, 2014.

[10] K. Gopalakrishnan, H. Ceylan, and N. O. Attoh-Okine, Intelligent and soft computing in infrastructure systems engineering: recent advances, vol. 259. Springer, 2009.

[11] D. R. Brill, "Development of advanced computational models for airport pavement design," Rep. No. DOT/FAA/AR-97, vol. 47, 1998.

[12] D. R. Brill, "Field verification of a 3D finite element rigid airport pavement model," 2000.

[13] A. Rezaei-Tarahomi, O. Kaya, H. Ceylan, S. Kim, and D. R. Brill, "Neural Network Algorithms for Rigid Airfield Pavement Responses," in Advances in Materials and Pavement Performance Prediction, Doha, Qatar, 2018.

[14] "AutoItV3." Jonathan Bennett & AutoIt Team, 2018.

[15] "Tecplot 360 EX 2016 R2." Tecplot, Inc, 2016.

[16] H. Demuth and M. Beale, Neural Network Toolbox. 2002.

[17] K. Gopalakrishnan, "Effect of training algorithms on neural networks aided pavement diagnosis," Int. J. Eng. Sci. Technol., vol. 2, no. 2, pp. 83–92, 2010.

[18] M. T. Hagan, H. B. Demuth, M. H. Beale, and O. De Jesús, Neural Network Design. Boston:PWS Pub, 2014.

[19] L. Hamm, B. W. Brorsen, and M. T. Hagan, "Comparison of stochastic global optimization methods to estimate neural network weights," Neural Process. Lett., vol. 26, no. 3, pp. 145–158, 2007.

CHAPTER 4. ANN MODEL ACCURACY ASSESSMENTS

Abstract

To consider top-down cracking failure in current airport rigid pavement design practices, a multiple-slab pavement structure's three-dimensional finite element (3D FE) model should be analyzed for determining critical responses associated with such failures, and artificial neural networks (ANNs) can be considered a robust and computationally efficient alternative for 3D FE analysis. This study compares the effects of airport rigid pavement's most important properties on the critical tensile stresses predicted by the ANN models relative to those for 3D-FE solutions. Sensitivity evaluation of both the 3D-FE solutions and the ANN model predictions for two new large and heavy aircraft (B777-300 ER and B787-8) have been conducted and are discussed in this study. The normalized sensitivity index (NSI) has been utilized to quantify the levels of sensitivity of the critical tensile stresses to changes in PCC slab thickness, base layer thickness, PCC slab modulus, subgrade elastic modulus, temperature gradients, and thermal coefficient. The results demonstrate that the developed ANN model is able to determine top-down critical tensile stress sensitivity similarly to the 3D-FE model.

Introduction

As a follow-up to ANN response model development, this study was conducted to validate the developed ANN models using sensitivity analysis, by both NIKE3D-FAA solutions and those predicted by ANN models, of the critical tensile stresses on top of rigid airfield pavements. Moreover this validation approach helped improving the models and using the most accurate ones in developing ANN based analyzing program called ANNFAA [1]. Sensitivity analysis results of the ANN critical response prediction models developed for

the B777-300 ER and the B787-8 are discussed in this chapter. To present sensitivity of the critical tensile stresses, the normalized sensitivity index (NSI) was obtained, for both NIKE3D-FAA solutions and the ANN response model predictions, for six input variables: PCC slab thickness, base layer thickness, PCC slab modulus, subgrade elastic modulus, temperature gradient and thermal coefficient. These variables have been selected since they have been obtained as the most effective inputs for the NIKE3D-FAA computed critical stresses on top of the slab [2], [3].

This chapter presents ANN response model performance results for different aircraft and compared them with NIKE3D-FAA FE solutions. The accuracy and robustness of the models are also discussed. Results for the ANN response models predicting critical tensile stresses at top of the slab most associated with top-down cracking are also demonstrated in this section.

Accuracy Assessment Criteria

There is no consensus on the most appropriate measure for representing model errors. AAE, maximum absolute error (MAE), R^2, and RMSE are the standard statistical metrics used to measure model performance and their accuracy in this study. These are useful measures widely used as important criteria in model evaluations and assessments. Since any individual metric tends emphasize only one aspect of a model's performance, a combination of different assessment criteria is usually required to assess model performance and accuracy adequately.

The coefficient of determination is a relative measure of fit, while RMSE is an absolute measure of fit [4]. The coefficient of determination is the most commonly used metric used to understand the percentage of variance in the target response explained by model prediction. Also, quantifying the error using the same measuring unit as that of the

responses are often needed. The RMSE, AAE, and MAE values all use the same units (psi) as the model prediction outputs) in this study. Among these measures, RMSE avoids the use of absolute value, making it distinct from AAE. RMSE indicates how accurately the model predicts the response, and it is the most important criterion for fit if the main purpose of the model is prediction [4]. The greatest concern with use of RMSE is its sensitivity to outliers, meaning that it tends to be more affected by large residuals. Absolute average error and maximum absolute error are the criteria that are most robust with respect to such big residuals. Equations 4.1-4.5 are the formulas for calculating the metrics for model performance and accuracy evaluation.

$$MSE = \frac{1}{n} \times \sum_{j=1}^{n} (y_j^{prediction} - y_j^{solution})^2 \tag{4.1}$$

$$RMSE = \sqrt{MSE} \tag{4.2}$$

$$R^2 = 1 - \frac{\sum_{j=1}^{n} \left(y_j^{solution} - y_j^{prediction}\right)^2}{\sum_{j=1}^{n} \left(y_j^{solution} - \bar{y}^{solution}\right)^2} \tag{4.3}$$

$$AAE = \frac{1}{n} \times \sum_{j=1}^{n} \left| y_j^{prediction} - y_j^{solution} \right| \tag{4.4}$$

$$MAE = Max\left(\left| y_j^{prediction} - y_j^{solution} \right|\right) \tag{4.5}$$

Where:

n = Element number within a dataset

j = Case number in the data set

$y^{solution}$ = FEAFAA output critical pavement responses

$y^{prediction}$ = ANN models predicted critical pavement responses

Since the RMSE is very popular for ANN model performance assessment [5]–[8], the RMSE obtained from independent testing was used to determine the optimal model among all the models trained by different algorithms and architectures.

ANN models' performance accuracy

This chapter reports the most accurate ANN response model for each aircraft, including critical responses. Independent testing results for the ANN models developed for all Airbus and Boeing airplanes are presented in Table 4.1. Also, detailed illustrations of each ANN model accuracy are presented by charts for four types of new large and heavy aircraft (B777-300 ER, B747-8, A380-800, and A340-500 opt). Each chart describes the accuracy of the ANN models for training, testing, validation, and independent testing datasets.

Table 4.1 shows the training algorithm and architecture of the most accurate ANN model for each critical response by each type of aircraft under both mechanical-only and simultaneous mechanical and temperature-induced loadings. This table shows the independent testing accuracy measures of the ANN models, using criteria of absolute average error (AAE), maximum absolute error (MAE), root-mean-squared error (RMSE), and R^2. For instance, Table 4.1 shows that most accurate model for predicting $\sigma_{XX\text{-}Max\text{-}Top\text{-}Tens.}$ for B777-300 ER mechanical loading, is an ANN model with 17-15-1 architecture (17 inputs, one hidden layer with 15 neurons, and one output) and OSS training algorithm. The ANN model provides high accuracy for an independent dataset, with an R^2 of 0.947 under mechanical-loading conditions. For the combined loading condition, the ANN model with 19-5-5-1 architecture (19 inputs, two hidden layers with five neurons in each layer, and one output) and a CGF training algorithm was the most accurate model, with R^2 accuracy of 0.925 for independent testing.

Generally, for most dual-wheel aircraft, the R^2 values of ANN models are between 0.7 and 0.9 and for some of them, accuracy of principal stress prediction models is less than accuracy of axial stresses (in *x* and *y* directions) prediction models. The ANN models trained for the heavy aircraft show more accurate results compared to the models trained for dual-wheel and light aircraft. For majority of aircraft, the ANN model architecture of 19-5-5-1 was obtained as the optimum model for simultaneous temperature and mechanical loading condition. Conjugate gradient algorithms (CGB, CGF, and CGP) were obtained as the optimum algorithms for most of the aircraft's ANN models.

Table 4.1 *ANN models' independent testing results for critical top tensile stresses.*

Aircraft	**Accuracy Criteria**	**Top Tensile Stresses**					
		Mechanical Loading			**Simultaneous Temperature and Mechanical Loading**		
		$\sigma_{XX\text{-}Max}$ [1]	$\sigma_{YY\text{-}Max}$ [2]	$\sigma_{1\text{-}Max}$ [3]	$\sigma_{XX\text{-}Max}$ [1]	$\sigma_{YY\text{-}Max}$ [2]	$\sigma_{1\text{-}Max}$ [3]
A300-B2 SB	Alg. [4]	CGP	CGP	OSS	CGF	OSS	OSS
	Arch. [5]	17-10-10-1	17-30-1	17-10-10-1	19-5-5-1	19-5-5-1	19-5-5-1
	AAE [*]	4.1	3.8	4.0	19.3	19.9	19.9
	MAE [*]	27.9	18.8	26.2	89.5	108.0	101.1
	RMSE [*]	5.8	5.1	5.9	26.6	27.6	28.1
	R^2	0.912	0.931	0.934	0.944	0.935	0.950
A300-B2 std	Alg. [4]	CGP	CGF	CGB	CGF	CGB	CGP
	Arch. [5]	17-10-1	17-10-1	17-20-1	19-5-1	19-5-1	19-5-5-1
	AAE [*]	4.4	4.0	4.5	20.6	19.6	19.0
	MAE [*]	26.6	21.6	24.3	83.8	112.5	99.1
	RMSE [*]	6.0	5.4	6.2	26.6	26.0	27.4
	R^2	0.907	0.920	0.908	0.937	0.937	0.957
A300-B4 LB	Alg. [4]	CGP	CGB	CGB	CGB	OSS	OSS
	Arch. [5]	17-15-1	17-10-1	17-10-1	19-5-5-1	19-10-1	19-5-5-1
	AAE [*]	4.7	4.6	4.4	20.4	18.8	20.9
	MAE [*]	26.5	32.3	33.6	93.1	128.6	132.4
	RMSE [*]	6.6	6.7	6.5	26.9	26.5	30.4
	R^2	0.929	0.919	0.937	0.941	0.942	0.944
A300-B4 std	Alg. [4]	OSS	CGP	OSS	CGB	CGB	CGB
	Arch. [5]	17-10-10-1	17-15-1	17-10-10-1	19-5-1	19-5-5-1	19-5-5-1
	AAE [*]	4.9	4.8	5.1	23.4	22.7	21.5
	MAE [*]	40.9	27.5	32.8	99.1	107.1	123.1
	RMSE [*]	7.0	6.4	7.1	30.0	29.3	30.8
	R^2	0.930	0.940	0.931	0.924	0.928	0.946

Note: [1] $\sigma_{XX\text{-}Max\text{-}Top\text{-}Tens.}$, [2] $\sigma_{YY\text{-}Max\text{-}Top\text{-}Tens.}$, [3] $\sigma_{1\text{-}Max\text{-}Top\text{-}Tens.}$, [4] Training Algorithm, [5] ANN Model Architecture, [*] The unit is (psi)

Table 4.1 (Continued)

Aircraft	Accuracy Criteria	Top Tensile Stresses					
		Mechanical Loading			Simultaneous Temperature and Mechanical Loading		
		$\sigma_{XX\text{-}Max}$ [1]	$\sigma_{YY\text{-}Max}$ [2]	$\sigma_{1\text{-}Max}$ [3]	$\sigma_{XX\text{-}Max}$ [1]	$\sigma_{YY\text{-}Max}$ [2]	$\sigma_{1\text{-}Max}$ [3]
A300-600 std	Alg. [4]	CGB	LM	CGF	OSS	CGB	OSS
	Arch. [5]	17-25-1	17-10-10-1	17-45-1	19-5-5-1	19-5-5-1	19-5-5-1
	AAE [*]	6.1	5.0	4.9	19.0	19.5	22.2
	MAE [*]	36.2	28.3	27.0	99.9	96.5	111.0
	RMSE [*]	8.3	6.7	7.0	25.6	26.6	32.5
	R^2	0.893	0.922	0.926	0.955	0.952	0.933
A300-600 LB	Alg. [4]	OSS	CGB	CGF	CGB	LM	OSS
	Arch. [5]	17-10-10-1	17-35-1	17-45-1	19-5-5-1	19-5-5-1	19-5-5-1
	AAE [*]	5.7	5.2	5.1	19.6	21.1	21.2
	MAE [*]	27.3	24.0	37.3	96.3	127.0	153.5
	RMSE [*]	7.8	6.8	7.4	26.9	30.5	29.7
	R^2	0.897	0.913	0.911	0.945	0.931	0.944
A310-200	Alg. [4]	CGP	CGF	CGP	OSS	OSS	CGF
	Arch. [5]	17-10-1	17-10-1	17-10-1	19-5-5-1	19-5-5-1	19-5-5-1
	AAE [*]	4.1	4.0	4.3	18.7	18.8	18.5
	MAE [*]	50.2	21.9	33.7	118.2	94.2	98.9
	RMSE [*]	6.6	5.2	6.3	26.1	25.8	26.4
	R^2	0.916	0.945	0.921	0.943	0.944	0.948
A310-300	Alg. [4]	OSS	CGP	OSS	CGP	OSS	LM
	Arch. [5]	17-10-1	17-10-1	17-5-5-1	19-5-5-1	19-5-5-1	19-5-5-1
	AAE [*]	4.3	4.1	4.4	18.6	19.1	20.8
	MAE [*]	20.7	20.5	28.9	98.9	104.7	92.5
	RMSE [*]	5.8	5.4	6.4	25.4	26.6	28.2
	R^2	0.913	0.920	0.902	0.942	0.936	0.952
A318-100 std	Alg. [4]	OSS	CGF	CGB	CGF	OSS	CGP
	Arch. [5]	17-5-5-1	17-15-1	17-25-1	19-5-5-1	19-5-5-1	19-5-5-1
	AAE [*]	2.3	2.6	3.8	17.9	17.1	20.0
	MAE [*]	26.0	14.9	41.8	105.6	91.7	146.6
	RMSE [*]	3.6	3.5	6.2	25.6	23.9	27.6
	R^2	0.892	0.894	0.845	0.943	0.950	0.936
A318-100 opt	Alg. [4]	CGB	CGP	CGB	OSS	CGP	CGB
	Arch. [5]	17-10-10-1	17-10-1	17-15-1	19-5-5-1	19-5-5-1	19-5-5-1
	AAE [*]	3.0	3.2	4.6	17.3	17.4	20.0
	MAE [*]	27.5	16.0	25.3	129.1	138.7	109.1
	RMSE [*]	4.5	4.4	6.2	24.0	24.8	27.5
	R^2	0.898	0.901	0.843	0.955	0.953	0.950
A319-100 opt	Alg. [4]	CGP	CGF	CGB	CGB	CGF	CGF
	Arch. [5]	17-10-1	17-20-1	17-15-1	19-5-5-1	19-5-5-1	19-5-5-1
	AAE [*]	2.9	3.6	4.3	19.3	21.0	20.6
	MAE [*]	26.3	33.8	26.2	111.8	91.0	133.3
	RMSE [*]	4.1	5.2	6.3	27.2	27.8	28.6
	R^2	0.938	0.903	0.837	0.925	0.921	0.936

Note: [1] $\sigma_{XX\text{-}Max\text{-}Top\text{-}Tens.}$, [2] $\sigma_{YY\text{-}Max\text{-}Top\text{-}Tens.}$, [3] $\sigma_{1\text{-}Max\text{-}Top\text{-}Tens.}$, [4] Training Algorithm, [5] ANN Model Architecture, [*] The unit is (psi)

Table 4.1 (Continued)

Aircraft	Accuracy Criteria	Top Tensile Stresses					
		Mechanical Loading			Simultaneous Temperature and Mechanical Loading		
		$\sigma_{XX\text{-}Max}$ [1]	$\sigma_{YY\text{-}Max}$ [2]	$\sigma_{1\text{-}Max}$ [3]	$\sigma_{XX\text{-}Max}$ [1]	$\sigma_{YY\text{-}Max}$ [2]	$\sigma_{1\text{-}Max}$ [3]
A319-100 std	Alg. [4]	LM	CGP	CGP	CGF	CGP	LM
	Arch. [5]	17-10-10-1	17-10-1	17-15-1	19-10-10-1	19-5-5-1	19-5-5-1
	AAE [*]	2.8	2.8	3.8	19.6	16.9	19.6
	MAE [*]	14.8	14.9	25.8	110.5	115.6	111.5
	RMSE [*]	3.9	3.9	5.3	27.4	25.8	28.4
	R^2	0.915	0.907	0.847	0.932	0.939	0.941
A320 Bogie	Alg. [4]	CGF	LM	CGB	CGF	CGF	OSS
	Arch. [5]	17-10-10-1	17-10-1	17-20-1	19-5-5-1	19-5-5-1	19-5-5-1
	AAE [*]	2.3	2.3	2.9	20.6	20.6	18.3
	MAE [*]	17.1	15.5	22.1	107.1	126.5	101.2
	RMSE [*]	3.3	3.2	4.1	29.5	29.6	24.6
	R^2	0.953	0.949	0.907	0.928	0.923	0.954
A320-100	Alg. [4]	OSS	LM	CGP	OSS	CGP	CGP
	Arch. [5]	17-10-1	17-15-1	17-20-1	19-5-5-1	19-5-5-1	19-10-1
	AAE [*]	2.9	3.4	4.6	20.2	20.3	20.9
	MAE [*]	29.8	36.7	45.0	120.7	125.2	104.9
	RMSE [*]	4.3	5.0	7.3	30.0	31.1	28.2
	R^2	0.926	0.897	0.799	0.920	0.911	0.942
A320-200 Twin std	Alg. [4]	CGP	CGB	OSS	LM	CGF	CGB
	Arch. [5]	17-10-10-1	17-10-1	17-10-1	19-10-1	19-5-5-1	19-5-5-1
	AAE [*]	3.3	3.9	4.8	21.1	20.7	19.1
	MAE [*]	22.7	47.5	38.3	105.5	123.6	107.1
	RMSE [*]	4.8	6.6	7.5	29.4	29.4	26.3
	R^2	0.923	0.858	0.787	0.928	0.923	0.955
A320-200 Twin opt	Alg. [4]	CGF	CGF	CGB	CGP	OSS	OSS
	Arch. [5]	17-10-10-1	17-10-1	17-10-1	19-5-5-1	19-5-5-1	19-5-5-1
	AAE [*]	3.7	3.3	5.2	20.7	21.1	20.3
	MAE [*]	33.7	18.4	44.7	96.5	121.3	103.3
	RMSE [*]	5.5	4.7	7.8	29.1	30.2	28.9
	R^2	0.888	0.916	0.794	0.931	0.920	0.946
A321-100 opt	Alg. [4]	CGP	CGF	CGB	OSS	OSS	CGF
	Arch. [5]	17-10-1	17-15-15-1	17-10-1	19-5-5-1	19-5-5-1	19-5-5-1
	AAE [*]	3.9	4.2	5.4	19.4	20.0	23.0
	MAE [*]	41.4	28.5	37.0	99.8	103.7	113.3
	RMSE [*]	6.2	6.4	7.9	26.7	27.5	33.1
	R^2	0.914	0.890	0.877	0.926	0.919	0.912
A321-100 std	Alg. [4]	OSS	OSS	CGF	CGP	CGF	CGF
	Arch. [5]	17-10-1	17-10-10-1	17-10-1	19-5-5-1	19-5-5-1	19-5-5-1
	AAE [*]	3.8	4.2	4.9	18.6	18.0	19.1
	MAE [*]	37.2	24.0	38.7	109.8	92.9	104.1
	RMSE [*]	5.9	6.1	7.1	24.7	24.4	27.3
	R^2	0.915	0.895	0.871	0.941	0.944	0.948

Note: [1] $\sigma_{XX\text{-}Max\text{-}Top\text{-}Tens.}$, [2] $\sigma_{YY\text{-}Max\text{-}Top\text{-}Tens.}$, [3] $\sigma_{1\text{-}Max\text{-}Top\text{-}Tens.}$, [4] Training Algorithm, [5] ANN Model Architecture, [*] The unit is (psi)

Table 4.1 (Continued)

Aircraft	Accuracy Criteria	Top Tensile Stresses					
		Mechanical Loading			Simultaneous Temperature and Mechanical Loading		
		$\sigma_{XX\text{-}Max}$ [1]	$\sigma_{YY\text{-}Max}$ [2]	$\sigma_{1\text{-}Max}$ [3]	$\sigma_{XX\text{-}Max}$ [1]	$\sigma_{YY\text{-}Max}$ [2]	$\sigma_{1\text{-}Max}$ [3]
A321-200 opt	Alg. [4]	OSS	CGB	CGB	CGP	CGP	CGP
	Arch. [5]	17-10-1	17-10-1	17-10-1	19-5-5-1	19-5-5-1	19-5-5-1
	AAE [*]	4.3	4.1	5.2	20.9	21.5	21.4
	MAE [*]	49.2	53.6	38.0	146.2	143.6	89.6
	RMSE [*]	6.8	6.6	7.6	30.4	31.7	28.8
	R^2	0.875	0.868	0.877	0.928	0.925	0.941
A321-200 std	Alg. [4]	CGF	CGB	OSS	LM	OSS	OSS
	Arch. [5]	17-10-1	17-15-1	17-5-1	19-5-5-1	19-5-5-1	19-5-5-1
	AAE [*]	4.1	4.2	5.0	18.5	19.7	20.8
	MAE [*]	44.9	50.8	35.5	118.4	147.2	125.2
	RMSE [*]	6.8	6.6	7.1	27.0	29.3	30.1
	R^2	0.876	0.883	0.852	0.946	0.936	0.945
A330-200 opt	Alg. [4]	CGF	CGB	CGP	OSS	CGF	CGP
	Arch. [5]	17-10-1	17-15-1	17-15-1	19-5-5-1	19-5-5-1	19-5-5-1
	AAE [*]	5.5	5.4	6.9	21.4	20.9	25.8
	MAE [*]	33.3	26.2	40.5	115.3	106.7	143.1
A330-200 std	Alg. [4]	OSS	CGF	OSS	CGP	OSS	CGB
	Arch. [5]	17-10-10-1	17-20-1	17-25-1	19-5-5-1	19-5-5-1	19-5-5-1
	AAE [*]	5.2	4.9	6.2	20.2	23.5	22.2
	MAE [*]	25.3	20.3	49.9	111.4	115.5	157.2
	RMSE [*]	6.9	6.3	8.8	28.0	32.1	33.3
	R^2	0.934	0.940	0.898	0.948	0.930	0.934
A330-300 opt	Alg. [4]	LM	CGB	CGP	OSS	CGP	CGP
	Arch. [5]	17-5-5-1	17-10-1	17-20-1	19-5-5-1	19-5-5-1	19-5-5-1
	AAE [*]	5.6	5.9	6.7	20.8	21.9	22.2
	MAE [*]	29.2	34.4	39.1	124.9	96.6	116.5
	RMSE [*]	7.5	8.1	9.6	27.8	28.7	31.7
	R^2	0.924	0.904	0.882	0.934	0.932	0.939
A330-300 std	Alg. [4]	LM	CGP	OSS	CGB	CGF	CGF
	Arch. [5]	17-5-5-1	17-10-1	17-25-1	19-5-5-1	19-5-5-1	19-5-5-1
	AAE [*]	5.0	5.0	6.4	20.3	20.0	23.6
	MAE [*]	27.9	30.1	49.9	97.8	110.9	146.1
	RMSE [*]	6.7	6.8	9.1	26.4	27.2	34.1
	R^2	0.938	0.931	0.891	0.946	0.938	0.927
A340-200 opt	Alg. [4]	CGF	CGF	CGP	LM	CGB	OSS
	Arch. [5]	17-10-1	17-10-1	17-15-1	19-5-5-1	19-10-10-1	19-5-5-1
	AAE [*]	5.3	4.9	5.9	21.5	21.7	19.6
	MAE [*]	42.7	25.9	37.5	108.1	108.5	114.0
	RMSE [*]	7.6	6.7	7.8	30.8	30.4	29.0
	R^2	0.905	0.916	0.909	0.931	0.934	0.949

Note: [1] $\sigma_{XX\text{-}Max\text{-}Top\text{-}Tens.}$, [2] $\sigma_{YY\text{-}Max\text{-}Top\text{-}Tens.}$, [3] $\sigma_{1\text{-}Max\text{-}Top\text{-}Tens.}$, [4] Training Algorithm, [5] ANN Model Architecture, [*] The unit is (psi)

Table 4.1 (Continued)

Aircraft	Accuracy Criteria	Top Tensile Stresses					
		Mechanical Loading			Simultaneous Temperature and Mechanical Loading		
		$\sigma_{XX\text{-}Max}$ [1]	$\sigma_{YY\text{-}Max}$ [2]	$\sigma_{1\text{-}Max}$ [3]	$\sigma_{XX\text{-}Max}$ [1]	$\sigma_{YY\text{-}Max}$ [2]	$\sigma_{1\text{-}Max}$ [3]
A340-200 std	Alg. [4]	CGP	LM	CGB	CGP	CGP	CGB
	Arch. [5]	17-5-5-1	17-10-10-1	17-20-20-1	19-5-5-1	19-5-5-1	19-5-5-1
	AAE [*]	4.4	4.1	5.6	22.5	22.3	19.5
	MAE [*]	21.4	28.8	36.4	102.2	103.9	127.5
	RMSE [*]	5.9	5.7	7.9	30.1	29.7	27.1
	R^2	0.943	0.942	0.894	0.922	0.923	0.959
A340-300 opt	Alg. [4]	OSS	CGB	CGP	CGF	OSS	OSS
	Arch. [5]	17-10-10-1	17-10-1	17-10-10-1	19-5-5-1	19-5-5-1	19-5-5-1
	AAE [*]	5.0	5.2	5.5	21.7	22.1	21.7
	MAE [*]	51.2	29.2	49.9	140.7	124.9	102.7
	RMSE [*]	7.6	7.5	8.5	30.7	30.7	30.2
	R^2	0.916	0.906	0.903	0.937	0.937	0.931
A340-300 std	Alg. [4]	OSS	CGF	CGF	CGF	CGF	OSS
	Arch. [5]	17-10-10-1	17-15-1	17-10-10-1	19-5-5-1	19-5-5-1	19-5-5-1
	AAE [*]	5.4	5.5	5.4	22.1	24.7	26.3
	MAE [*]	37.2	30.3	60.3	112.0	125.9	139.0
	RMSE [*]	7.4	7.6	8.4	30.8	34.1	36.6
	R^2	0.919	0.903	0.931	0.937	0.921	0.914
A340-500 opt	Alg. [4]	CGP	CGF	CGB	CGF	LM	CGF
	Arch. [5]	17-10-10-1	17-10-1	17-5-5-1	19-5-5-1	19-5-5-1	19-5-5-1
	AAE [*]	5.2	6.4	6.5	21.3	21.3	23.0
	MAE [*]	57.1	41.5	34.2	94.6	103.8	125.8
	RMSE [*]	8.5	8.9	9.6	29.2	28.7	32.2
	R^2	0.925	0.905	0.910	0.943	0.948	0.935
A340-500 std	Alg. [4]	CGF	OSS	CGP	OSS	CGB	CGP
	Arch. [5]	17-15-15-1	17-10-1	17-15-1	19-5-5-1	19-5-5-1	19-5-5-1
	AAE [*]	5.7	5.7	6.8	22.1	24.1	22.7
	MAE [*]	65.6	30.5	51.4	99.1	123.2	117.0
	RMSE [*]	8.4	7.6	9.5	29.0	32.5	31.9
	R^2	0.919	0.925	0.907	0.944	0.930	0.935
A340-600 opt	Alg. [4]	CGP	CGF	CGP	OSS	OSS	CGF
	Arch. [5]	17-10-10-1	17-10-10-1	17-15-15-1	19-5-5-1	19-5-5-1	19-5-5-1
	AAE [*]	5.2	5.8	7.4	20.3	21.2	21.5
	MAE [*]	57.1	59.0	56.7	120.5	133.9	145.4
	RMSE [*]	8.5	8.8	10.2	27.5	28.8	30.4
	R^2	0.925	0.907	0.907	0.946	0.941	0.937
A340-600 std	Alg. [4]	CGP	CGF	CGP	CGP	CGB	OSS
	Arch. [5]	17-20-1	17-10-1	17-15-1	19-5-5-1	19-5-5-1	19-5-5-1
	AAE [*]	6.1	6.0	7.2	21.0	21.8	21.6
	MAE [*]	50.1	35.9	48.4	92.0	130.1	118.1
	RMSE [*]	8.7	8.4	9.7	28.1	30.6	29.3
	R^2	0.911	0.905	0.899	0.943	0.927	0.930

Note: [1] $\sigma_{XX\text{-}Max\text{-}Top\text{-}Tens.}$, [2] $\sigma_{YY\text{-}Max\text{-}Top\text{-}Tens.}$, [3] $\sigma_{1\text{-}Max\text{-}Top\text{-}Tens.}$, [4] Training Algorithm, [5] ANN Model Architecture, [*] The unit is (psi)

Table 4.1 (Continued)

Aircraft	Accuracy Criteria	Top Tensile Stresses					
		Mechanical Loading			Simultaneous Temperature and Mechanical Loading		
		$\sigma_{XX\text{-}Max}$ [1]	$\sigma_{YY\text{-}Max}$ [2]	$\sigma_{1\text{-}Max}$ [3]	$\sigma_{XX\text{-}Max}$ [1]	$\sigma_{YY\text{-}Max}$ [2]	$\sigma_{1\text{-}Max}$ [3]
A380-800	Alg. [4]	OSS	CGB	CGB	CGB	LM	OSS
	Arch. [5]	17-5-5-1	17-15-15-1	17-15-1	19-5-5-1	19-5-5-1	19-5-5-1
	AAE [*]	8.6	8.7	10.0	21.9	22.6	24.7
	MAE [*]	53.1	63.0	48.6	126.1	174.2	126.8
	RMSE [*]	12.2	12.1	13.3	29.5	31.7	33.4
	R^2	0.929	0.930	0.930	0.959	0.949	0.947
Adv.B727-200 Option	Alg. [4]	CGB	CGF	LM	OSS	CGP	LM
	Arch. [5]	17-10-1	17-10-1	17-5-5-1	19-5-5-1	19-5-5-1	19-5-5-1
	AAE [*]	4.2	4.0	5.2	18.2	19.3	22.5
	MAE [*]	42.2	62.8	29.8	98.4	106.8	111.2
	RMSE [*]	6.5	6.9	7.7	25.4	25.7	31.1
	R^2	0.909	0.894	0.893	0.941	0.939	0.936
Adv.B727-200c	Alg. [4]	CGF	CGP	CGP	CGF	OSS	CGP
	Arch. [5]	17-15-1	17-10-1	17-10-1	19-5-5-1	19-5-5-1	19-5-5-1
	AAE [*]	3.5	3.6	4.8	18.9	17.7	19.3
	MAE [*]	30.9	23.1	46.3	137.3	89.9	136.3
	RMSE [*]	5.4	5.0	7.8	26.0	25.1	28.2
	R^2	0.913	0.917	0.886	0.944	0.946	0.931
Adv.B737-200	Alg. [4]	CGP	OSS	CGP	CGB	CGB	CGP
	Arch. [5]	17-5-5-1	17-10-1	17-10-1	19-5-1	19-5-5-1	19-10-10-1
	AAE [*]	2.3	2.0	2.7	20.4	19.2	20.8
	MAE [*]	14.9	14.8	17.9	113.4	130.0	113.8
	RMSE [*]	3.3	3.0	3.9	28.3	27.8	28.4
	R^2	0.922	0.929	0.895	0.926	0.932	0.944
B707-320C	Alg. [4]	CGB	CGP	CGP	CGP	OSS	CGF
	Arch. [5]	17-15-1	17-25-1	17-20-1	19-5-5-1	19-5-5-1	19-5-5-1
	AAE [*]	4.9	4.3	4.6	19.8	19.9	20.3
	MAE [*]	39.2	24.7	44.2	128.1	131.1	126.1
	RMSE [*]	7.2	5.7	7.1	28.3	29.2	29.6
	R^2	0.916	0.946	0.922	0.928	0.924	0.938
B717-200 HGW	Alg. [4]	OSS	OSS	CGP	CGP	CGB	OSS
	Arch. [5]	17-10-1	17-5-5-1	17-5-5-1	19-5-5-1	19-10-10-1	19-5-5-1
	AAE [*]	2.5	2.9	3.2	17.0	16.9	18.0
	MAE [*]	19.1	38.5	43.4	100.9	111.8	91.6
	RMSE [*]	3.7	4.6	5.0	23.4	25.0	25.4
	R^2	0.920	0.868	0.860	0.947	0.942	0.948
B720B	Alg. [4]	OSS	CGP	CGB	OSS	OSS	LM
	Arch. [5]	17-15-1	17-10-1	17-10-1	19-5-5-1	19-10-1	19-5-5-1
	AAE [*]	3.3	2.8	3.4	23.3	22.7	20.1
	MAE [*]	24.0	11.8	16.9	156.5	135.9	114.8
	RMSE [*]	4.9	3.6	4.6	34.2	32.8	28.5
	R^2	0.926	0.959	0.939	0.905	0.912	0.940

Note: [1] $\sigma_{XX\text{-}Max\text{-}Top\text{-}Tens.}$, [2] $\sigma_{YY\text{-}Max\text{-}Top\text{-}Tens.}$, [3] $\sigma_{1\text{-}Max\text{-}Top\text{-}Tens.}$, [4] Training Algorithm, [5] ANN Model Architecture, [*] The unit is (psi)

Table 4.1 (Continued)

Aircraft	Accuracy Criteria	Top Tensile Stresses					
		Mechanical Loading			Simultaneous Temperature and Mechanical Loading		
		$\sigma_{XX\text{-}Max}$ [1]	$\sigma_{YY\text{-}Max}$ [2]	$\sigma_{1\text{-}Max}$ [3]	$\sigma_{XX\text{-}Max}$ [1]	$\sigma_{YY\text{-}Max}$ [2]	$\sigma_{1\text{-}Max}$ [3]
B727-100C	Alg. [4]	CGB	CGF	CGB	CGB	CGP	LM
	Arch. [5]	17-15-1	17-10-1	17-10-1	19-5-5-1	19-10-10-1	19-5-5-1
	AAE [*]	3.3	3.7	4.7	21.9	21.4	20.6
	MAE [*]	21.6	48.6	38.1	110.1	99.6	97.9
	RMSE [*]	4.6	6.7	7.1	30.0	29.1	28.3
	R^2	0.937	0.870	0.817	0.926	0.925	0.935
B737 BBJ2	Alg. [4]	CGP	OSS	LM	CGB	CGP	OSS
	Arch. [5]	17-5-5-1	17-10-1	17-10-1	19-5-5-1	19-5-5-1	19-5-5-1
	AAE [*]	3.9	3.5	5.5	17.4	19.0	22.8
	MAE [*]	38.8	21.8	38.4	154.9	101.8	103.4
	RMSE [*]	6.3	5.0	7.6	26.1	25.4	30.9
	R^2	0.843	0.896	0.841	0.935	0.937	0.926
B737-100	Alg. [4]	OSS	CGF	LM	CGF	CGF	CGP
	Arch. [5]	17-15-1	17-5-5-1	17-5-1	19-5-5-1	19-5-5-1	19-10-10-1
	AAE [*]	2.5	2.7	3.8	18.7	18.6	18.4
	MAE [*]	12.1	17.7	33.4	110.1	112.8	125.8
	RMSE [*]	3.3	4.0	6.0	27.1	27.3	26.2
	R^2	0.923	0.898	0.839	0.922	0.922	0.931
B737-200	Alg. [4]	OSS	CGF	LM	OSS	LM	CGB
	Arch. [5]	17-10-1	17-10-1	17-10-10-1	19-10-1	19-5-5-1	19-5-5-1
	AAE [*]	2.7	3.4	4.1	18.0	17.2	18.3
	MAE [*]	20.5	39.7	43.8	107.8	106.3	102.7
	RMSE [*]	3.9	5.6	6.4	25.4	24.4	27.3
	R^2	0.892	0.779	0.752	0.934	0.941	0.934
B737-300	Alg. [4]	CGF	LM	OSS	CGP	CGB	CGB
	Arch. [5]	17-20-1	17-20-1	17-15-1	19-5-5-1	19-5-5-1	19-5-5-1
	AAE [*]	3.2	4.1	4.5	18.4	18.8	20.2
	MAE [*]	23.5	44.1	46.2	123.1	118.4	109.8
	RMSE [*]	4.4	6.3	7.1	26.9	27.4	28.7
	R^2	0.909	0.806	0.794	0.936	0.936	0.936
B737-400	Alg. [4]	CGP	CGP	OSS	CGF	CGF	OSS
	Arch. [5]	17-20-1	17-5-5-1	17-10-1	19-5-5-1	19-5-5-1	19-5-5-1
	AAE [*]	3.2	4.2	4.1	20.6	19.7	18.9
	MAE [*]	25.7	58.6	23.8	101.9	111.5	114.6
	RMSE [*]	4.6	7.2	5.7	29.8	29.0	27.7
	R^2	0.925	0.829	0.876	0.926	0.924	0.941
B737-500	Alg. [4]	CGP	LM	CGP	OSS	CGP	LM
	Arch. [5]	17-10-1	17-5-5-1	17-5-1	19-5-5-1	19-5-5-1	19-5-5-1
	AAE [*]	3.0	3.7	4.3	18.3	17.7	18.0
	MAE [*]	19.2	31.8	38.0	100.3	94.7	102.8
	RMSE [*]	4.1	5.6	6.4	24.7	23.6	24.9
	R^2	0.913	0.822	0.807	0.946	0.950	0.954

Note: [1] $\sigma_{XX\text{-}Max\text{-}Top\text{-}Tens.}$, [2] $\sigma_{YY\text{-}Max\text{-}Top\text{-}Tens.}$, [3] $\sigma_{1\text{-}Max\text{-}Top\text{-}Tens.}$, [4] Training Algorithm, [5] ANN Model Architecture, [*] The unit is (psi)

Table 4.1 (Continued)

Aircraft	Accuracy Criteria	Top Tensile Stresses					
		Mechanical Loading			Simultaneous Temperature and Mechanical Loading		
		$\sigma_{XX\text{-}Max}$ [1]	$\sigma_{YY\text{-}Max}$ [2]	$\sigma_{1\text{-}Max}$ [3]	$\sigma_{XX\text{-}Max}$ [1]	$\sigma_{YY\text{-}Max}$ [2]	$\sigma_{1\text{-}Max}$ [3]
B737-600	Alg. [4]	CGB	CGP	OSS	CGB	CGP	CGP
	Arch. [5]	17-15-1	17-10-1	17-5-1	19-10-1	19-5-5-1	19-5-5-1
	AAE [*]	3.0	3.1	4.2	19.5	17.4	20.2
	MAE [*]	33.0	21.1	31.6	115.9	119.9	102.3
	RMSE [*]	4.6	4.5	6.0	26.8	25.8	28.6
	R^2	0.882	0.871	0.814	0.938	0.942	0.942
B737-700	Alg. [4]	CGP	CGB	OSS	LM	OSS	LM
	Arch. [5]	17-5-5-1	17-10-1	17-10-1	19-5-5-1	19-10-10-1	19-5-5-1
	AAE [*]	3.2	3.9	4.6	19.8	21.1	20.5
	MAE [*]	21.4	50.3	26.2	125.9	100.9	117.0
	RMSE [*]	4.6	6.6	6.6	28.8	29.5	30.0
	R^2	0.925	0.853	0.847	0.931	0.922	0.935
B737-800	Alg. [4]	CGP	OSS	OSS	CGF	LM	LM
	Arch. [5]	17-30-1	17-10-1	17-10-1	19-5-5-1	19-5-5-1	19-5-5-1
	AAE [*]	3.9	3.6	5.1	18.4	19.3	21.0
	MAE [*]	36.5	22.6	35.6	91.1	94.2	126.4
	RMSE [*]	6.3	5.0	7.5	24.8	25.3	29.5
	R^2	0.848	0.895	0.821	0.948	0.944	0.934
B737-900ER	Alg. [4]	LM	LM	CGB	CGF	CGF	OSS
	Arch. [5]	17-15-15-1	17-10-10-1	17-5-1	19-5-5-1	19-5-5-1	19-5-5-1
	AAE [*]	4.2	4.5	5.7	17.4	18.3	20.2
	MAE [*]	35.1	35.2	62.0	113.8	91.8	88.5
	RMSE [*]	6.1	6.8	9.6	24.7	24.1	26.5
	R^2	0.898	0.857	0.805	0.938	0.943	0.939
B747-100 SF	Alg. [4]	OSS	CGB	CGB	CGB	CGB	CGP
	Arch. [5]	17-10-10-1	17-25-1	17-10-1	19-5-5-1	19-5-5-1	19-5-5-1
	AAE [*]	4.8	5.0	5.3	20.3	20.3	22.1
	MAE [*]	26.6	39.6	47.5	107.2	140.3	107.5
	RMSE [*]	6.7	7.1	7.6	28.5	29.6	30.8
	R^2	0.928	0.916	0.913	0.939	0.937	0.941
B747-200B	Alg. [4]	CGP	OSS	CGP	CGF	CGP	CGF
	Arch. [5]	17-15-1	17-10-1	17-15-1	19-5-5-1	19-5-5-1	19-5-5-1
	AAE [*]	4.8	4.8	5.5	20.5	20.8	22.8
	MAE [*]	26.2	25.4	31.5	94.8	93.9	128.5
	RMSE [*]	6.5	6.2	7.7	27.9	28.0	32.4
	R^2	0.945	0.946	0.916	0.937	0.936	0.935
B747-300	Alg. [4]	OSS	LM	CGP	OSS	OSS	CGB
	Arch. [5]	17-25-1	17-30-1	17-15-1	19-5-5-1	19-5-5-1	19-5-5-1
	AAE [*]	6.1	5.2	5.3	21.4	21.9	21.6
	MAE [*]	43.6	36.4	35.2	108.3	128.0	118.8
	RMSE [*]	8.2	7.8	7.4	30.5	31.4	31.4
	R^2	0.900	0.898	0.920	0.937	0.931	0.939

Note: [1] $\sigma_{XX\text{-}Max\text{-}Top\text{-}Tens.}$, [2] $\sigma_{YY\text{-}Max\text{-}Top\text{-}Tens.}$, [3] $\sigma_{1\text{-}Max\text{-}Top\text{-}Tens.}$, [4] Training Algorithm, [5] ANN Model Architecture, [*] The unit is (psi)

Table 4.1 (Continued)

Aircraft	Accuracy Criteria	Top Tensile Stresses					
		Mechanical Loading			Simultaneous Temperature and Mechanical Loading		
		$\sigma_{XX\text{-}Max}$ [1]	$\sigma_{YY\text{-}Max}$ [2]	$\sigma_{1\text{-}Max}$ [3]	$\sigma_{XX\text{-}Max}$ [1]	$\sigma_{YY\text{-}Max}$ [2]	$\sigma_{1\text{-}Max}$ [3]
B747-400ER Passenger	Alg. [4]	LM	LM	CGF	LM	CGP	CGB
	Arch. [5]	17-10-10-1	17-10-10-1	17-20-1	19-5-5-1	19-5-5-1	19-5-5-1
	AAE [*]	5.8	5.3	6.1	22.5	22.0	22.2
	MAE [*]	38.7	46.4	34.4	136.8	133.9	171.6
	RMSE [*]	8.4	8.0	8.2	30.8	30.3	32.3
	R^2	0.912	0.909	0.930	0.940	0.940	0.941
B747-400ER Freighter	Alg. [4]	CGB	CGB	OSS	CGF	LM	OSS
	Arch. [5]	17-25-1	17-10-10-1	17-20-1	19-5-5-1	19-5-5-1	19-10-10-1
	AAE [*]	6.4	5.5	6.1	20.5	21.7	20.2
	MAE [*]	40.2	57.3	52.1	142.6	112.1	113.1
	RMSE [*]	9.0	8.8	8.9	28.1	30.1	29.2
	R^2	0.898	0.890	0.905	0.937	0.929	0.944
B747-400B	Alg. [4]	CGB	CGF	CGB	CGF	CGP	LM
	Arch. [5]	17-20-1	17-15-1	17-10-10-1	19-10-10-1	19-5-5-1	19-5-5-1
	AAE [*]	4.9	5.4	5.2	21.6	20.5	22.7
	MAE [*]	28.0	40.5	34.4	120.5	141.0	155.4
	RMSE [*]	6.7	7.9	7.2	29.1	30.4	33.4
	R^2	0.936	0.910	0.940	0.946	0.938	0.940
B747-SP	Alg. [4]	CGF	CGF	OSS	OSS	CGB	OSS
	Arch. [5]	17-25-1	17-15-1	17-5-5-1	19-5-5-1	19-5-5-1	19-5-5-1
	AAE [*]	4.4	4.7	4.6	20.3	21.0	21.2
	MAE [*]	18.4	41.9	40.5	121.1	105.1	130.3
	RMSE [*]	5.9	6.7	7.1	28.7	29.2	28.8
	R^2	0.939	0.916	0.944	0.926	0.922	0.946
B747-8	Alg. [4]	CGF	CGB	CGP	CGP	OSS	CGB
	Arch. [5]	17-20-1	17-10-1	17-45-1	19-5-5-1	19-5-5-1	19-5-5-1
	AAE [*]	6.4	6.7	9.7	22.6	22.7	23.9
	MAE [*]	29.7	36.1	56.0	142.0	105.1	136.2
	RMSE [*]	9.1	8.9	12.6	31.7	30.7	33.3
	R^2	0.912	0.907	0.872	0.929	0.930	0.926
B757-200	Alg. [4]	CGB	CGP	CGB	CGB	CGB	OSS
	Arch. [5]	17-10-1	17-20-1	17-10-10-1	19-10-10-1	19-5-5-1	19-5-5-1
	AAE [*]	3.6	3.2	3.5	20.5	18.9	20.4
	MAE [*]	23.9	20.0	18.4	108.0	100.8	111.4
	RMSE [*]	5.0	4.7	5.0	28.0	25.6	29.1
	R^2	0.935	0.937	0.935	0.935	0.942	0.942
B757-300	Alg. [4]	CGF	CGF	CGP	CGP	CGB	CGF
	Arch. [5]	17-10-1	17-10-1	17-15-1	19-15-15-1	19-5-5-1	19-5-5-1
	AAE [*]	4.0	3.5	3.9	17.6	18.9	19.5
	MAE [*]	19.3	20.3	21.7	110.8	111.7	93.0
	RMSE [*]	5.5	4.7	5.5	25.1	26.3	25.5
	R^2	0.917	0.935	0.923	0.953	0.948	0.951

Note: [1] $\sigma_{XX\text{-}Max\text{-}Top\text{-}Tens.}$, [2] $\sigma_{YY\text{-}Max\text{-}Top\text{-}Tens.}$, [3] $\sigma_{1\text{-}Max\text{-}Top\text{-}Tens.}$, [4] Training Algorithm, [5] ANN Model Architecture, [*] The unit is (psi)

Table 4.1 (Continued)

Aircraft	Accuracy Criteria	Top Tensile Stresses					
		Mechanical Loading			Simultaneous Temperature and Mechanical Loading		
		$\sigma_{XX\text{-}Max}$ [1]	$\sigma_{YY\text{-}Max}$ [2]	$\sigma_{1\text{-}Max}$ [3]	$\sigma_{XX\text{-}Max}$ [1]	$\sigma_{YY\text{-}Max}$ [2]	$\sigma_{1\text{-}Max}$ [3]
B767-200	Alg. [4]	CGP	LM	OSS	CGP	CGF	CGP
	Arch. [5]	17-10-1	17-10-1	17-15-1	19-10-1	19-5-5-1	19-5-5-1
	AAE [*]	3.8	3.8	5.2	18.8	19.7	21.4
	MAE [*]	19.7	20.0	30.2	87.4	109.3	104.3
	RMSE [*]	5.2	5.2	7.1	25.4	26.3	29.5
	R^2	0.919	0.913	0.934	0.945	0.939	0.944
B767-200 ER	Alg. [4]	CGP	LM	CGP	CGP	CGP	CGB
	Arch. [5]	17-20-20-1	17-10-1	17-15-1	19-10-1	19-10-10-1	19-5-5-1
	AAE [*]	4.4	4.5	5.2	19.9	21.9	22.1
	MAE [*]	19.1	29.2	35.4	101.8	96.5	139.6
	RMSE [*]	6.0	6.3	7.6	26.6	29.4	31.4
	R^2	0.948	0.939	0.909	0.944	0.934	0.934
B767-300 ER	Alg. [4]	CGF	CGB	CGP	CGF	OSS	CGB
	Arch. [5]	17-5-1	17-10-10-1	17-20-20-1	19-5-5-1	19-5-5-1	19-5-5-1
	AAE [*]	4.9	4.7	5.5	20.7	20.7	20.5
	MAE [*]	22.6	22.5	30.0	128.7	127.6	126.1
	RMSE [*]	6.5	6.4	7.7	29.5	30.3	29.3
	R^2	0.944	0.941	0.951	0.942	0.938	0.938
B767-400	Alg. [4]	CGF	OSS	CGP	LM	OSS	OSS
	Arch. [5]	17-25-1	17-10-1	17-5-1	19-5-5-1	19-5-5-1	19-10-1
	AAE [*]	6.2	5.6	4.8	22.4	21.2	21.1
	MAE [*]	56.7	48.0	22.3	126.1	114.4	136.5
	RMSE [*]	9.1	8.0	6.3	31.2	29.0	29.6
	R^2	0.896	0.910	0.955	0.935	0.937	0.946
B777-200 Baseline	Alg. [4]	CGF	CGF	CGP	OSS	OSS	CGF
	Arch. [5]	17-10-1	17-15-1	17-20-1	19-5-5-1	19-5-5-1	19-5-5-1
	AAE [*]	4.6	4.4	4.8	22.3	20.8	22.6
	MAE [*]	20.8	21.0	48.3	91.4	84.8	115.6
	RMSE [*]	6.0	5.9	7.3	29.9	28.3	31.8
	R^2	0.943	0.941	0.916	0.929	0.933	0.941
B777-200 ER	Alg. [4]	CGF	LM	CGB	CGP	CGB	CGP
	Arch. [5]	17-15-1	17-10-10-1	17-15-1	19-5-5-1	19-5-5-1	19-5-5-1
	AAE [*]	5.2	5.2	6.5	21.5	23.3	19.7
	MAE [*]	33.7	33.6	52.9	101.9	100.4	88.9
	RMSE [*]	7.3	7.5	9.0	29.2	30.4	27.8
	R^2	0.933	0.930	0.917	0.936	0.936	0.944
B777-200 LR	Alg. [4]	OSS	CGP	LM	CGP	CGP	CGF
	Arch. [5]	17-15-1	17-10-10-1	17-10-10-1	19-5-5-1	19-5-5-1	19-5-5-1
	AAE [*]	6.2	5.4	7.1	19.4	20.7	22.5
	MAE [*]	37.0	34.6	44.5	69.3	79.7	110.0
	RMSE [*]	9.0	7.8	10.0	24.5	27.1	30.5
	R^2	0.928	0.943	0.928	0.961	0.953	0.948

Note: [1] $\sigma_{XX\text{-}Max\text{-}Top\text{-}Tens.}$, [2] $\sigma_{YY\text{-}Max\text{-}Top\text{-}Tens.}$, [3] $\sigma_{1\text{-}Max\text{-}Top\text{-}Tens.}$, [4] Training Algorithm, [5] ANN Model, Architecture, [*] The unit is (psi)

Table 4.1 (Continued)

Aircraft	Accuracy Criteria	Top Tensile Stresses					
		Mechanical Loading			Simultaneous Temperature and Mechanical Loading		
		$\sigma_{XX\text{-}Max}$ [1]	$\sigma_{YY\text{-}Max}$ [2]	$\sigma_{1\text{-}Max}$ [3]	$\sigma_{XX\text{-}Max}$ [1]	$\sigma_{YY\text{-}Max}$ [2]	$\sigma_{1\text{-}Max}$ [3]
B777-300 Baseline	Alg. [4]	CGP	CGP	CGF	OSS	CGB	OSS
	Arch. [5]	17-15-1	17-10-1	17-10-10-1	19-5-5-1	19-5-5-1	19-5-5-1
	AAE [*]	5.4	5.6	5.6	23.8	23.5	24.2
	MAE [*]	41.9	40.3	41.7	117.3	138.4	190.5
	RMSE [*]	7.7	8.0	8.1	32.1	33.3	35.1
	R^2	0.927	0.922	0.936	0.924	0.919	0.919
B787-8	Alg. [4]	LM	CGF	CGP	LM	CGF	LM
	Arch. [5]	17-15-1	17-10-1	17-10-1	19-5-5-1	19-5-5-1	19-5-5-1
	AAE [*]	5.2	5.6	5.5	24.0	23.3	23.9
	MAE [*]	23.9	31.6	49.4	123.7	125.3	117.7
	RMSE [*]	6.9	7.5	8.3	33.7	32.5	32.8
	R^2	0.947	0.932	0.931	0.902	0.912	0.923
B777-300 ER	Alg. [4]	OSS	OSS	CGB	CGF	OSS	CGP
	Arch. [5]	17-15-1	17-10-1	17-15-1	19-5-5-1	19-5-5-1	19-5-5-1
	AAE [*]	6.1	5.3	7.3	24.3	25.2	28.6
	MAE [*]	32.3	45.3	33.7	120.6	140.7	160.7
	RMSE [*]	8.3	7.7	9.9	33.2	34.6	40.9
	R^2	0.947	0.957	0.953	0.925	0.916	0.919

Note: [1] $\sigma_{XX\text{-}Max\text{-}Top\text{-}Tens.}$, [2] $\sigma_{YY\text{-}Max\text{-}Top\text{-}Tens.}$, [3] $\sigma_{1\text{-}Max\text{-}Top\text{-}Tens.}$, [4] Training Algorithm, [5] ANN Model Architecture, [*] The unit is (psi)

Mechanical Loading Only

Figures 4.1 through 4.3 present ANN model critical response predictions compared with NIKE3D-FAA FEM solutions for (a) $\sigma_{XX\text{-}Max\text{-}Top\text{-}Tens.}$, (b) $\sigma_{YY\text{-}Max\text{-}Top\text{-}Tens.}$, and (c) $\sigma_{1\text{-}Max\text{-}Top\text{-}Tens.}$ under mechanical loading of four types of aircraft: B777-300 ER, B747-8, A380-800, and A340-500 opt. Displaying the accuracy of the ANN models, R^2 and RMSE have been separately presented in each figure for each training, testing, validation, and independent testing dataset. ANN models were found to successfully replicate FEAFAA/NIKE3D-FAA pavement response solutions for all four types of aircraft. Validation and test sets produced high accuracy similar to that of the training set for all pavement response types, proving ANN models' lack of generalization (i.e., they did not memorize the relationship), and

showing them to be robust and valid. Comparing results for all three responses shows that ANN models predict top tensile stress responses accurately.

Maximum Top Tensile Stress in X-Direction ($\sigma_{XX\text{-}Max\text{-}Top\text{-}Tens.}$)

Figure 4.1 compares NIKE3D-FAA FEM solutions to ANN predictions for the $\sigma_{XX\text{-}Max\text{-}Top\text{-}Tens.}$ for mechanical-only loading of B777-300 ER, B747-8, A380-800, and A340-500 opt. Figure 4.1 (a) shows the prediction performance of the ANN model with 17-15-1 architecture and an OSS training algorithm compared with a FEM solution for B777-300 ER.

Figure 4.1 (b) represents the performance of the B747-8's most accurate $\sigma_{XX\text{-}Max\text{-}Top\text{-}Tens.}$-ANN model (with 17-20-1 architecture and CGF training algorithm) compared with a FEM solution. As Figure 4.1 (b) displays, the ANN model is able to predict tensile stress with high accuracy for training and independent testing portions of the data with R^2 measures of 0.978 and 0.912. It can also be observed that the RMSE values are 5 (psi) for training and 9 (psi) for independent testing over a range of stresses varying from about 0 to 250 (psi). Figure 4.1 (c) represents prediction accuracy of the A380-800's ANN model with best performance for predicting $\sigma_{XX\text{-}Max\text{-}Top\text{-}Tens.}$. The model has 17-5-5-1 architecture and OSS algorithm was used to train it, and it demonstrates accuracy with R^2 values of 0.937 and 0.929 for training and independent testing and an RMSE value of 12 psi for both training and independent testing.

Figure 4.1 (d) describes the performance of the best $\sigma_{XX\text{-}Max\text{-}Top\text{-}Tens.}$-predicting model for the A340-500 opt. This model has been trained with CGP algorithm and has two hidden layers with 10 neurons in each layer (17-10-10-1). With its high accuracy in terms of an R^2 value of 0.970 for training and 0.925 for independent testing, the model is well trained and generalized so that it can ensure an adequate fit. The low RMSE value for all training,

validation, and testing sets (lower than 9 (psi)) also shows a negligible difference between ANN model prediction and the FE analysis solution.

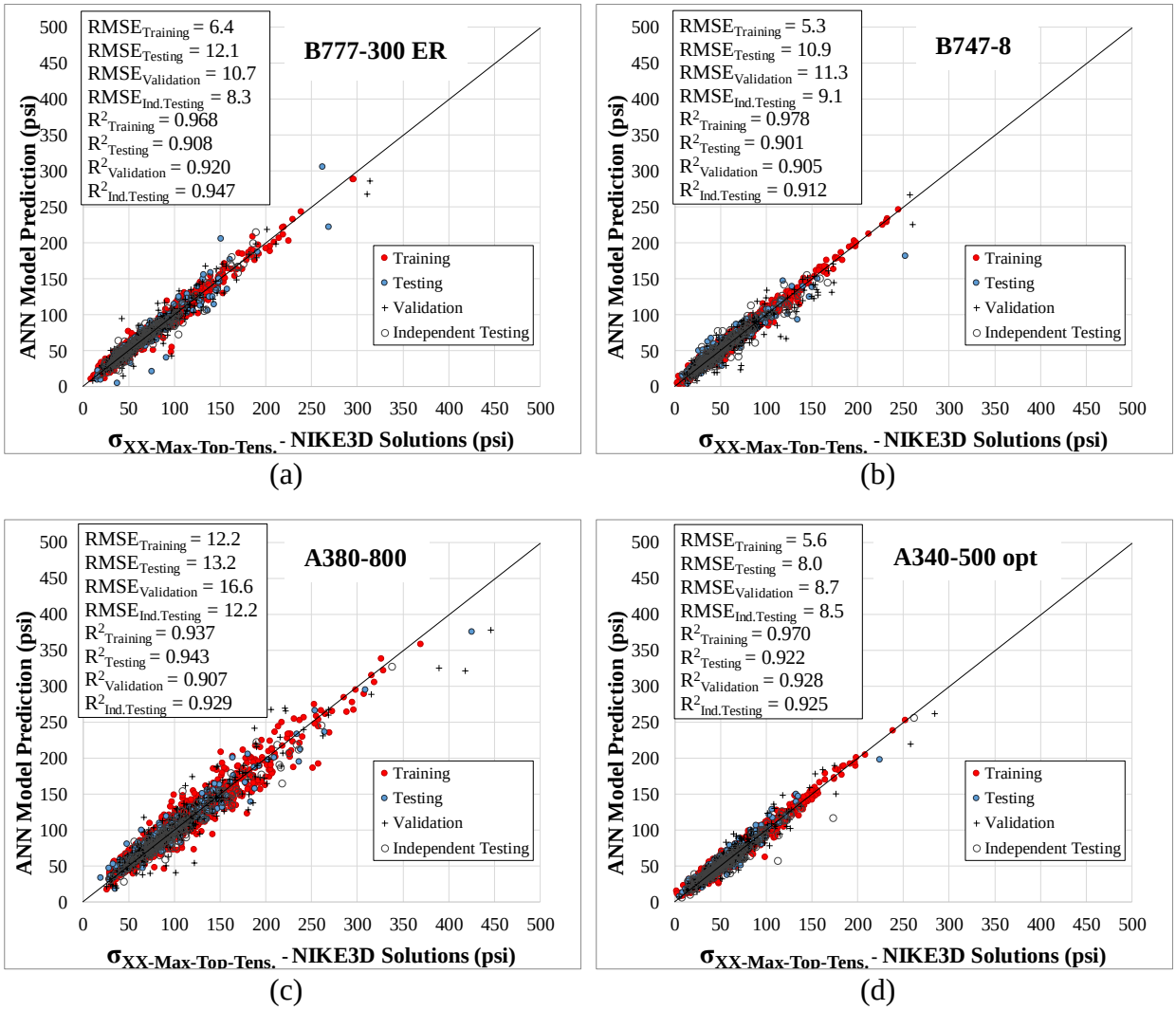

Figure 4.1 *NIKE3D FEM solution vs. ANN model prediction of the σXX-Max-Top-Tens. for (a) B777-300 ER (b) B747-8 (c) A380-800 (d) A340-500 opt mechanical loading only.*

Maximum top tensile stress in Y-direction ($\sigma_{YY\text{-}Max\text{-}Top\text{-}Tens.}$) Figure 4.2 shows a comparison between ANN predictions and NIKE3D-FAA FEM solutions of the $\sigma_{YY\text{-}Max\text{-}Top\text{-}Tens,}$ with the solution and the prediction results shown in Figure 4.2 belonging to a pavement subjected to B777-300 ER, B747-8, A380-800, and A340-500 opt mechanical loading only. Figure 4.2 (a) describes the prediction performance of the B777-300's $\sigma_{YY\text{-}Max\text{-}Top\text{-}Tens.}$—

prediction ANN model with 17-10-1 architecture and trained by an OSS training algorithm, and reflects predictions accurately fitted to values obtained by FE solutions. The model is promising for adequately predicting top tensile stress. The R^2 for training and independent testing were 0.963 and 0.957 and the RMSE for training and independent testing were 7 and 8 (psi).

Figure 4.2 (b) describes the performance of the B747-8's most accurate $\sigma_{YY\text{-}Max\text{-}Top\text{-}Tens.}$-predicting ANN model, demonstrating good fitting between predicted tensile stress and the FE solution. The R^2 and RMSE values of 0.950 and 8 (psi) for training and 0.907 and 9 (psi) for independent testing represent the promising performance of the model.

Figure 4.2 (c) shows prediction accuracy of the A380-800's $\sigma_{YY\text{-}Max\text{-}Top\text{-}Tens.}$-prediction model. Comparing the NIKE3D solution and ANN response model prediction shows a good fitting, indicating that the training R^2 and RMSE were 0.977 and 8 psi and independent testing values are 0.930 and 12 psi, respectively.

Figure 4.2 (d) shows prediction results of the A340-500 opt's best $\sigma_{YY\text{-}Max\text{-}Top\text{-}Tens.}$-prediction model compared to the NIKE3D-FAA solution. The model has been trained by a CGF algorithm with architecture including one hidden layer with 10 neurons (17-10-1). The ANN model's prediction error in terms of RMSE is lower than 10 (psi) for all data sets and the R^2 is 0.905 for independent testing and 0.954 for training. The low error and high R^2 for training and independent testing data affirm that the model is generalized well to predict unseen data not used in developing the model.

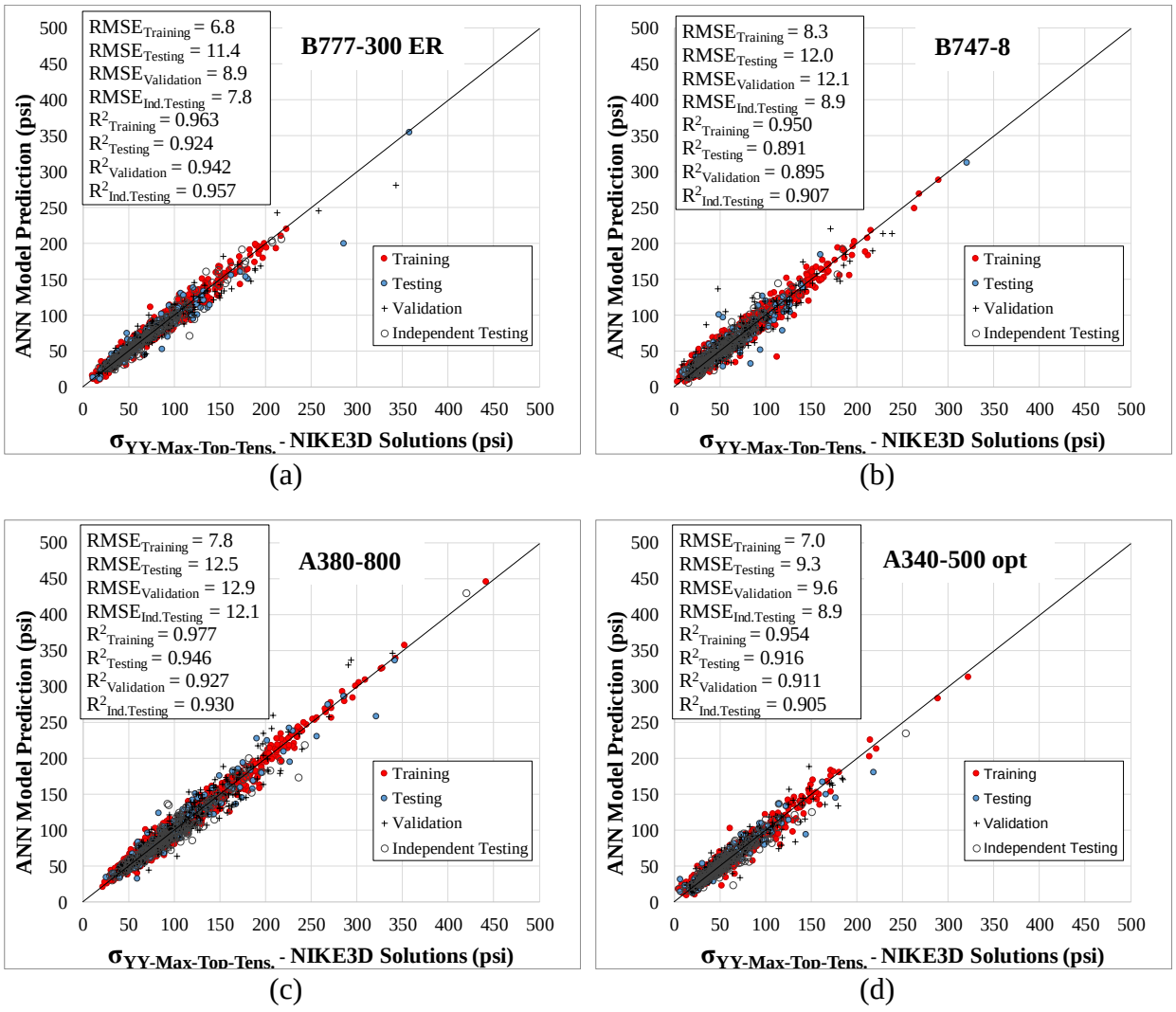

Figure 4.2 *NIKE3D FEM solution vs. ANN model prediction of the σYY-Max-Top-Tens. for (a) B777-300 ER (b) B747-8 (c) A380-800 (d) A340-500 opt mechanical loading only.*

Maximum Principal tensile stress ($\sigma_{1\text{-}Max\text{-}Top\text{-}Tens.}$)

In this study ANN models have been developed for predicting both principal stress and tensile stresses in *x* and *y* directions. Figure 4.3 present the prediction performance of the principal stress-prediction ANN models for the four types of aircraft. Figure 4.3 (a), (b), (c), and (d) show that the σ_1-prediction ANN models developed for different types of aircraft can accurately replicate the NIKE3D-FAA FE solutions, and can help in obtaining one of the

most important responses corresponding to top-down cracking in concrete pavements using ANN models.

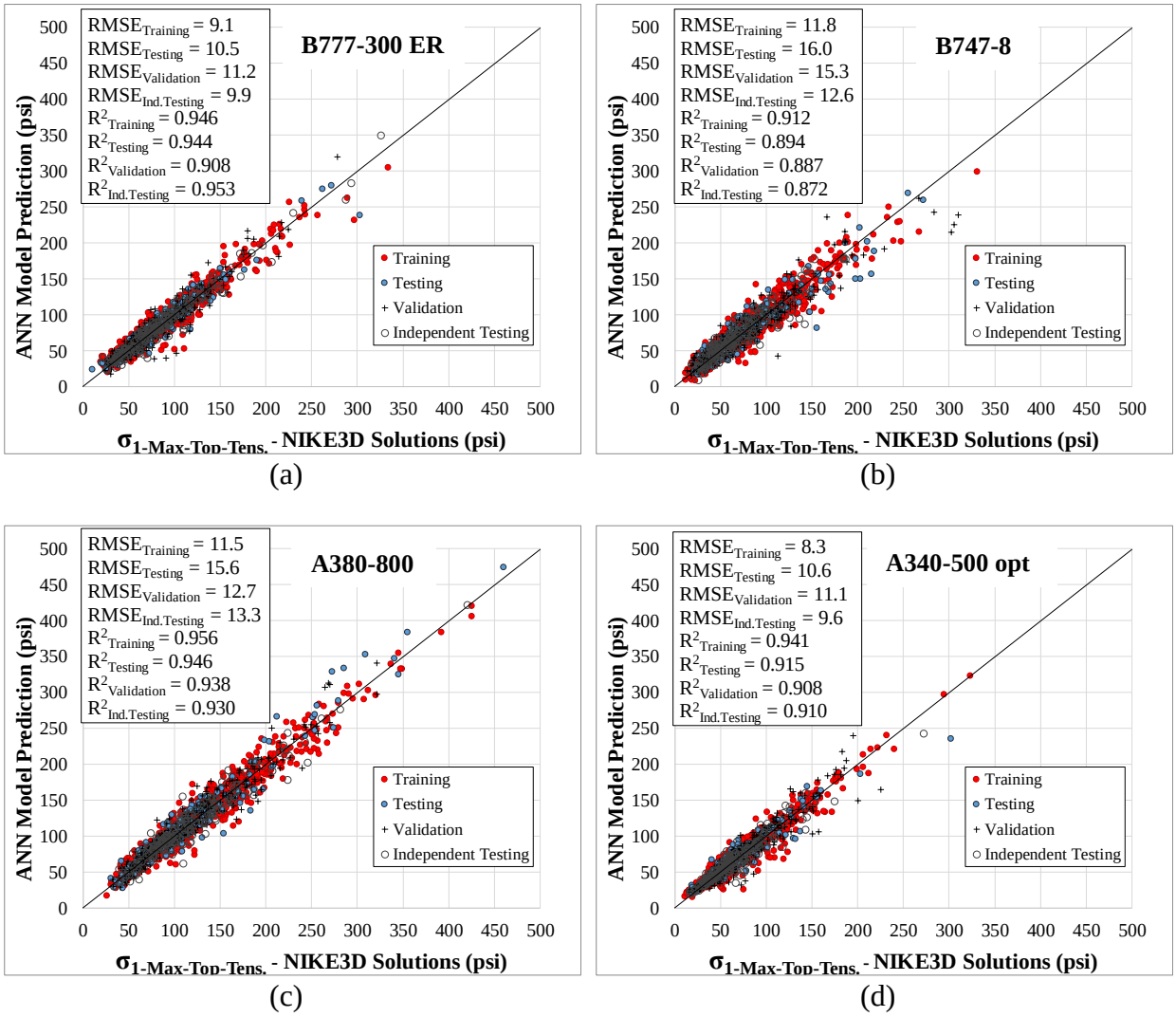

Figure 4.3 *NIKE3D FEM solution vs. ANN model prediction of the $\sigma_{1\text{-Max-Top-Tens.}}$ for (a) B777-300 ER (b) B747-8 (c) A380-800 (d) A340-500 opt mechanical loading only.*

Simultaneous Mechanical and Temperature Loading

Figures 4.4 through 4.6 compare ANN model predictions to NIKE3D-FAA FEM solutions under simultaneous mechanical and temperature loading for four aircraft (B777-300 ER, B747-8, A380-800, and A340-500 opt). The models predict maximum σ_{XX}, σ_{YY}, and σ_1 at the top of the PCC slab.

Maximum Top Tensile Stress in X-Direction ($\sigma_{XX\text{-}Max\text{-}Top\text{-}Tens.}$)

Figure 4.4 represents $\sigma_{XX\text{-}Max\text{-}Top\text{-}Tens.}$-prediction model results compared with FE solutions when temperature loading is concurrently applied with mechanical loading. Comparing Figure 4.4 with Figure 4.1 shows that the maximum tensile stresses obtained at the top of the slab in the presence of temperature and mechanical loading is (600 psi), about two times greater than that when only mechanical loading is applied (300 psi).

Figure 4.4 (a) shows the B777-300 ER's $\sigma_{XX\text{-}Max\text{-}Top\text{-}Tens.}$-prediction model accuracy. As presented in Table 4.1, this model has 19-5-5-1 architecture and a CGF algorithm was used for training it. Moreover, the RMSE value for independent testing is 33 psi, almost 4 times more than the RMSE obtained for the $\sigma_{XX\text{-}Max\text{-}Top\text{-}Tens.}$-prediction ANN model under mechanical loading condition (8.3 psi). This difference is because applying temperature loading can create more nonlinearity and complexity and also a higher range of stresses, Figure 4.4 (a) exhibits high accuracy in terms of R^2 values of 0.951 and 0.925 for training and independent testing.

The B747-8's $\sigma_{XX\text{-}Max\text{-}Top\text{-}Tens.}$-prediction model performance is shown in Figure 4.4 (b). The figure displays that the model is predicting $\sigma_{XX\text{-}Max\text{-}Top\text{-}Tens.}$ with R^2 values of 0.940 and 0.929 and RMSE values of 29 and 32 psi for training and independent testing, respectively. Figure 4.4 (b) shows that higher tensile stresses have been predicted more accurately than lower tensile stresses. The higher stresses on top of the slab usually are associated with negative temperature gradient cases in which the slab is curled upward and the corner of the slab has higher deflection than other parts of the slab.

Figure 4.4 (c) represents the A380-800's $\sigma_{XX\text{-}Max\text{-}Top\text{-}Tens.}$-prediction model results compared to FE solutions. The figure shows that the ANN response model can predict the $\sigma_{XX\text{-}Max\text{-}Top\text{-}Tens.}$ under combined temperature and A380-800 mechanical loading with high accuracy (R^2 values of 0.951 and 0.925 for training and independent testing, respectively) without overfitting since the R^2 and RMSE of the training, testing, validation and independent testing are not much different.

Figure 4.4 (d) compares A340-500 opt's $\sigma_{XX\text{-}Max\text{-}Top\text{-}Tens.}$-prediction ANN model results with the FE solution. The results are for a model with 19-5-5-1 architecture trained by a CGF algorithm. R^2 and RMSE values are 0.943 and 29 psi for independent testing and 0.950 and 26 psi for training, respectively. Very close results between training and testing demonstrate that the model has been generalized well and has avoided overfitting. In summary, Figure 4.4 indicates that ANN models developed for different types of aircraft have promise for predicting the $\sigma_{XX\text{-}Max\text{-}Top\text{-}Tens.}$ even when temperature induced loading is present. In very few number of individual cases, there are some high order of errors. For instance, Figure 4.4 (c) shows an over predicted $\sigma_{XX\text{-}Max\text{-}Top\text{-}Tens.}$ for independent testing by 36%. To address this issue, training ANN models for positive and negative temperature gradient separately and increasing the data set size might help.

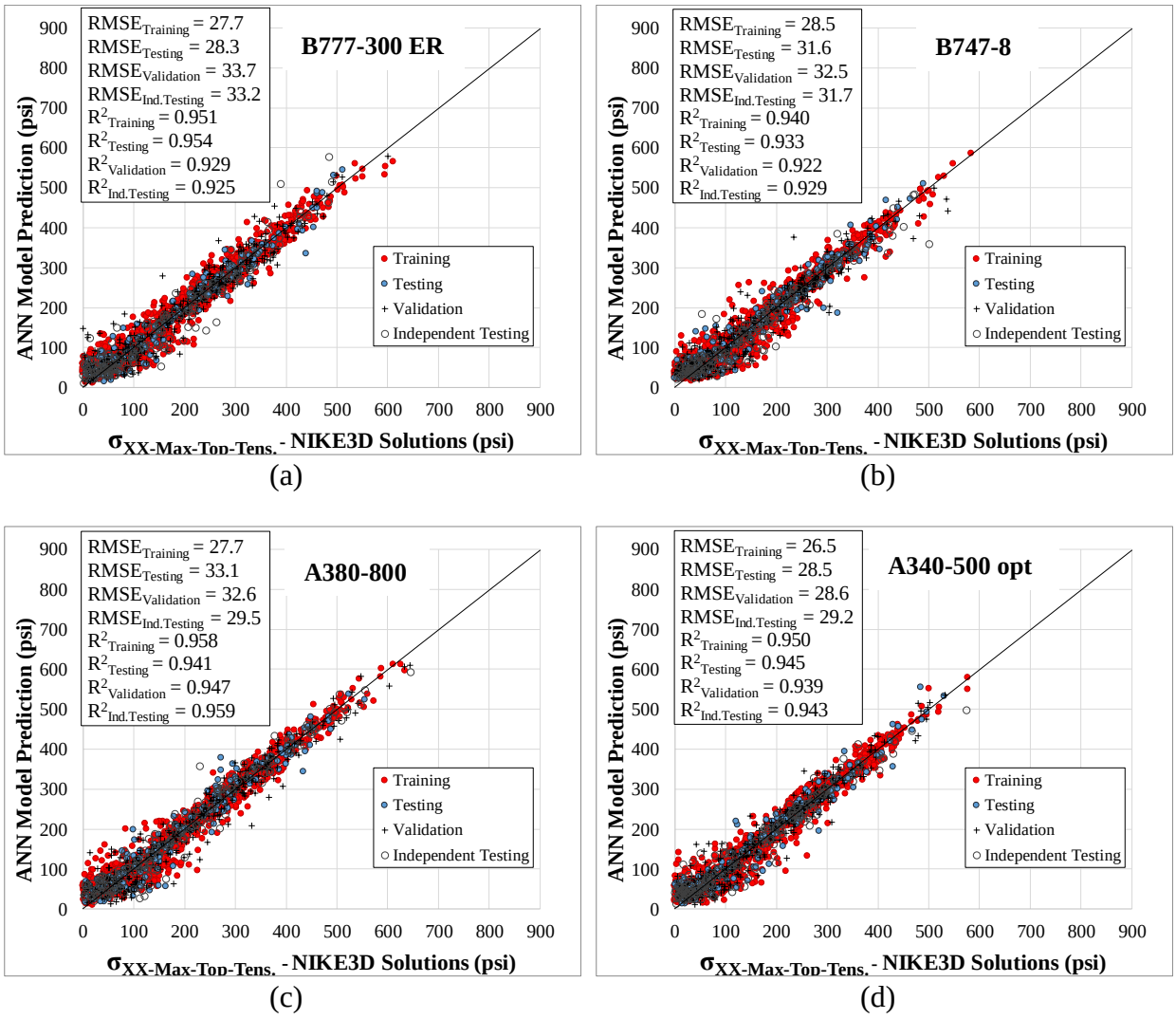

Figure 4.4 *NIKE3D FEM solution vs. ANN model prediction of the $\sigma_{XX\text{-}Max\text{-}Top\text{-}Tens.}$ for simultaneously (a) B777-300 ER (b) B747-8 (c) A380-800 (d) A340-500 opt mechanical loading and temperature induced loading.*

Maximum top tensile stress in Y-direction ($\sigma_{YY\text{-}Max\text{-}Top\text{-}Tens.}$)

Figure 4.5 is a comparison between ANN predictions and NIKE3D-FAA FEM solutions of the $\sigma_{YY\text{-}Max\text{-}Top\text{-}Tens.}$. The solution and the prediction results shown in Figure 4.5 are associated with pavement subjected to simultaneous temperature and B777-300 ER, B747-8, A380-800, and A340-500 opt's mechanical loading. Figure 4.5 (a) displays the prediction performance of the B777-300's $\sigma_{YY\text{-}Max\text{-}Top\text{-}Tens.}$–prediction ANN model with 19-5-5-1 architecture and trained by an OSS training algorithm. Figure 4.5 (a) shows that the

predictions accurately fit to values obtained by FE solutions. Also, in terms of R^2 and RMSE, it can be observed that the model adequately predicts top tensile stress. The R^2 values for training and independent testing are 0.950 and 0.916 and the RMSE for training and independent testing 28 and 35 psi, respectively.

Figure 4.5 (b) presents the performance of the B747-8's most accurate $\sigma_{YY\text{-}Max\text{-}Top\text{-}Tens.}$-prediction ANN model. As displayed in Figure 4.5 (b), a good fit between predicted tensile stress and FE solution can be observed. R^2 and RMSE values of 0.943 and 27 psi for training and 0.930 and 31 psi for independent testing reflect the promising performance of the model. The performance of the A380-800's $\sigma_{YY\text{-}Max\text{-}Top\text{-}Tens.}$-prediction model, with 19-5-5-1 architecture and trained by an LM algorithm, is depicted in Figure 4.5 (c).

Figure 4.5 (d) shows prediction results for the A340-500 opt's best $\sigma_{YY\text{-}Max\text{-}Top\text{-}Tens.}$-prediction model compared to the NIKE3D-FAA solution. The model has been trained by LM algorithm and has architecture with one hidden layer with 10 neurons (19-5-5-1). The ANN model's prediction error in terms of RMSE is lower than 30 psi for all data sets and has an R^2 value of 0.948 for independent testing and 0.950 for training. The low error and high R^2 along with achieving the same accuracy for training and independent testing datasets affirm that the model is generalized well and can predict from unseen data not used for developing the model.

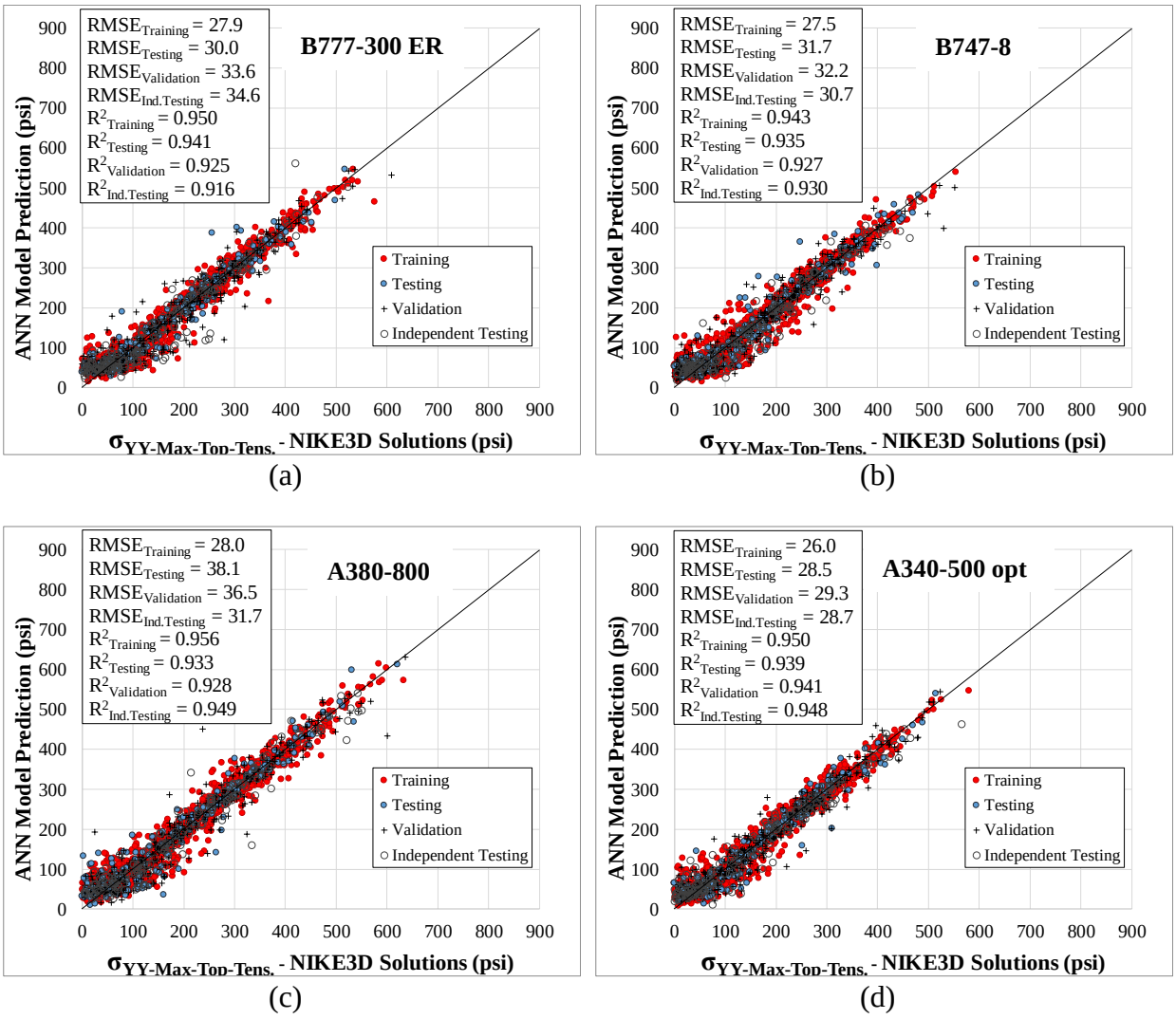

Figure 4.5 *NIKE3D FEM solution vs. ANN model prediction of the $\sigma_{YY\text{-}Max\text{-}Top\text{-}Tens.}$ for simultaneously (a) B777-300 ER (b) B747-8 (c) A380-800 (d) A340-500 opt mechanical loading and temperature induced loading.*

Maximum Principal tensile stress ($\sigma_{1\text{-}Max\text{-}Top\text{-}Tens.}$)

Figure 4.6 represents $\sigma_{1\text{-}Max\text{-}Top\text{-}Tens.}$-prediction models results compared with FE solutions when temperature loading is applied concurrently with mechanical loading. Comparing Figure 4.6 with Figure 4.3 shows that the maximum tensile principal stresses occurring on top of the slab when temperature and mechanical loading are simultaneously applied is (<700 psi), about two times more than the condition when mechanical loading only is applied (<350 psi).

Figure 4.6 (a) describes the B777-300 ER's $\sigma_{1\text{-}Max\text{-}Top\text{-}Tens.}$-prediction model accuracy. As presented in Table 4.1, this model has 19-5-5-1 architecture trained by CGP algorithm. Figure 4.6 (a) reflects high accuracy in terms of R^2 values of 0.941 and 0.919 for training and independent testing.

Figure 4.6 (b) shows that the B747-8's $\sigma_{1\text{-}Max\text{-}Top\text{-}Tens.}$-prediction ANN model results are accurately fitted to the NIKE3D-FAA FE solutions. The best model selected for B747-8's $\sigma_{1\text{-}Max\text{-}Top\text{-}Tens.}$-prediction has an architecture of 19-5-5-1 trained by a CGB algorithm (Table 4.1). It can also be observed that the model adequately predicts top tensile stress with R^2 accuracy values of 0.943 and 0.926 for training and independent testing.

Figure 4.6 (c) is a comparison between $\sigma_{1\text{-}Max\text{-}Top\text{-}Tens.}$-ANN predictions and NIKE3D-FAA FE solutions for A380-800. The $\sigma_{1\text{-}Max\text{-}Top\text{-}Tens.}$-ANN model is a two-hidden-layer network with 5 neurons in each layer and trained by an OSS algorithm. Figure 4.6 (c) shows that the model accuracy for predicting $\sigma_{1\text{-}Max\text{-}Top\text{-}Tens.}$ for training and independent testing in terms of R^2 is 0.953 and 0.947 with RMSE values of 30 and 33 psi, respectively.

The A340-500 opt's best $\sigma_{1\text{-}Max\text{-}Top\text{-}Tens.}$-ANN model prediction results compared to the NIKE3D-FAA solution are represented in Figure 4.6 (d). The model has an architecture of with two hidden layers and was trained by a CGF algorithm with 5 neurons (19-5-5-1). The ANN model's prediction error in terms of RMSE is lower than 32 psi for all datasets and the R^2 value is 0.935 for independent testing and 0.949 for training.

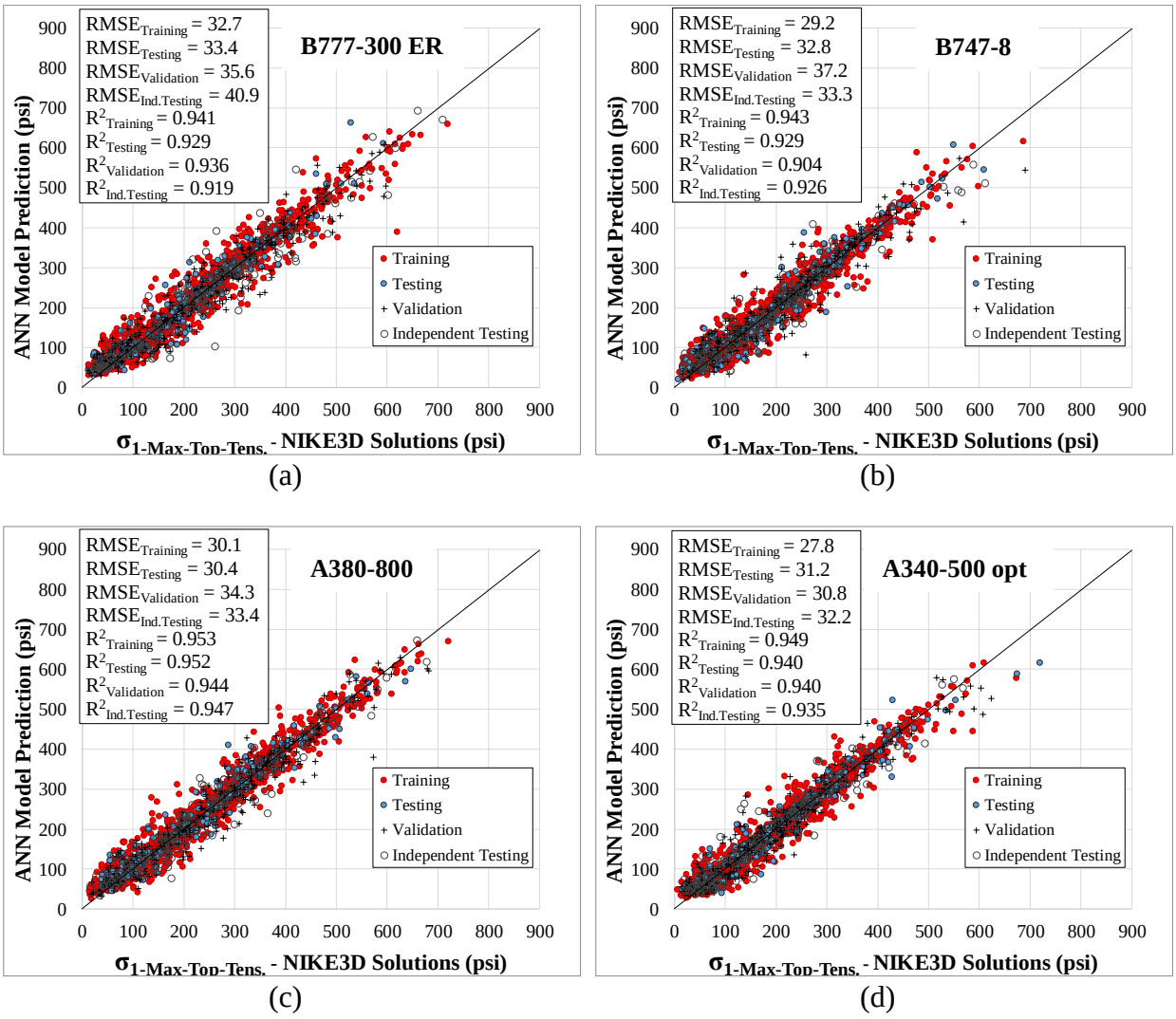

Figure 4.6 *NIKE3D FEM solution vs. ANN model prediction of the $\sigma_{1\text{-}Max\text{-}Top\text{-}Tens.}$ for simultaneously (a) B777-300 ER (b) B747-8 (c) A380-800 (d) A340-500 opt mechanical loading and temperature induced loading.*

In this section ANN model predictions have been provided and compared with the NIKE3D-FAA FE solutions. The results for four types of heavy and new generation aircraft show that ANN models can reasonably replicate critical tensile stresses corresponding to top-down cracking in rigid airfield pavements under both environmental and mechanical loading conditions. In the next section sensitivity approaches for verifying and testing the ANN models are discussed.

Sensitivity assessments of the ANN Models

Sensitivity of the ANN models prediction were tested by using a new data set. Sensitivity analysis testing was limited to two aircraft (B777-300 ER and B787-8) and seven input variables: PCC thickness, base thickness, subbase thickness, PCC modulus, subgrade modulus, temperature gradient, and coefficient of thermal expansion. Sensitivity was evaluated for aircraft-only and combined temperature/aircraft loads. Sensitivity was evaluated for all ANN models trained for each response and each aircraft, and the best model (based on accuracy obtained by the sensitivity test) is presented. Tables 4.2 and 4.3 present the architecture, the training algorithm, and the performance of the highest-accuracy ANN model from the sensitivity analysis testing.

Table 4.2 *ANN model prediction performance for mechanical-loading-only case.*

Training Algorithm	**Accuracy Criteria**	**B777-300 ER**			**B787-8**		
		σ_{XX}-Max-Top-Tens.	***σ_{YY}- Max-Top-Tens.***	***σ_{1}- Max-Top-Tens.***	***σ_{XX}-Max-Top-Tens.***	***σ_{YY}- Max-Top-Tens.***	***σ_{1}- Max-Top-Tens.***
LM	Architecture	17-25-1	17-25-25-1	17-15-15-1	17-10-1	17-25-25-1	17-45-1
	R^2	0.948	0.981	0.973	0.937	0.960	0.881
	AAE (psi)	3.3	2.9	3.9	3.1	2.9	4.7
	RMSE (psi)	5.5	3.7	4.5	4.4	3.6	6.3
CGB	Architecture	17-40-1	17-30-30-1	17-10-10-1	17-5-5-1	17-45-1	17-50-50-1
	R^2	0.958	0.975	0.977	0.958	0.955	0.905
	AAE (psi)	4.1	3.4	2.9	2.8	3.1	4.6
	RMSE (psi)	5.0	4.3	4.2	3.6	3.8	5.7
CGF	Architecture	17-15-15-1	17-25-1	17-10-1	17-30-30-1	17-20-1	17-40-40-1
	R^2	0.963	0.968	0.978	0.931	0.957	0.883
	AAE (psi)	3.8	3.5	3.1	3.4	2.7	4.4
	RMSE (psi)	4.7	4.8	4.1	4.7	3.7	6.3
CGP	Architecture	17-5-5-1	17-10-1	17-20-1	17-30-30-1	17-25-1	17-25-1
	R^2	0.957	0.961	0.985	0.942	0.963	0.871
	AAE (psi)	3.7	3.9	2.5	2.6	2.7	5.7
	RMSE (psi)	5.0	5.3	3.4	4.3	3.4	6.6
OSS	Architecture	17-10-10-1	17-5-5-1	17-10-10-1	17-30-30-1	17-25-1	17-30-30-1
	R^2	0.956	0.972	0.987	0.951	0.960	0.862
	AAE (psi)	3.6	3.3	2.5	3.3	2.5	4.7
	RMSE (psi)	5.1	4.6	3.2	3.9	3.5	6.8
Model With Minimum RMSE		CGF	LM	OSS	CGB	CGP	CGB
		17-15-15-1	17-25-25-1	17-10-10-1	17-5-5-1	17-25-1	17-50-50-1

Table 4.3 *ANN model prediction performance for combined temperature and mechanical loading case.*

Training Algorithm	Accuracy Criteria	B777-300 ER			B787-8		
		$\sigma_{XX\text{-}Max\text{-}Top\text{-}Tens.}$	$\sigma_{YY\text{-}Max\text{-}Top\text{-}Tens.}$	$\sigma_{1\text{-}Max\text{-}Top\text{-}Tens.}$	$\sigma_{XX\text{-}Max\text{-}Top\text{-}Tens.}$	$\sigma_{YY\text{-}Max\text{-}Top\text{-}Tens.}$	$\sigma_{1\text{-}Max\text{-}Top\text{-}Tens.}$
LM	Architecture	19-5-5-1	19-15-1	19-15-15-1	19-5-5-1	19-5-5-1	19-15-1
	R^2	0.850	0.905	0.839	0.917	0.902	0.653
	AAE (psi)	8.7	8.1	9.5	5.5	5.8	13.6
	RMSE (psi)	12.1	10.9	13.7	7.5	8.2	15.5
CGB	Architecture	19-35-1	19-40-1	19-30-1	19-5-5-1	19-5-5-1	19-30-30-1
	R^2	0.885	0.940	0.896	0.898	0.915	0.799
	AAE (psi)	7.7	6.6	8.6	5.9	4.8	9.0
	RMSE (psi)	10.6	8.7	11.0	8.3	7.6	11.8
CGF	Architecture	19-20-20-1	19-20-20-1	19-35-35-1	19-10-10-1	19-35-35-1	19-45-1
	R^2	0.868	0.917	0.884	0.929	0.919	0.680
	AAE (psi)	8.8	7.9	8.8	5.2	5.4	12.1
	RMSE (psi)	11.4	10.2	11.6	6.9	7.4	14.9
CGP	Architecture	19-35-35-1	19-10-10-1	19-15-15-1	19-5-5-1	19-5-5-1	19-10-1
	R^2	0.865	0.960	0.881	0.917	0.907	0.804
	AAE (psi)	9.2	5.6	9.1	5.7	6.1	8.1
	RMSE (psi)	11.5	7.1	11.8	7.5	7.9	11.6
OSS	Architecture	19-5-5-1	19-10-1	19-20-1	19-5-5-1	19-5-5-1	19-30-1
	R^2	0.864	0.925	0.915	0.924	0.920	0.815
	AAE (psi)	6.7	8.2	7.1	5.5	5.4	8.8
	RMSE (psi)	11.6	9.7	9.9	7.2	7.4	11.3
Model With Minimum RMSE		CGB	CGP	OSS	CGF	OSS	OSS
		19-35-1	19-10-10-1	19-20-1	19-10-10-1	19-5-5-1	19-30-1

Effect of PCC slab Thickness on the Predicted Responses

Mechanical Loading Only

Figure 4.7 depicts variation of the critical responses from NIKE3D-FAA and the ANN response model. Figure 4.7 (a) shows that $\sigma_{XX\text{-}Max\text{-}Top\text{-}Tens.}$ decreases while the slab thickness increases for both gear types. Also $\sigma_{XX\text{-}Max\text{-}Top\text{-}Tens.}$ exhibits lower values for the four-wheel type gear of the B787 than for the six-wheel gear type of the B777-300 ER.

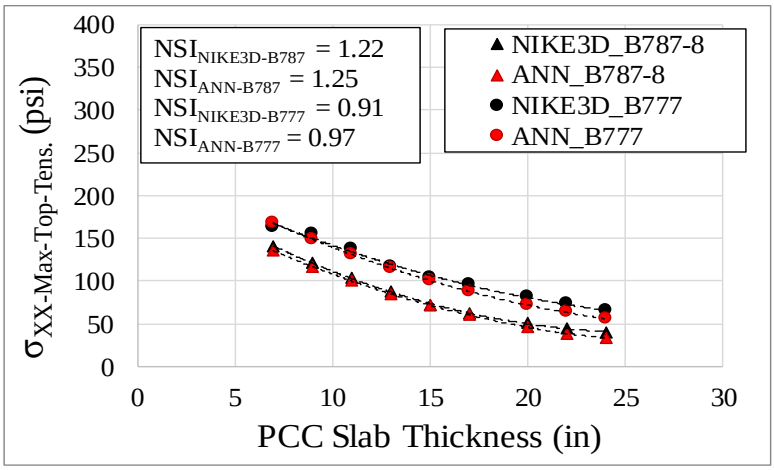

(a)

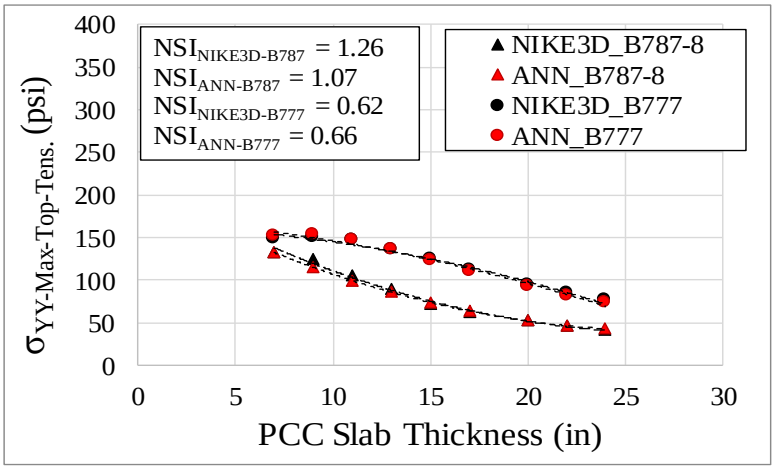

(b)

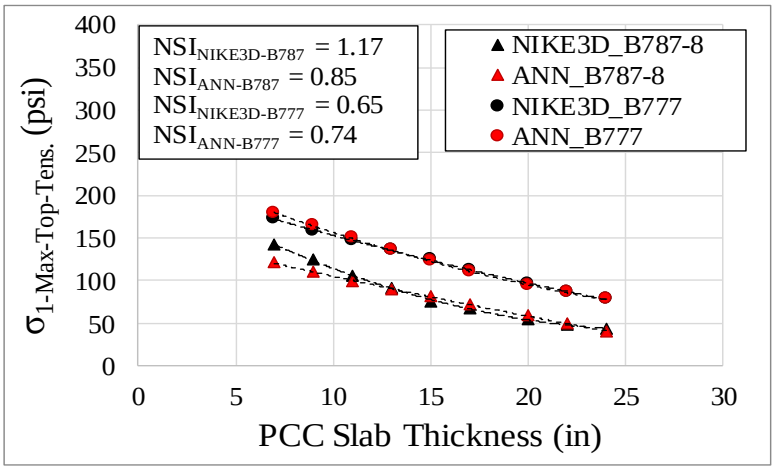

(c)

Figure 4.7 *Variation of the critical responses (a) σXX-Max-Top-Tens. (b) σYY-Max-Top-Tens. (c) σ1-Max-Top-Tens., obtained by NIKE3D-FAA solutions and ANN response model predictions vs. PCC slab thickness changes under mechanical loading only.*

Figure 4.7 demonstrates similar trends in stress response due to variation of the slab thickness. NSI is reasonably close for both aircraft analyses. Figure 4.7 (c) for $\sigma_{1\text{-}Max\text{-}Top\text{-}Tens.}$ shows worse agreement and more deviation of the ANN prediction from the direct 3D FEM solution, than either $\sigma_{XX\text{-}Max\text{-}Top\text{-}Tens.}$ or $\sigma_{YY\text{-}Max\text{-}Top\text{-}Tens.}$. Highest deviation obtained for the B787 and low slab thickness.

Simultaneous Mechanical and Temperature Loading

Figure 4.8 shows the effects of increasing PCC slab thickness on the predicted critical stresses and the NIKE3D-FAA solutions for slab thicknesses values from 7 to 24 in while the B787-8 or B777-300 ER gear load is located on the slab with temperature loading applied. Since there is temperature loading, nonlinear variation of the critical stresses to the PCC slab thickness changes can be observed in the figure.

Based on the NSI values in Figure 4.8, it can be concluded that sensitivity of the $\sigma_{1\text{-}Max\text{-}Top\text{-}Ten}$ to the slab thickness is higher than the sensitivity of the $\sigma_{XX\text{-}Max\text{-}Top\text{-}Tens.}$ and $\sigma_{YY\text{-}Max\text{-}Top\text{-}Tens.}$ to the slab thickness for B787-8, although the sensitivity of all three critical responses are the same to that of PCC slab thickness for B777-300 ER. In Figure 4.8 (a) it can be observed that the ANN response models can predict the $\sigma_{XX\text{-}Max\text{-}Top\text{-}Tens.}$. But, for B 777, the NIKE3D trend is linear, while the ANN model trend is curved downward for the cases with very low or very high slab thicknesses. This might be an overfitting issue of the ANN model. The model developed for combined loading condition uses both negative and positive temperature gradient in dataset. For sensitivity analysis, only negative gradient was tested. Separate ANN models would have been developed for both positive and negative temperature gradient cases to avoid this problem.

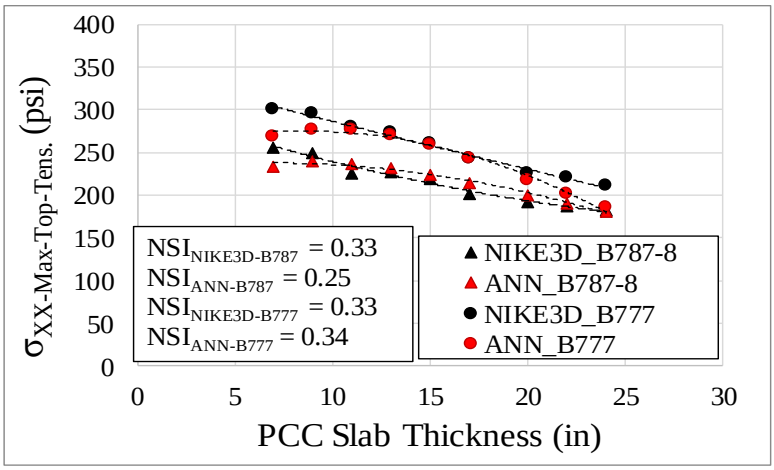

(a)

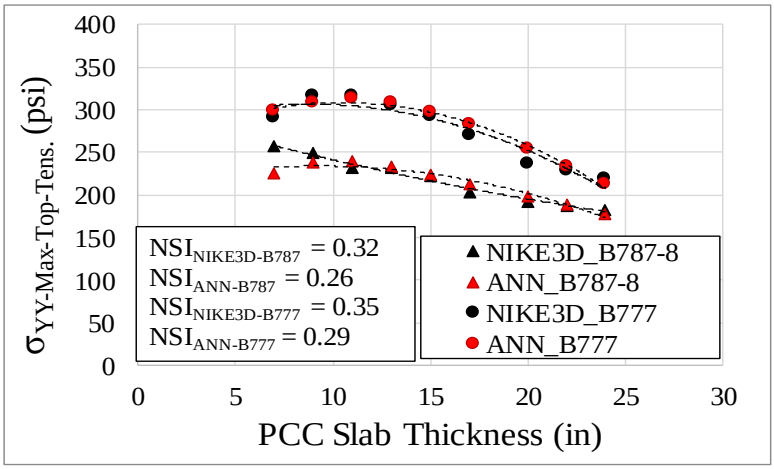

(b)

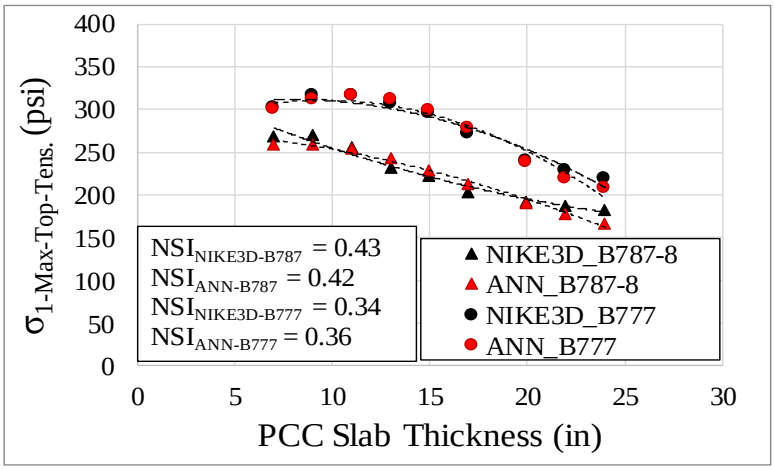

(c)

Figure 4.8 *Variation of the critical responses (a) $\sigma_{XX\text{-}Max\text{-}Top\text{-}Tens.}$ (b) $\sigma_{YY\text{-}Max\text{-}Top\text{-}Tens.}$ (c) $\sigma_{1\text{-}Max\text{-}Top\text{-}Tens.}$, obtained by NIKE3D-FAA solutions and ANN response model predictions vs. PCC slab thickness changes under simultaneous mechanical and temperature loading.*

Figure 4.8 (b) shows that $\sigma_{YY\text{-}Max\text{-}Top\text{-}Tens.}$ predicted values are very close to the NIKE3D-FAA solutions, and the sensitivity of this stress to slab thickness is well-predicted for both aircraft. Figure 4.8 (c) shows that the trend of the $\sigma_{1\text{-}Max\text{-}Top\text{-}Tens.}$ changes to the slab thickness are very well predicted for both aircraft, so the NSI values for ANN prediction (NSI=0.42 and 0.36 for B787-8 and B777-300 ER) and FE solution (NSI=0.43 and 0.34 for B787-8 and B777-300 ER) are very close.

Effect of Base Layer Thickness on the Predicted Responses

Mechanical Loading Only

Sensitivity evaluation of ANN model prediction to base layer thickness changes are illustrated in Figure 4.9. Figure 4.9 presents sensitivity analysis results for base-layer thickness values varying from 5 to 30 in while other inputs are kept constant and the B787-8 load and the B777-300 ER load are applied. Overall, looking at these figures shows that the sensitivity of the critical responses to the base layer thickness are close for both aircraft. It can also be seen that the ANN response models can predict the effect of increasing base layer thickness very well. Figure 4.9 also shows that ANN models provide very accurate prediction for B787-8 and B777-300 ER loading, with the sensitivity and the exact value of the critical response predictions almost the same as the NIKE-3D FAA solutions in both x, y, and principal directions.

Figure 4.9 (a) shows that the NSI_{NIKE3D} of the slab thickness for $\sigma_{XX\text{-}Max\text{-}Top\text{-}Tens.}$ are 0.56 and 0.51 for the B787-8 and B777-300 ER, respectively, and the ANN prediction shows NSI values of 0.67 and 0.61 for B787-8 and B777-300 ER, respectively.

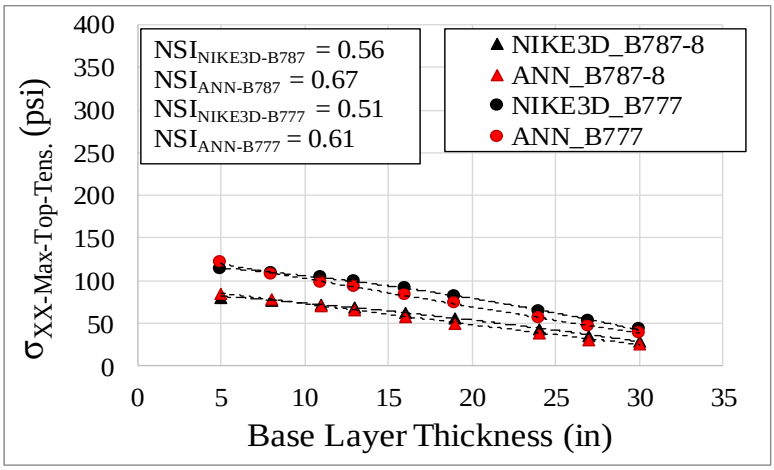

(a)

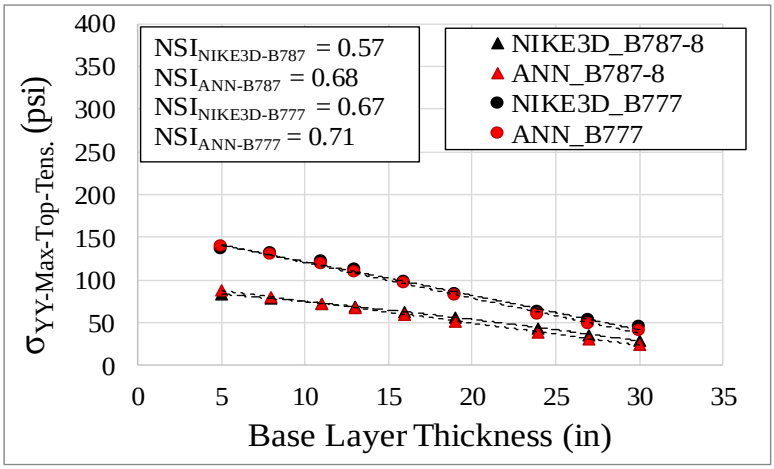

(b)

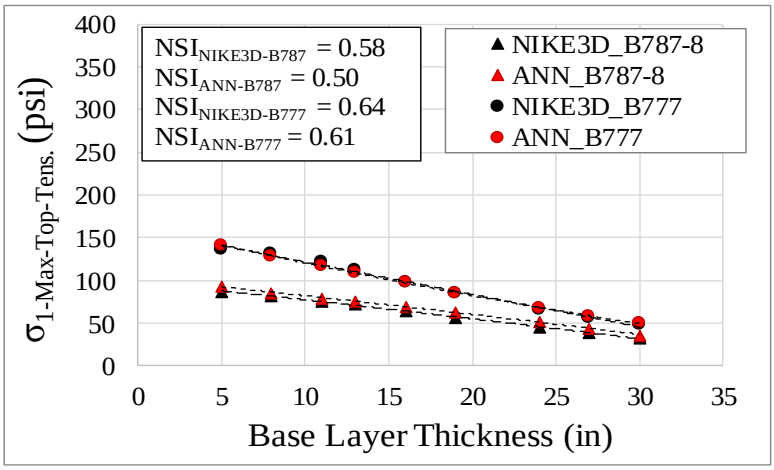

(c)

Figure 4.9 *Variation of the critical responses (a) $\sigma_{XX\text{-}Max\text{-}Top\text{-}Tens.}$ (b) $\sigma_{YY\text{-}Max\text{-}Top\text{-}Tens.}$ (c) $\sigma_{1\text{-}Max\text{-}Top\text{-}Tens.}$, obtained by NIKE3D-FAA solutions and ANN response model predictions vs. base layer thickness changes under mechanical loading only.*

Figure 4.9 (b) and Figure 4.9 (c) also display the sensitivity of the FE solution and predicted $\sigma_{YY\text{-}Max\text{-}Top\text{-}Tens.}$ and $\sigma_{1\text{-}Max\text{-}Top\text{-}Tens.}$ to base-layer thickness changes. These results show that the sensitivity obtained by FE solution and ANN prediction are close, especially with respect to the principal stress, with NSI_{ANN} values for predicted $\sigma_{YY\text{-}Max\text{-}Top\text{-}Tens.}$ of 0.68 and 0.71 for B787-8 and B777-300 and for NSI_{NIKE3D} 0.57 and 0.6 for B787-8 and B777-300, respectively. The NSI_{ANN} for $\sigma_{1\text{-}Max\text{-}Top\text{-}Tens.}$ is 0.50 and 0.61 and NSI_{NIKE3D} is 0.58 and 0.64 for B787-8 and B777-300, respectively. The results affirm that ANN model predictions are as sensitive as NIKE3D-FAA solutions to base-layer thickness.

Simultaneous Mechanical and Temperature Loading

Figure 4.10 presents sensitivity evaluation of the ANN model prediction with respect to base-layer thickness changes when temperature loading is simultaneously applied with mechanical loading. These figures show that, as for the mechanical loading condition, ANN critical response prediction models can predict stresses when the base layer thickness is changing with the same trend as the FE solution. Comparing Figure 4.10 and Figure 4.9 reveals that the sensitivity of the critical top tensile stresses to the base layer thickness is much higher for the mechanical-loading-only case than for combined temperature and mechanical loading. In the presence of the temperature load, the thermal properties of the slab (temperature gradient and thermal coefficient) affect the tensile stresses, and base and sub-base layer properties have less effect on the stresses.

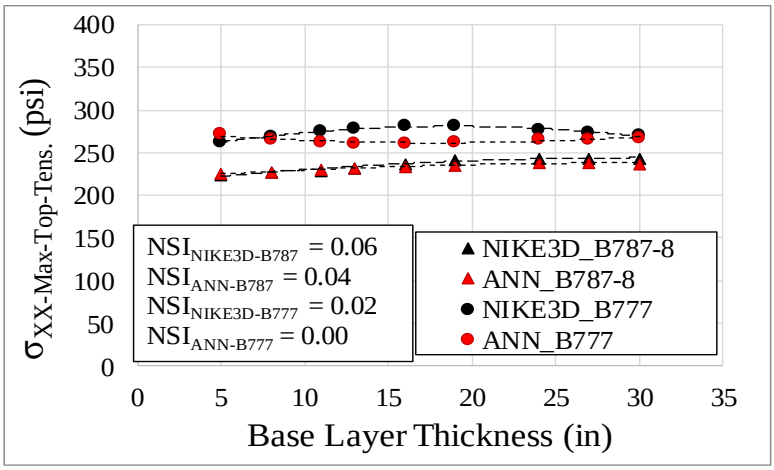

(a)

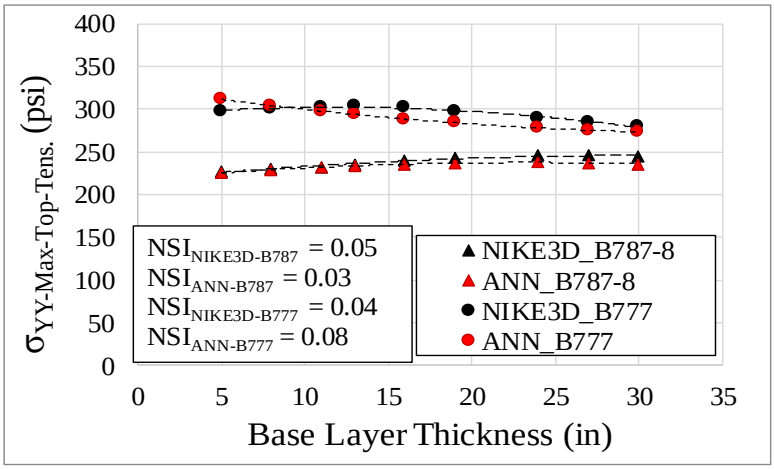

(b)

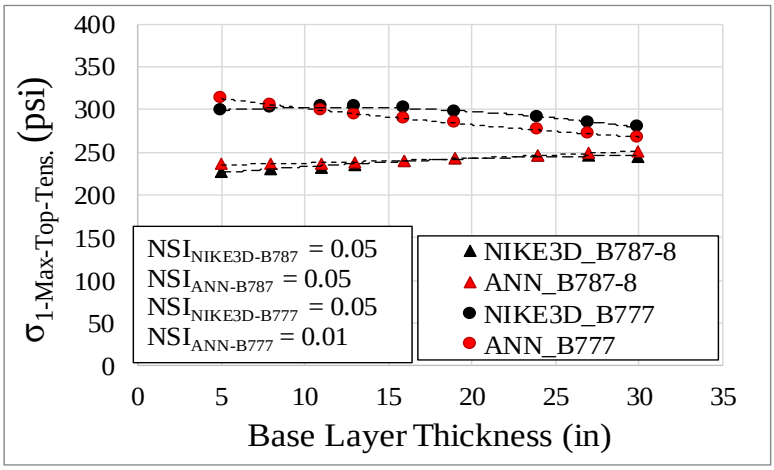

(c)

Figure 4.10 *Variation of the critical responses (a) $\sigma_{XX\text{-}Max\text{-}Top\text{-}Tens.}$ (b) $\sigma_{YY\text{-}Max\text{-}Top\text{-}Tens.}$ (c) $\sigma_{1\text{-}Max\text{-}Top\text{-}Tens.}$, obtained by NIKE3D-FAA solutions and ANN response model predictions vs. base layer thickness changes under simultaneous mechanical and temperature loading.*

Effect of PCC slab Modulus on the Predicted Responses

Mechanical Loading Only

The sensitivity of tensile stresses to PCC slab modulus variation is illustrated in Figure 4.11 for the mechanical-loading-only case. As seen in Figure 4.11, the response prediction models can replicate the NIKE3D-FAA FE solution so that the sensitivity of the tensile stresses in *x* and *y* direction and the principal stress to the PCC slab modulus changes for the ANN prediction and the FE solution are very close. As Figure 4.11 (a) shows, the $NSI_{B787\text{-}8}$ values are 0.27 and 0.28 for the NIKE3D-FAA solution and the ANN prediction, respectively. Figure 4.11 (b) also shows that NSI_{B777} is 0.44 and 0.49 for the NIKE3D-FAA solution and the ANN prediction, respectively. Furthermore, Figure 4.11 (c) shows that both the $\sigma_{1\text{-}Max\text{-}Top\text{-}Tens.}$ prediction and the $\sigma_{1\text{-}Max\text{-}Top\text{-}Tens.}$ FE solution have similar sensitivity to the PCC slab modulus, with $NSI_{B787\text{-}8}$ values of 0.35 and 0.35 and NSI_{B777} values of 0.45 and 0.48 for NIKE3D-FAA solutions and ANN predictions, respectively. The close sensitivity index obtained for the prediction and the actual solution represents the fact that response models seem promising in predicting critical stresses and their variation in behavior when the input parameters are only slightly changing.

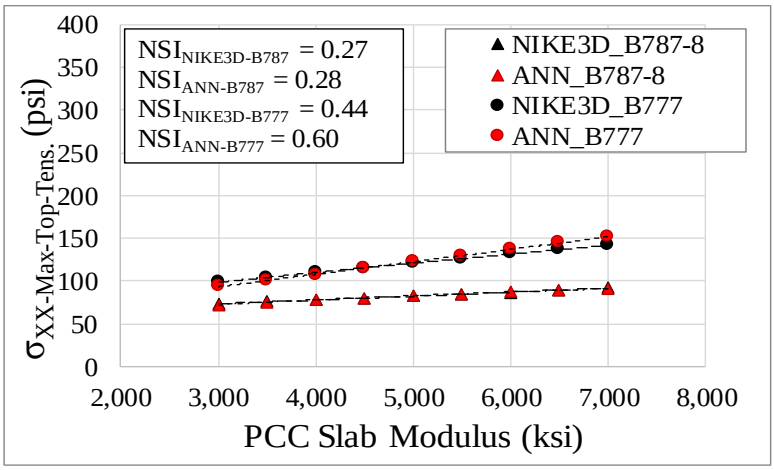

(a)

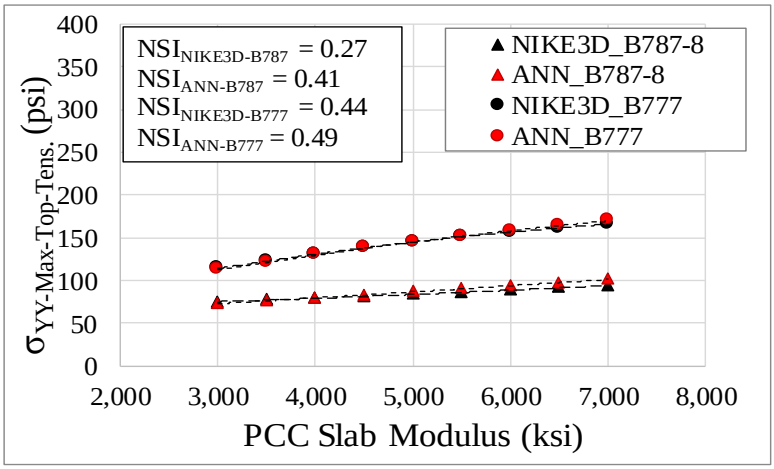

(b)

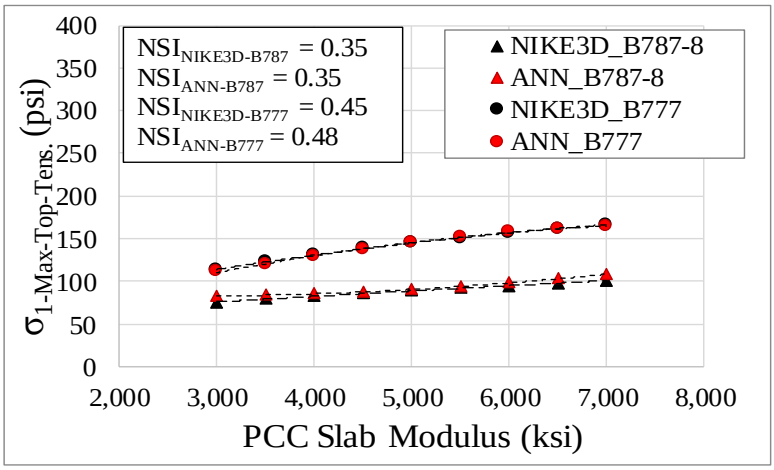

(c)

Figure 4.11 *Variation of the critical responses (a) $\sigma_{XX\text{-}Max\text{-}Top\text{-}Tens.}$ (b) $\sigma_{YY\text{-}Max\text{-}Top\text{-}Tens.}$ (c) $\sigma_{1\text{-}Max\text{-}Top\text{-}Tens.}$, obtained by NIKE3D-FAA solutions and ANN response model predictions vs. PCC slab modulus changes under mechanical loading only.*

Simultaneous Mechanical and Temperature Loading

Figure 4.12 and Figure 4.11 show that ANN critical response models provide similar sensitivity as the actual solutions to the PCC slab modulus even when there is temperature loading. As Figure 4.12 (a) shows, the $NSI_{B787\text{-}8}$ value is 0.47 and 0.51 for the NIKE3D-FAA solution and the ANN prediction, respectively. Figure 4.12 (b) also shows that NSI_{B777} is 0.49 and 0.37 for the NIKE3D-FAA solution and the ANN prediction, respectively, and Figure 4.12 (c) shows that $NSI_{B787\text{-}8}$ is 0.47 and 0.56 and NSI_{B777} is 0.51 and 0.44 for the NIKE3D-FAA solution and the ANN prediction, respectively.

Effect of Subgrade Modulus on the Predicted Responses

Mechanical Loading Only

Figure 4.13 and Figure 4.14 present the sensitivity of the tensile stresses obtained by the NIKE3D-FAA solution and the ANN response models to the subgrade modulus as it varies from 3,000 to 50,000 psi while other inputs are kept constant for B787-8 and B777-300 ER loading. These figures show that the sensitivity of the different stress responses are very close for both the NIKE-3D results and the ANN response model prediction. Figure 4.13 and Figure 4.14 show that the tensile stresses are more sensitive to the subgrade modulus change under B777-300 ER loading than under B787-8 loading. It can also be observed that the NSI values obtained by B777-300 ER's ANN response models are closer to the NIKE3D-FAA solution than the B787-8's models. As Figure 4.13 (a) shows, NSI_{B777} is 0.5 and 0.60, respectively for the NIKE3D solution and the ANN prediction, and NSI_{B787} is 0.41 and 0.28.

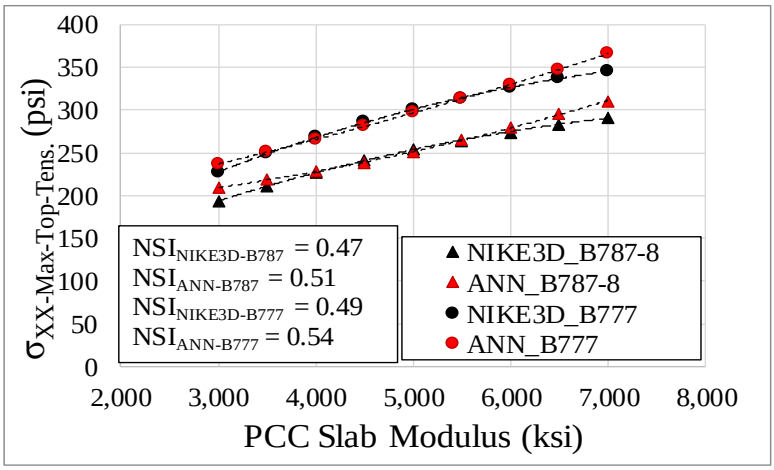

(a)

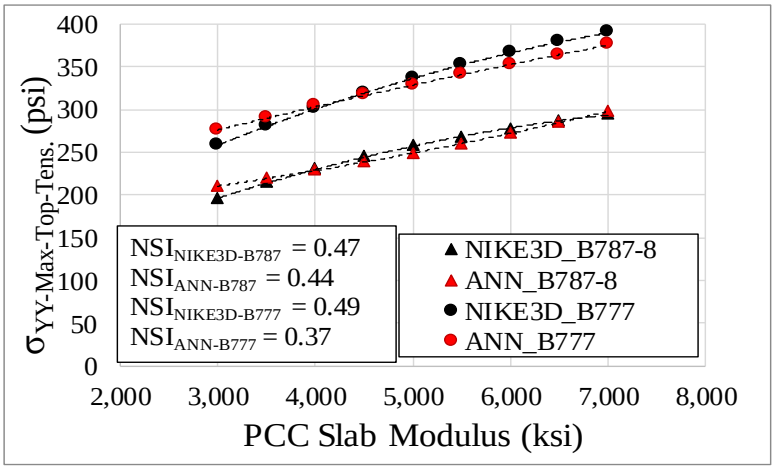

(b)

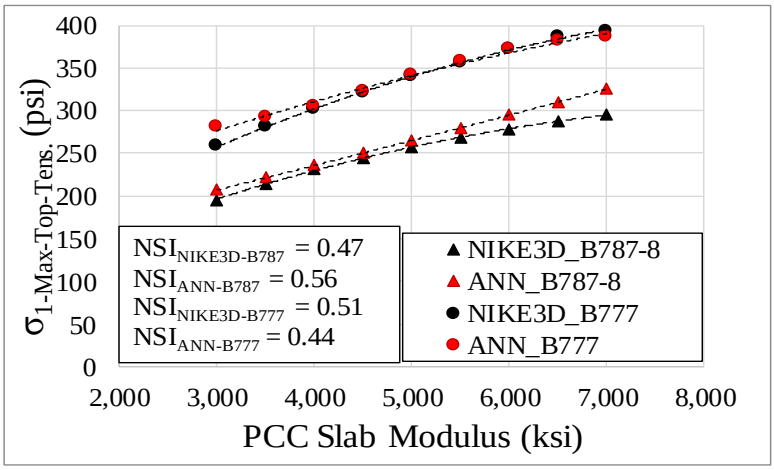

(c)

Figure 4.12 *Variation of the critical responses (a) $\sigma_{XX\text{-}Max\text{-}Top\text{-}Tens.}$ (b) $\sigma_{YY\text{-}Max\text{-}Top\text{-}Tens.}$ (c) $\sigma_{1\text{-}Max\text{-}Top\text{-}Tens.}$, obtained by NIKE3D-FAA solutions and ANN response model predictions vs. PCC slab modulus changes under simultaneous mechanical and temperature loading.*

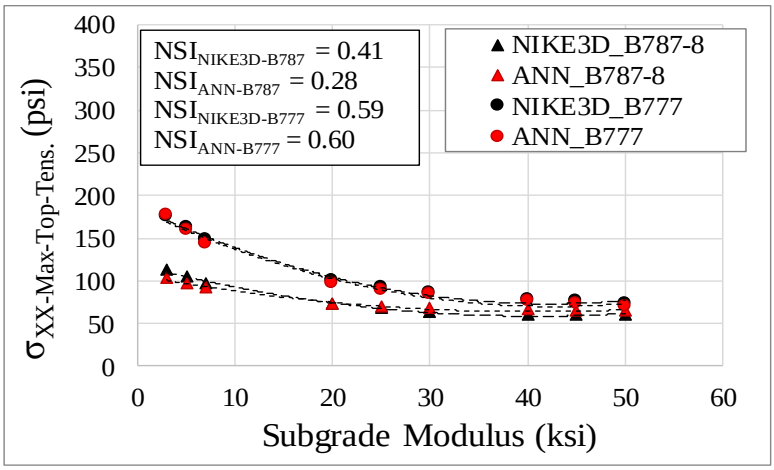

(a)

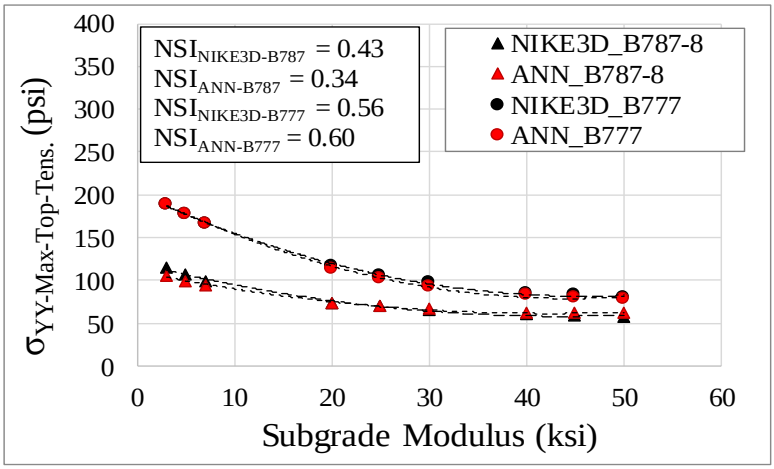

(b)

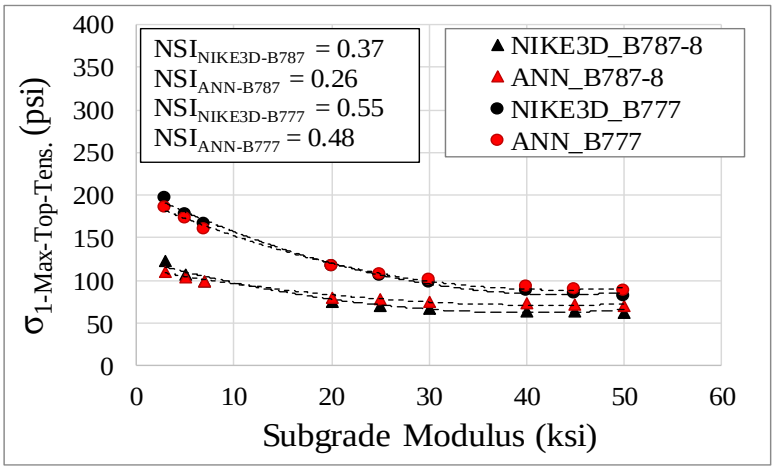

(c)

Figure 4.13 *Variation of the critical responses (a) $\sigma_{XX\text{-}Max\text{-}Top\text{-}Tens.}$ (b) $\sigma_{YY\text{-}Max\text{-}Top\text{-}Tens.}$ (c) $\sigma_{1\text{-}Max\text{-}Top\text{-}Tens.}$, obtained by NIKE3D-FAA solutions and ANN response model predictions vs. subgrade modulus changes under mechanical loading only.*

Simultaneous Mechanical and Temperature Loading

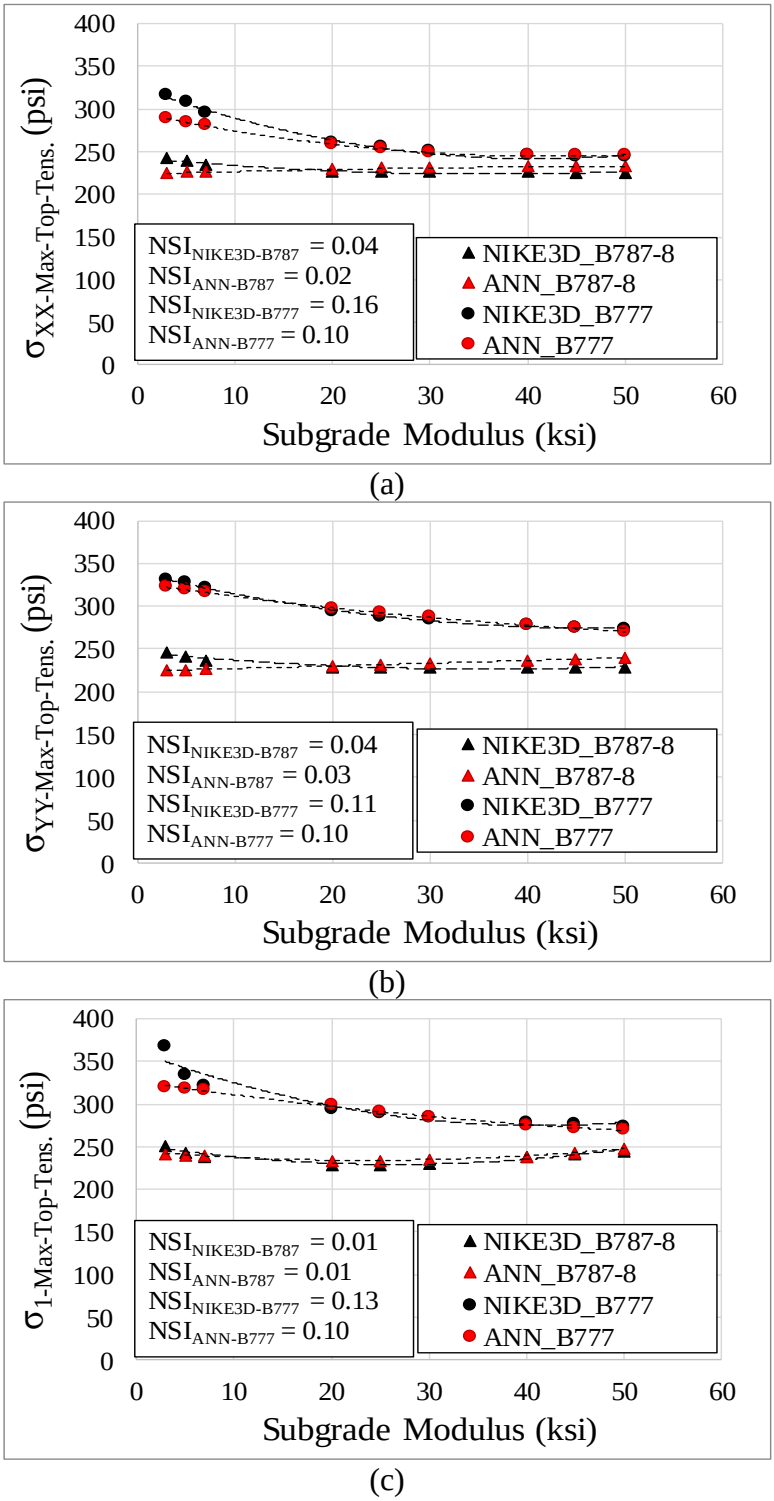

Figure 4.14 *Variation of the critical responses (a) $\sigma_{XX\text{-}Max\text{-}Top\text{-}Tens.}$ (b) $\sigma_{YY\text{-}Max\text{-}Top\text{-}Tens.}$ (c) $\sigma_{1\text{-}Max\text{-}Top\text{-}Tens.}$, obtained by NIKE3D-FAA solutions and ANN response model predictions vs. subgrade modulus changes under simultaneous mechanical and temperature loading.*

Effect of Temperature Gradient on the Predicted Responses

Sensitivity evaluation of the ANN model predictions to the slab's temperature gradient changes is shown in Figure 4.15. The figure presents the sensitivity analysis results for temperature gradient values varying from -0.3 to -1.9 F/in while other inputs are kept constant and the B787-8 load and the B777-300 ER load are applied. Overall, these figures show that the sensitivities of the critical responses to the temperature gradient are very close for both aircraft. It can also be seen that the ANN response models can predict the effect of increasing temperature gradient very well.

Figure 4.15 (a) shows that the NSI_{NIKE3D} is 0.48 and 0.39 for the B787-8 and B777-300 ER, respectively, and the ANN prediction produces an NSI value of 0.44 and 0.37 for B787-8 and B777-300 ER, respectively. Figure 4.15 (b) and Figure 4.15 (c) also display the sensitivity of the FE solution and predicted $\sigma_{YY\text{-}Max\text{-}Top\text{-}Tens.}$ and $\sigma_{1\text{-}Max\text{-}Top\text{-}Tens.}$ to temperature gradient changes, and the results indicate that the sensitivities obtained by the FE solution and the ANN prediction are close, with NSI_{B787} values for $\sigma_{YY\text{-}Max\text{-}Top\text{-}Tens.}$ of 0.47 and 0.40 for NIKE3D and ANN and NSI_{B777} values of 0.40 and 0.42 for NIKE3D and ANN, respectively. The NSI_{ANN} values for $\sigma_{1\text{-}Max\text{-}Top\text{-}Tens.}$ are 0.50 and 0.35 and for NSI_{NIKE3D} are 0.45 and 0.38 for B787-8 and B777-300, respectively. These results indicate that ANN model predictions are just as sensitive as NIKE3D-FAA solutions to temperature gradients, proving the accuracy of the ANN models in predicting critical tensile stresses.

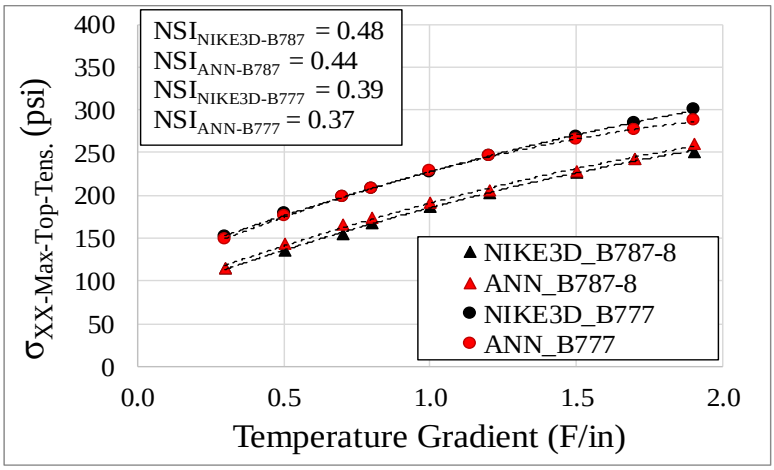

(a)

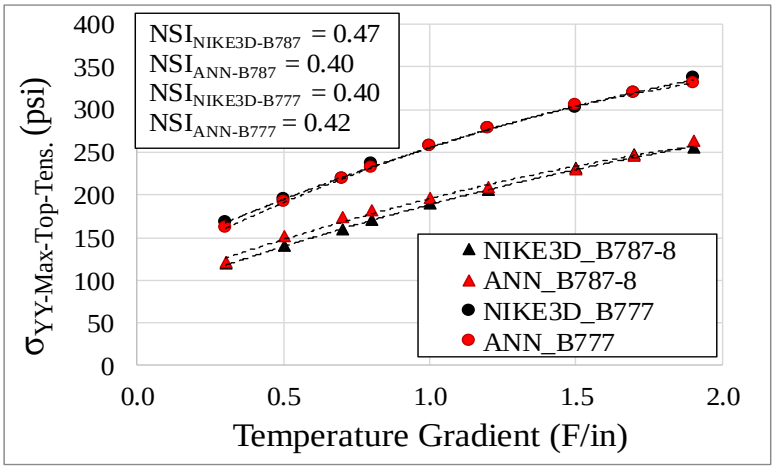

(b)

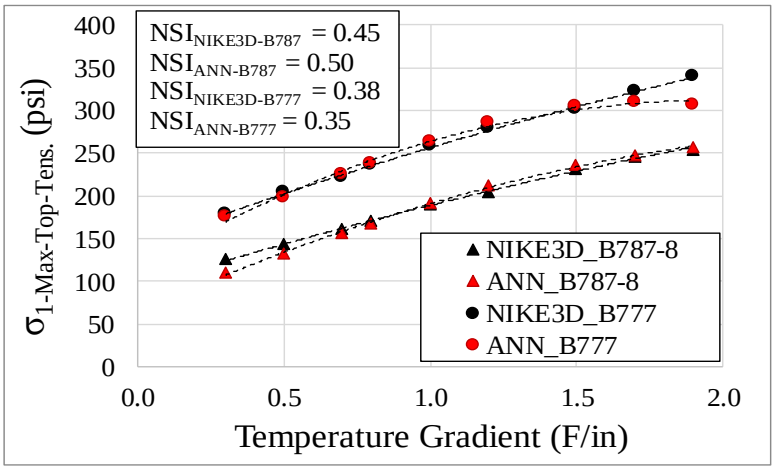

(c)

Figure 4.15 *Variation of the critical responses (a) $\sigma_{XX\text{-}Max\text{-}Top\text{-}Tens.}$ (b) $\sigma_{YY\text{-}Max\text{-}Top\text{-}Tens.}$ (c) $\sigma_{1\text{-}Max\text{-}Top\text{-}Tens.}$, obtained by NIKE3D-FAA solutions and ANN response model predictions vs. temperature gradient changes.*

Effect of Thermal Coefficient on the Predicted Responses

The sensitivity of the tensile stresses to thermal coefficient variation is illustrated in Figure 4.16. The response prediction models can replicate the NIKE3D-FAA FE solution. The sensitivity of predicted stress to variations in the thermal coefficient is similar in the ANN prediction and the FE solution. Figure 4.16 (a) shows $NSI_{B787\text{-}8}$ values of 0.49 and 0.50 for the NIKE3D-FAA solution and the ANN prediction, respectively. Figure 4.16 demonstrates that for thermal coefficients higher than 6.6×10^{-6}, while the B787-8's ANN response prediction and NIKE3D solution do not produce the same value, the difference is less than 30 psi. For the B777-300 ER the ANN response predictions fit the NIKE3D solutions. The ability of the ANN critical response models to predict maximum stresses and their sensitivities to input values can assure accurate replication of the NIKE3D-FAA solutions for the critical stresses.

Summary

Mechanical Loading Only

Figures 4.17 through 4.20 summarize the sensitivity analysis results. Figures 4.17 and 4.18 show the rigid pavement feature rankings based on the sensitivity of the critical top tensile stresses to these features under aircraft-only load. The ranking is almost the same whether based on the NIKE3D-FAA solution or ANN critical response prediction. Figure 4.17 shows that the top five most effective parameters that have the same ranking order for the B777-300 ER's NIKE3D solution and ANN prediction. Figure 4.18 also shows that the top five most effective parameters and their ranking order are the same for B787-8's NIKE3D solution and ANN prediction except for slab modulus and subbase thickness.

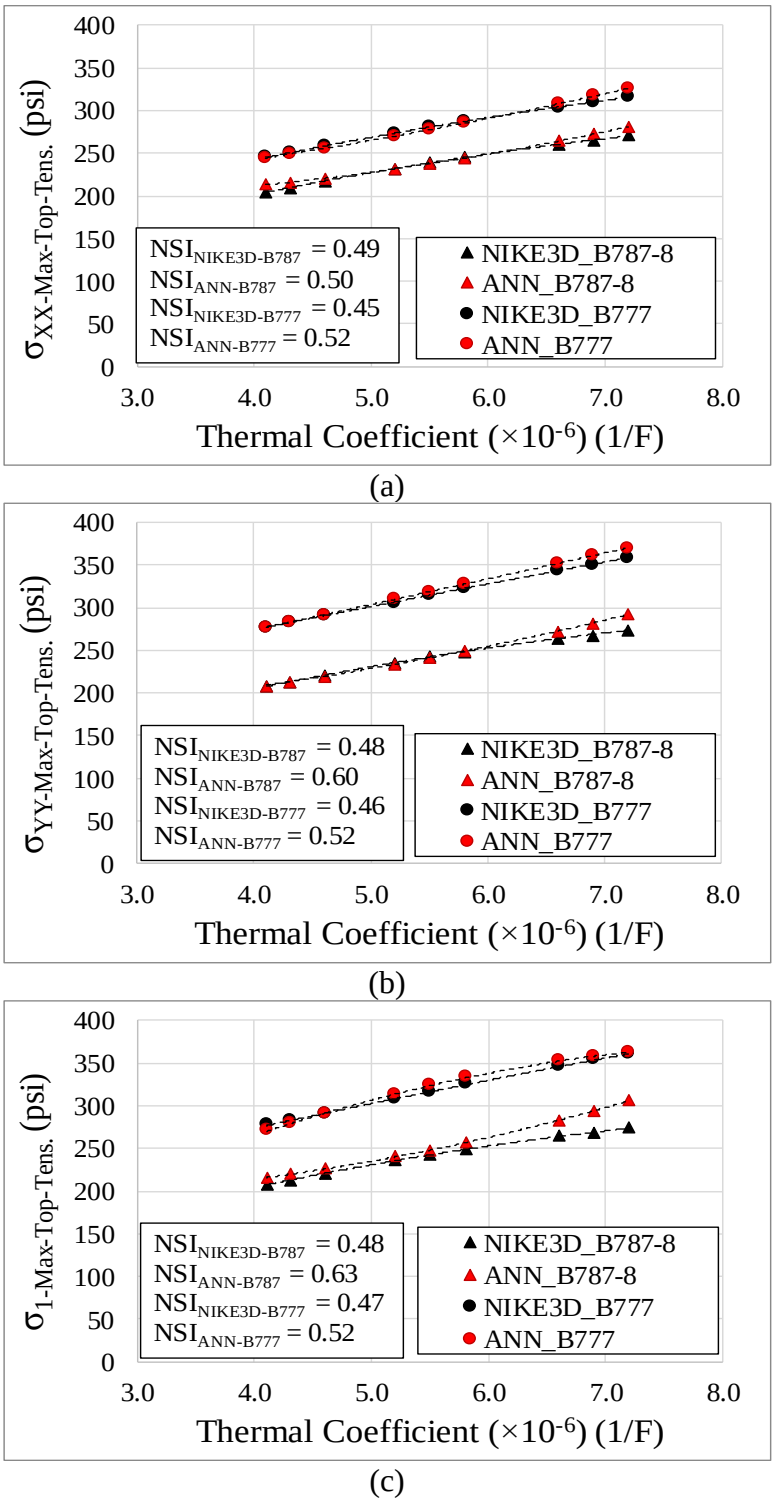

Figure 4.16 *Variation of the critical responses (a) $\sigma_{XX\text{-}Max\text{-}Top\text{-}Tens.}$ (b) $\sigma_{YY\text{-}Max\text{-}Top\text{-}Tens.}$ (c) $\sigma_{1\text{-}Max\text{-}Top\text{-}Tens.}$, obtained by NIKE3D-FAA solutions and ANN response model predictions vs. thermal coefficient changes.*

Simultaneous Mechanical and Temperature Loading

Figure 4.19 and Figure 4.20 show rigid pavement features ranking based on the sensitivity of the critical top tensile stresses under combined temperature and mechanical loading. The figures show that the pavement features rankings based on the NIKE3D-FAA solution and ANN critical response prediction are almost the same. Figure 4.19 shows that the top five most effective parameters and their ranking order are the same for B777-300 ER's NIKE3D solution and the ANN prediction. Figure 4.20 also shows that the top four most effective parameters are the same for B787-8's NIKE3D solution and the ANN prediction.

Based on sensitivity analysis, it can be concluded that the ANN model developed to study different critical responses for each type of aircraft can satisfactorily predict the actual value and the sensitivity of the responses to pavement feature alterations. The sensitivity analysis is also a good way of testing the trained ANN models with a very independent testing data set.

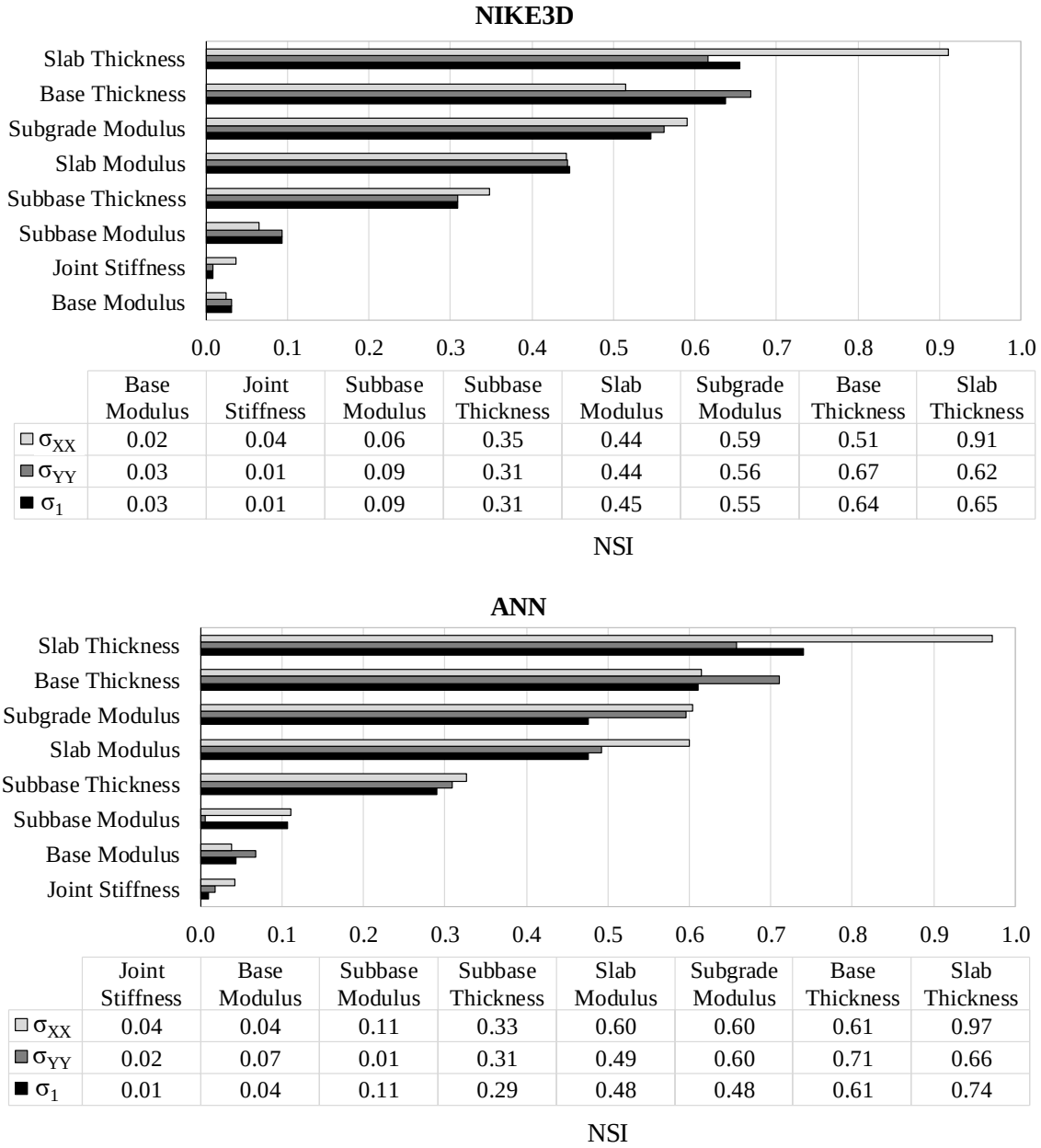

	Base Modulus	Joint Stiffness	Subbase Modulus	Subbase Thickness	Slab Modulus	Subgrade Modulus	Base Thickness	Slab Thickness
σ_{XX}	0.02	0.04	0.06	0.35	0.44	0.59	0.51	0.91
σ_{YY}	0.03	0.01	0.09	0.31	0.44	0.56	0.67	0.62
σ_1	0.03	0.01	0.09	0.31	0.45	0.55	0.64	0.65

	Joint Stiffness	Base Modulus	Subbase Modulus	Subbase Thickness	Slab Modulus	Subgrade Modulus	Base Thickness	Slab Thickness
σ_{XX}	0.04	0.04	0.11	0.33	0.60	0.60	0.61	0.97
σ_{YY}	0.02	0.07	0.01	0.31	0.49	0.60	0.71	0.66
σ_1	0.01	0.04	0.11	0.29	0.48	0.48	0.61	0.74

Figure 4.17 *NSI value showing the sensitivity of top tensile stresses to different pavement characteristics for NIKE3D FEM solution and ANN prediction of B777-300 ER mechanical loading only case.*

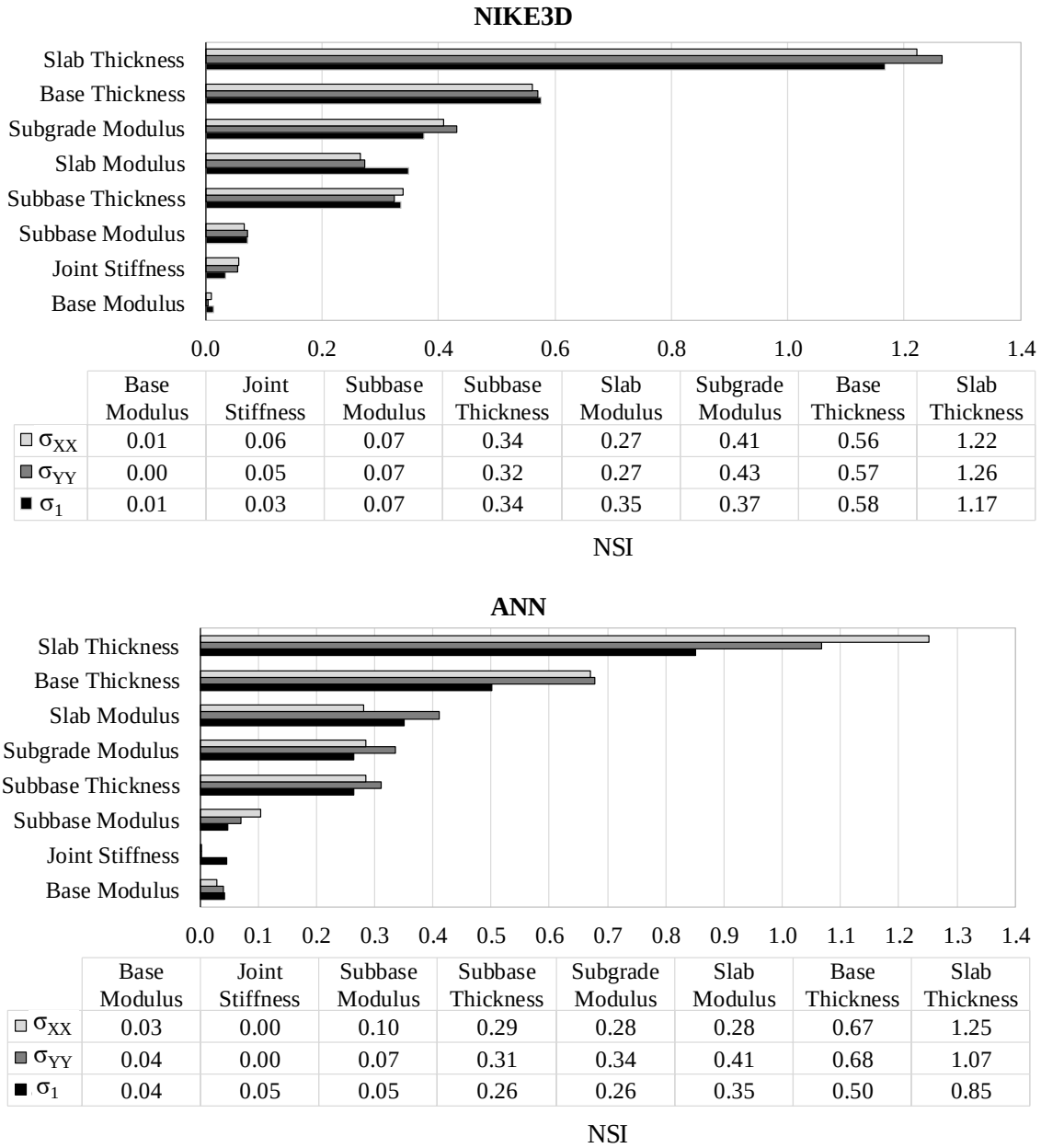

	Base Modulus	Joint Stiffness	Subbase Modulus	Subbase Thickness	Slab Modulus	Subgrade Modulus	Base Thickness	Slab Thickness
σ_{XX}	0.01	0.06	0.07	0.34	0.27	0.41	0.56	1.22
σ_{YY}	0.00	0.05	0.07	0.32	0.27	0.43	0.57	1.26
σ_1	0.01	0.03	0.07	0.34	0.35	0.37	0.58	1.17

	Base Modulus	Joint Stiffness	Subbase Modulus	Subbase Thickness	Subgrade Modulus	Slab Modulus	Base Thickness	Slab Thickness
σ_{XX}	0.03	0.00	0.10	0.29	0.28	0.28	0.67	1.25
σ_{YY}	0.04	0.00	0.07	0.31	0.34	0.41	0.68	1.07
σ_1	0.04	0.05	0.05	0.26	0.26	0.35	0.50	0.85

Figure 4.18 *NSI value showing the sensitivity of top tensile stresses to different pavement characteristics for NIKE3D FEM solution and ANN prediction of B787-8 mechanical loading only case.*

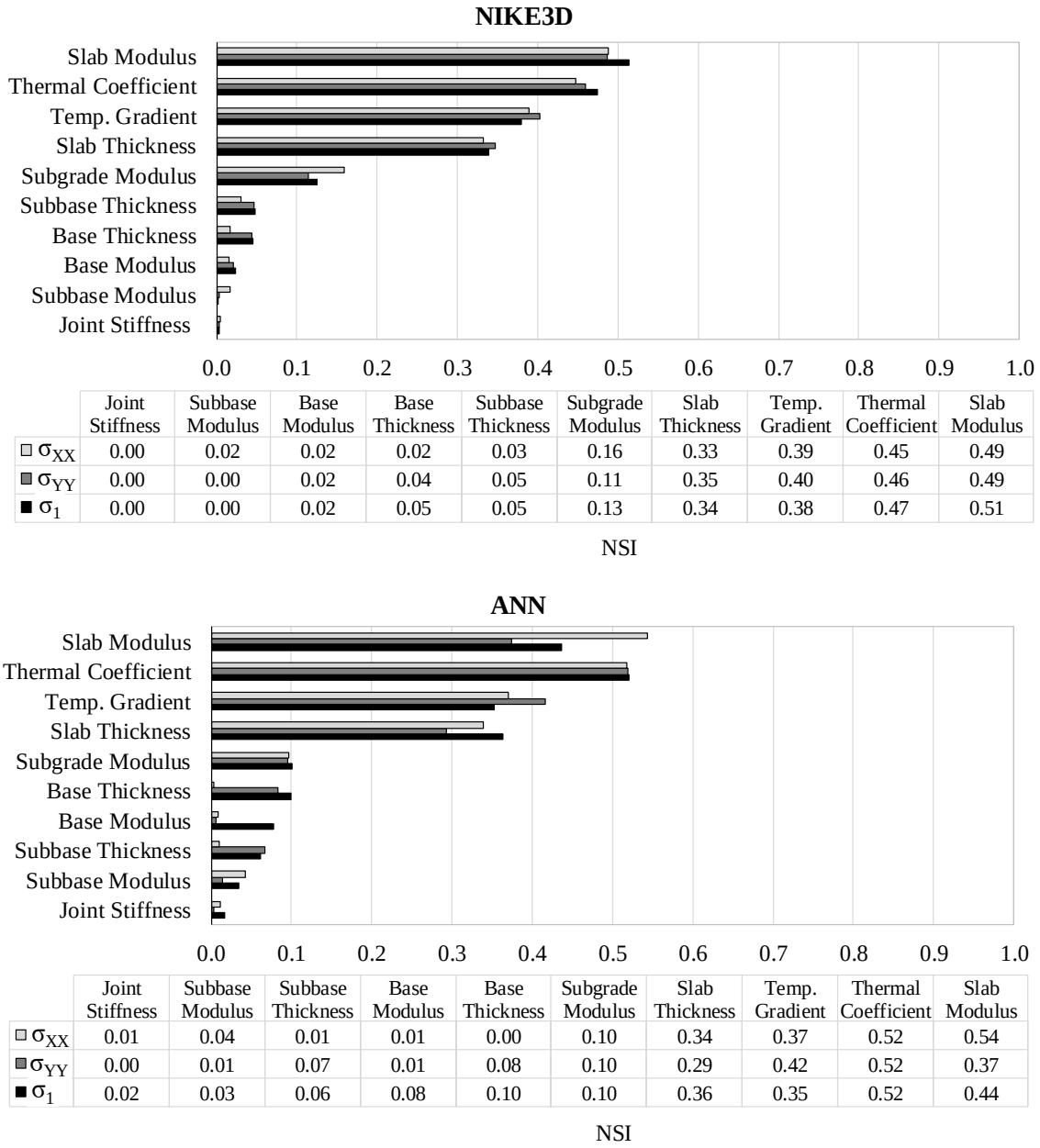

	Joint Stiffness	Subbase Modulus	Base Modulus	Base Thickness	Subbase Thickness	Subgrade Modulus	Slab Thickness	Temp. Gradient	Thermal Coefficient	Slab Modulus
σ_{XX}	0.00	0.02	0.02	0.02	0.03	0.16	0.33	0.39	0.45	0.49
σ_{YY}	0.00	0.00	0.02	0.04	0.05	0.11	0.35	0.40	0.46	0.49
σ_1	0.00	0.00	0.02	0.05	0.05	0.13	0.34	0.38	0.47	0.51

	Joint Stiffness	Subbase Modulus	Subbase Thickness	Base Modulus	Base Thickness	Subgrade Modulus	Slab Thickness	Temp. Gradient	Thermal Coefficient	Slab Modulus
σ_{XX}	0.01	0.04	0.01	0.01	0.00	0.10	0.34	0.37	0.52	0.54
σ_{YY}	0.00	0.01	0.07	0.01	0.08	0.10	0.29	0.42	0.52	0.37
σ_1	0.02	0.03	0.06	0.08	0.10	0.10	0.36	0.35	0.52	0.44

Figure 4.19 *NSI value showing the sensitivity of top tensile stresses to different pavement characteristics for NIKE3D FEM solution and ANN prediction of simultaneous temperature and B777-300 ER mechanical loading case.*

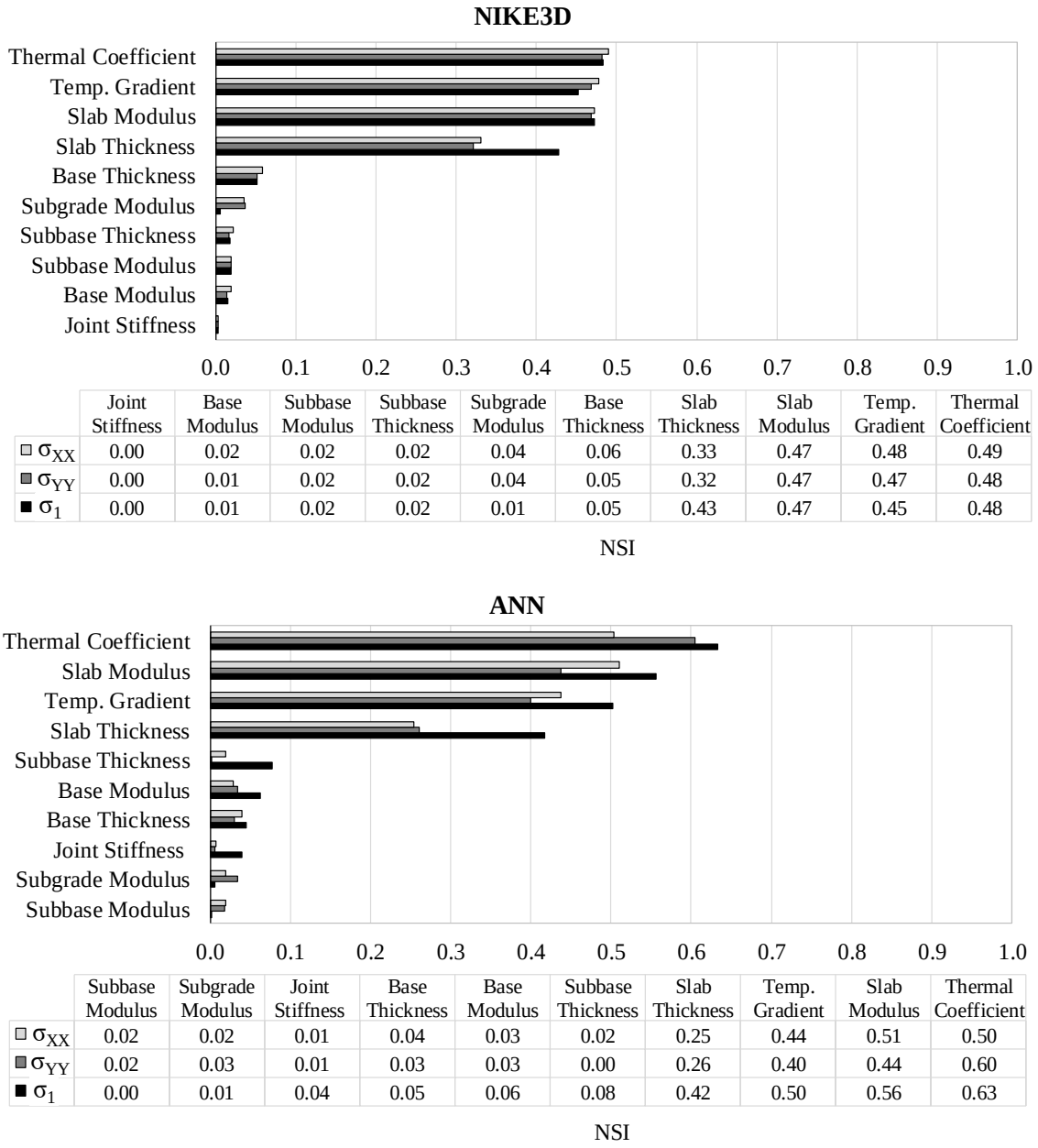

	Joint Stiffness	Base Modulus	Subbase Modulus	Subbase Thickness	Subgrade Modulus	Base Thickness	Slab Thickness	Slab Modulus	Temp. Gradient	Thermal Coefficient
σ_{XX}	0.00	0.02	0.02	0.02	0.04	0.06	0.33	0.47	0.48	0.49
σ_{YY}	0.00	0.01	0.02	0.02	0.04	0.05	0.32	0.47	0.47	0.48
σ_1	0.00	0.01	0.02	0.02	0.01	0.05	0.43	0.47	0.45	0.48

	Subbase Modulus	Subgrade Modulus	Joint Stiffness	Base Thickness	Base Modulus	Subbase Thickness	Slab Thickness	Temp. Gradient	Slab Modulus	Thermal Coefficient
σ_{XX}	0.02	0.02	0.01	0.04	0.03	0.02	0.25	0.44	0.51	0.50
σ_{YY}	0.02	0.03	0.01	0.03	0.03	0.00	0.26	0.40	0.44	0.60
σ_1	0.00	0.01	0.04	0.05	0.06	0.08	0.42	0.50	0.56	0.63

Figure 4.20 *NSI value showing the sensitivity of top tensile stresses to different pavement characteristics for NIKE3D FEM solution and ANN prediction of simultaneous temperature and B787-8 mechanical loading case.*

Summary and Conclusions

The most accurate ANN models were obtained for each type of critical response ($\sigma_{XX\text{-}Max\text{-}Top\text{-}Tens.}$, $\sigma_{YY\text{-}Max\text{-}Top\text{-}Tens.}$, and $\sigma_{1\text{-}Max\text{-}Top\text{-}Tens.}$) and for each type of aircraft under both

mechanical and mechanical and temperature induced loading. Accuracy of the ANN critical response prediction models for (a) $\sigma_{XX\text{-}Max\text{-}Top\text{-}Tens.}$, (b) $\sigma_{YY\text{-}Max\text{-}Top\text{-}Tens.}$, and (c) $\sigma_{1\text{-}Max\text{-}Top\text{-}Tens.}$ responses were presented and discussed. Sensitivity of the ANN response model predictions with respect to some of the most effective rigid airfield pavement properties have been implemented. This evaluation can help determine the performance of ANN based multiple-slab response models when a slight variation in pavement properties occurs. Key findings and major conclusions of this chapter are listed below:

- A combination of absolute average error (AAE), maximum absolute error (MAE), coefficient of correlation (R^2), and root mean squared error (RMSE) assessment criteria were used to assess model performance and accuracy, since any individual item represents only one aspect of model performance. In order to determine optimal ANN model, (1) the architecture of ANN model with the lowest independent testing RMSE was selected as the optimal architecture for each training algorithm and then (2) the algorithm showing highest R^2 for training, testing, validation, and independent testing, was determined as the optimal training algorithm.
- ANN model accuracy using different dataset sizes were compared, with results showing that increasing dataset size (from 100 to 5,000) improves capability for generalization up to a point.
- Since as a dataset becomes larger than 2,000 elements, ANN model accuracy in predicting top tensile stresses does not significantly change, a 2,000 element dataset was adopted for developing critical responses.
- ANN models were found to successfully replicate FEAFAA/NIKE3D-FAA pavement response solutions. Since comparing the results for all three responses showed that

ANN models predict top tensile stress responses accurately, they can significantly help in analyzing top-down cracks by predicting the most critical associated stress responses.

- ANN model mechanical loading predictions were more accurate for larger and heavy aircraft than for smaller aircraft, meaning that ANN models for aircraft most likely to produce higher critical stresses for top-down cracking can predict and estimate top-down cracking development very well.
- For most aircraft, 19-5-5-1 was the most accurate architecture for an ANN model used to predict tensile stresses under simultaneous temperature and mechanical loading condition.
- Since models developed in this study are for rigid pavements with 9 slabs, the critical responses of pavement systems with some other number of slabs may not be correctly predicted by the models described in this study.
- ANN models developed in this study are used for predicting critical responses for new rigid airfield pavements and are not suitable for predicting critical responses for concrete overlays.
- An ANN model developed for studying different critical responses for each type of aircraft can predict the actual value and the sensitivity of the responses to pavement feature alterations. Sensitivity analysis is also a good method for testing trained ANN models with a very independent testing data set.
- Similar sensitivity of the ANN response model predictions and the FE solutions with respect to PCC slab variations suggests that ANN models are promising for predicting $\sigma_{XX\text{-}Max\text{-}Top\text{-}Tens.}$, $\sigma_{YY\text{-}Max\text{-}Top\text{-}Tens.}$, and principal stresses even for slight changes in PCC

slab thickness for both mechanical and combined mechanical and temperature loading. In other words, an ANN model can precisely predict top tensile stresses when the PCC slab thickness varies even when temperature loading is applied.

- Under both mechanical-only loading and simultaneous temperature and mechanical loading conditions, ANN critical response models provide similar sensitivity as actual finite element solution to PCC slab modulus changes.
- ANN model sensitivity analysis results suggest that their critical tensile stress predictions are as sensitive as NIKE3D-FAA solutions with respect to thermal coefficient and temperature gradients. In other words, the results indicate that ANN models can detect the influence of the PCC slab's thermal properties variations on the critical top tensile stresses prediction, and can also lead to better prediction of top-down cracking behavior even under complex combined temperature and mechanical loading conditions.
- Under simultaneous temperature and mechanical loading conditions, a slab's thermal properties (temperature gradient and thermal coefficient) affect the critical top tensile stresses while base and subbase layer properties have less effect on stresses.
- The top five most effective input parameters related to the NIKE3D's tensile stresses solution are the same as those for ANN model tensile stresses prediction under mechanical-loading-only condition.
- The five most effective parameters and their ranking order are the same for the B777-300 ER's NIKE3D solution and ANN prediction, and the top four most effective parameters are the same for B787-8's NIKE3D solution and ANN prediction.

References

[1] A. Rezaei-Tarahomi, H. Ceylan, K. Gopalakrishnan, S. Kim, O. Kaya, and D. R. Brill, "Artificial Neural Network Models for Airport Rigid Pavement Top-Down Critical Stress Predictions: Sensitivity Evaluation," in 2019 ASCE International Airfield and Highway Pavements Conference, 2019.

[2] A. Rezaei-Tarahomi, O. Kaya, H. Ceylan, K. Gopalakrishnan, S. Kim, and D. R. Brill, "Using Sensitivity Evaluations for Studying Multiple Slabs Concrete Pavements Critical Responses Associated with Top-down and Bottom-up Cracking," in Transportation Research Board 96th Annual Meeting, Washington D.C., 2017.

[3] A. Rezaei-Tarahomi, O. Kaya, H. Ceylan, K. Gopalakrishnan, S. Kim, and D. R. Brill, "Sensitivity quantification of airport concrete pavement stress responses associated with top-down and bottom-up cracking," Int. J. Pavement Res. Technol., vol. 10, no. 5, pp. 410–420, 2017.

[4] K. Grace-Martin, "Assessing the Fit of the Model," 2013. [Online]. Available: http://doi.wiley.com/10.1002/9781118548387.ch5.

[5] K. Gopalakrishnan, H. Ceylan, and N. O. Attoh-Okine, Intelligent and soft computing in infrastructure systems engineering: recent advances, vol. 259. Springer, 2009.

[6] T. Chai and R. R. Draxler, "Root mean square error (RMSE) or mean absolute error (MAE)? -Arguments against avoiding RMSE in the literature," Geosci. Model Dev., vol. 7, no. 3, pp. 1247–1250, 2014.

[7] A. R. Ghanizadeh and M. R. Ahadi, "Application of Artificial Neural Networks for Analysis of Flexible Pavements under Static Loading of Standard Axle," vol. 3, no. 1, 2016.

[8] K. Gopalakrishnan, M. R. Thompson, and A. Manik, "Rapid Finite-Element Based Airport Pavement Moduli Solutions using Neural Networks," Comput. Intell., vol. 3, no. 1, pp. 63–71, 2006.

CHAPTER 5. RELIABILITY-BASED DESIGN OPTIMIZATION OF AIRPORTS CONCRETE PAVEMENT

Abstract

The current state-of-the-art airfield concrete pavement design is accomplished using FAARFIELD software developed and released by the U.S. Federal Aviation Administration (FAA). Since this mode of design is implemented based on some initial assumed inputs, obtaining an optimum design for a given traffic and environmental loading and design age is an iterative process to find the best possible design. However, it takes considerable amount of time to perform this iterative process using the 3-D Finite Element (FE) based FAARFIELD software. To overcome this challenge, a more efficient methodology, Simulation Optimization for Airfield Rigid Pavement (SOARP), is proposed. SOARP relies on artificial neural network (ANN) models combined with a design optimization framework to determine the optimal design of airfield rigid pavement, and this optimal design should perform satisfactorily for different values of uncertain parameters. SOARP is implemented for various reliability levels and design lives for the airfield rigid pavement. In addition, the pavement thickness designed by SOARP and FAARFIELD are compared for various flexural strength and reliability levels. The results show that SOARP either results in more reliable or less expensive pavement designs.

Introduction

Airport pavements are designed over many years to withstand repeated traffic loading imposed by a broad entire range of aircraft types over many years, to resist the abrasive action of traffic, and to endure deterioration induced by adverse weather conditions (e.g., extreme hot or cold weather) and other influences in a cost-effective manner. For rigid airport pavement design, the Federal Aviation Administrative (FAA) uses three-dimensional

finite- element (3D-FE) procedures for rigid airport pavement design, as implemented in the FAA Rigid and Flexible Iterative Elastic Layer Design (FAARFIELD) program [1]. The iterative processes encountered in rigid pavement thickness design based on 3D-FE solution exhibit long and unpredictable run times, especially when the number of slabs is increased and top-down cracking is considered [2]–[6].

Although there are many features affecting pavement performance, typical airfield rigid pavement design processes in FAARFIELD use a trial-and-error approach to find optimum slab size (joint spacing), joint stiffness, temperature-induced initial curling, and predefined load location, using a trial-and -error approach. Since it is also not practical to determine the optimum design solution from an exhaustive set of all acceptable designs using this approach [7], some practical alternatives are needed to expand the airfield rigid pavement design beyond the current restricted approach, making design calculation computationally-tractable, agile, and comprehensive. To achieve this goal, this study proposes a novel approach utilizing Artificial Neural Networks (ANN) along with an optimization technique for airfield rigid pavement design, recognizing that there have been previous studies utilizing predictive models (e.g., ANN) or optimization methods in pavement design and rehabilitation problems to make pavement engineering practices versatile and practical.

Santos and Ferreira [8] presented a deterministic pavement-design optimization model that considers pavement performance, construction costs, maintenance and rehabilitation costs in the model, assuming deterministic values for all model parameters. Mikolaj, et.al., [9] optimized a rehabilitation plan featuring cost-benefit analysis to maximize life-cycle length of pavement constructed with asphalt concrete materials. Hadi and Arfiadi

[10] used a genetic algorithm to optimize pavement building costs of rigid highway pavement. Mamlouk et al. [11] developed a project-level optimization model for flexible pavements whose design variables were initial pavement thickness, overlay thickness, and overlay timing used to minimize highway agency and user costs.

Engineering design problems typically have multiple variables, and there is often uncertainty around these variables [12]. Monte Carlo simulation is often used to explore the design output given design parameters [13]. Some studies in the pavement design area have considered that simulation evaluates the effects of different design inputs on the desired output [14]–[16]. For example, Timm & Newcomb [14] developed a Monte Carlo simulation framework for asphalt to conduct a probabilistic analysis of pavement reaction to loading and to evaluate the resulting damage. In their proposed framework, to meet the damage criteria, random samples were generated from probability distributions of asphalt layer thickness, loading configurations, and material properties, and sequences of new random numbers were generated from the input parameters until the level of damage is less than a threshold value. Their proposed frameworks lack an optimization model that could lead to an exact or near-exact solution.

Design of new and rehabilitated pavements involves many uncertainties, variabilities, and approximations. Generally, reliability refers to the ability of the system to perform above a safety limit under various sources of uncertainty [17]. In pavement design, reliability can be defined as the probability that pavement performance would remain within an allowable range during the design life [18]. A reliability-based pavement design can properly incorporate the uncertainty and variability to make an effective design [19], [20]. The American Association of State Highway and Transportation Officials (AASHTO)

mechanistic empirical pavement design guide (MEPDG) considers the reliability of pavement sections in the design [18]. Dinegdae et al. [18] evaluated pavement reliability analysis by incorporating response surface methods. They developed a two-component reliability analysis methodology to evaluate the reliability of fatigue cracking failure in actual field pavements. Their study shows how the influence of different design input variables can be captured within a reliability analysis framework. Retherford & McDonald [21] investigated potential reliability methods and discussed their advantages and disadvantages in the mechanistic empirical design approach to pavement design.

A number of studies applied reliability in the pavement design optimization. Sanchez-Silva et al. [22] presented a model for reliability cost-based optimization of asphalt pavement structures that considered asphalt-surface fatigue damage and the degradation of granular materials by repetitive loading cycles. They also combined reliability-based design optimization with long-term pavement-maintenance policy. Gaurav et al. [7] minimized asphalt-pavement design costs using a surrogate-based optimization approach. They considered design reliability in the model via the use of chance constraints, and the design variables were the asphalt-concrete base, and sub-base thicknesses. They considered deterministic values for model parameters such as Granular base, Granular sub-base, and sub-grade. By considering different reliability levels in pavement design optimization, decision makers can determine an optimal design that considers expected design costs or choose a design that meets their degree of risk aversion.

The objective of this study is to develop a novel design methodology called Simulation Optimization for Airfield Rigid Pavement (SOARP). SOARP is a comprehensive reliability-based simulation-optimization framework benefiting from artificial intelligence for

critical stress responses prediction for the airfield concrete design. The optimal design can be identified more quickly than with other methods. This framework empowers the designers to consider large number of scenarios for designing airfield concrete pavement. This study proposes SOARP for decision makers involved in the design of airport concrete to achieve various reliability levels. The novelty of this study and its primary difference with FAARFIELD's design methods lie in its use of ANN to predict critical responses. Another difference is to conduct airfield concrete pavement design with using Monte Carlo simulation and Bayesian optimization under different reliability levels.

ANN-based Bayesian Optimization Framework

Figure 5.1 shows the whole procedures of the SOARP Framework. The framework is aimed at minimizing the design cost while the fatigue failure of the pavement is kept under the allowable amount by a reliability constraint. The cost function (objective function) represents the total cost of the design thickness of the Portland cement concrete (PCC) slab, base layer, and subbase layer. The reliability constraint limits structural fatigue life of the pavement to an allowable load repetition-to-failure using the cumulative damage factor (CDF). The CDF calculation follows the same method used in FAARFIELD [1], [23], [24]. Unlike FAARFIELD, an ANN is used instead of finite element analysis to determine the critical response. SOARP employs ANNs as analysis engine for replicating critical stress responses associated with cracking which is used for calculating the CDF of the pavement. Using an ANN in this framework enables performing large number of simulations without interruptions induced by time-consuming analysis and complex calculations.

The following subsections describe the approaches, models, and the mathematics employed for design optimization including CDF calculations, reliability constraint, objective function, ANN models development, and Bayesian optimization algorithm.

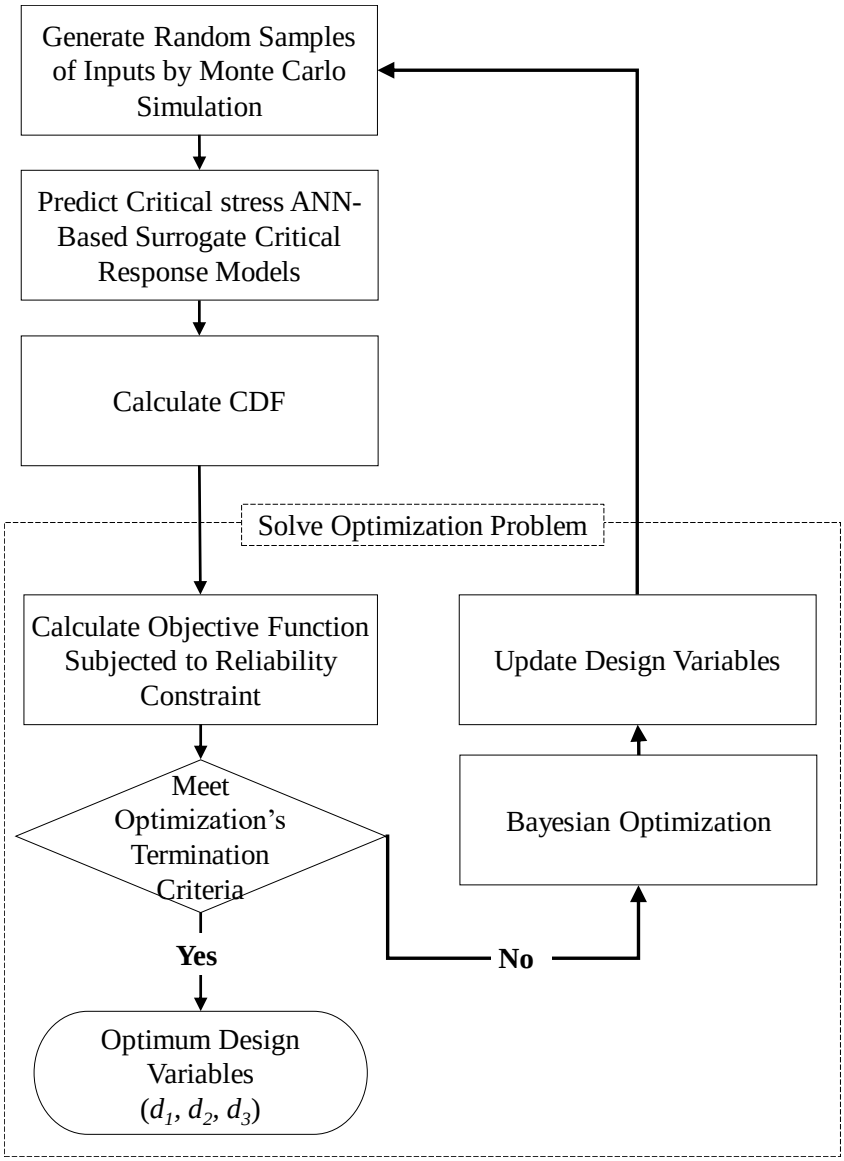

Figure 5.1 *Flow chart of the SOARP steps.*

Mathematical Model

This section describes the approaches, models, and the mathematical methods employed for design optimization, including total damage caused by an aircraft traffic mix, an objective function, and a design cost function. The objective function limits the structural fatigue life of the pavement to allowable load repetition-to-failure using cumulative damage factor (CDF). The cost function represents the total cost of the design thickness of the PCC slab, base layer, and subbase layer. In this study, design optimization was aimed toward

minimizing design cost while using a reliability constraint to keep pavement fatigue failure below a tolerable level, using the same method of fatigue life calculation used in FAA rigid airfield pavement design software (FAARFIELD) [23], [24].

The proposed design method followed the following steps:

1. Randomly generate *N* samples from the distributions of uncertain parameters: Gear loading angle (θ_g), Loading location on the slab (X and Y), temperature gradient, thermal coefficient, PCC slab cost, base layer cost, and subbase layer cost.

2. Calculate critical bottom tensile stress using the trained ANN models for the airplanes (see CHAPTER 3).

3. Calculate cumulative damage factor [1] for each airplane using the design variables (PCC slab thickness (d_1), base layer thickness (d_2), and subbase layer thickness (d_3)) by the optimization algorithm:

$$CDF = \frac{(\text{annual departure}) \times (\text{life in years})}{(\frac{\text{pass}}{\text{covrage ratio}}) \times (\text{covergae to failure})} \tag{5.1}$$

To calculate the pass-to-coverage ratio (P/C), coverage-to-pass (C/P) is calculated using Equation 5.2. For rigid pavements, the pavement surface is divided into 81 longitudinal strips (10-inch strips at lateral distance between -400 and 400 in.), and the C/P ratio is computed for each offset. For each offset i, $(C/P)_i$ is computed using the following probability equation:

$$(C/P)_i = \sum_{k=1}^{N_t} P\left[\left(x_i - \frac{w}{2}\right) \le x_k \le \left(x_i + \frac{w}{2}\right)\right] \tag{5.2}$$

where N_t is the number of tires on the landing gear, x_i is lateral distance from a longitudinal reference line (e.g., runway or taxiway centerline) to the midpoint of strip i, x_k

is the lateral distance from the same reference line to the centerline of tire k [24], and w is tire width. Coverage to design failure (C) can then be obtained by solving Equation 5.3 [23]:

$$DF = \left[\frac{F_s^{'} bd}{(1-\alpha)(d-b)+F_s^{'} b}\right] \times \log C + \left[\frac{(1-\alpha)(ad-bc)+F_s^{'} bc}{(1-\alpha)(d-b)+F_s^{'} b}\right] \tag{5.3}$$

where the design factor $DF = R/\sigma$ and $\alpha = SCI/100$. R is the flexural strength of the PCC and σ is the analytical stress obtained by ANN critical response models. For new rigid pavements, a structural condition index (*SCI*) of 80 is the FAA definition of structural failure, consistent with the condition that 50 percent of slabs in the traffic area exhibit a structural crack [25]. The parameter values of Equation 5.3 from Brill and Kawa [26] are:

$$\begin{aligned} F_s^{'} &= 1 \\ b = d &= 0.160 \\ a &= 0.760 + 2.543\times 10^{-5}(E-4500) \\ c &= 0.857 + 2.314\times 10^{-5}(E-4500) \end{aligned} \tag{5.4}$$

where E is the subgrade modulus considered to be 20,000 psi in this chapter. To calculate the cumulative CDF (CCDF), the CDF values for all airplanes in the traffic mix load are summed for each of the 81 strips, after which the peak value of the CCDF is represented as TCDF (Equation 5.3). Figure 5.2 shows the CCDF and CDF values calculated by Equation 5.1 for each airplane.

$$\begin{aligned} CCDF_s &= \sum_{k=1}^{4} CDF_{ks} \qquad \forall s = \{1,2,...,80\} \\ TCDF &= \max_s CCDF_s \end{aligned} \tag{5.5}$$

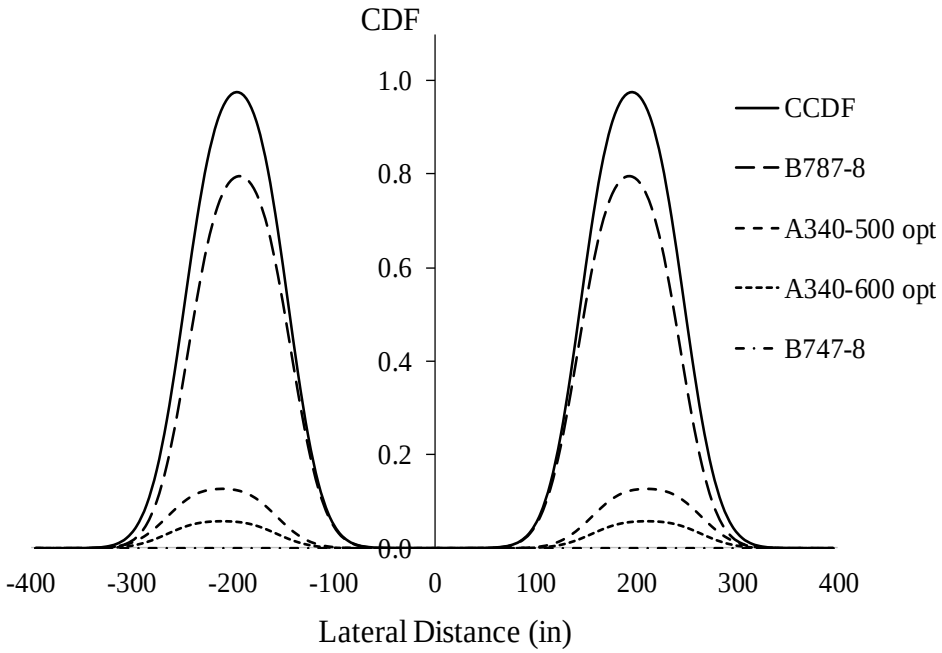

Figure 5.2 *CCDF and the CDF for each airplane.*

4. Solve the optimization problem and use MSC to determine the expected design cost, while ensuring that the reliability constraint is not violated:

$$\begin{aligned} &\underset{d\in D}{\text{minimize}}\ \frac{1}{N}\sum_{j=1}^{N}\sum_{q=1}^{Q}C_{jq}d_q \\ &\text{subject to}\ P\left(TCDF \le T\right) \ge \Re \end{aligned} \tag{5.6}$$

The first part of Equation (5.6) represents the expected design cost considering N simulations, where C_{jq} is the cost of design for design variable d in simulation j. Since several of the parameters are uncertain, Monte Carlo simulation can be used to calculate the cost function, with the expected cost of design calculated as the average after N different simulations. The second part of Equation (5.6) shows the reliability constraint representing the simulated probability that TCDF is less than or equal to T (e.g., 1.05), where T is the TCDF threshold.

The decision maker establishes reliability level $\Re$ (e.g., 0.95) before optimizing the problem using Equation (5.6). For a design to be reliable, the TCDF should be less than the threshold (T) $\Re$% of the time. This framework allows the design to fail fewer than $(1-\Re)$% of the time. If $TCDF > T$ the pavement will fail before reaching its design life, but it would be too costly to build or design a system that would never fail during its operation.

The Bayesian optimization algorithm is used to solve this problem. The algorithm procedure and the optimization termination criteria are elaborated in detail in Optimization Algorithm section.

Artificial Neural Networks

Previous chapters showed that employing ANN in the current FAA design process can be beneficial by performing rapid analysis and reducing computer run time for multiple-slab simulation to a matter of seconds. Incorporating ANN surrogate response models into the pavement design process can therefore significantly enhance efficiency of the design process by reducing the iteration time for calculation of critical stresses for each type of aircraft in a mixed-aircraft traffic loading scenario. Using rapid-response ANN models can also help expand current design method beyond those compromising the currently used one-slab model involving limited-loading circumstances.

Before incorporating such alternative models into the current FAA design process, they must be tested and validated. Chapter I assesses ANN models accuracy in analyzing airfield concrete pavement using various testing, independent testing, and sensitivity testing data sets. The accuracy metrics demonstrated promising predictions for training and testing and confirmed a good fit and a lack of memorization of the predictors-output relationship. In addition, this study is presenting SOARP method which employs the trained ANN models

along with the FAA's airfield concrete pavement design. This method enables finding the optimum thickness for each pavement's layer by using the ANN-predicted critical stress. Moreover, it is implemented in a case study and then validated by comparing SOARP method with FAARFIELD.

Optimization Algorithm

In this study, the expected cost of design is minimized under different reliability levels. To calculate the objective function and determine an optimal design, the ANN model is used in each simulation scenario. ANNs are complex black box functions whose outputs provide little information about functional forms because there is often no simple relationship between network weights and model properties [27]. The first or second order information of the highly nonlinear simulation model is hard to estimate. Hence, the traditional optimization algorithms such as gradient descent which uses the first order information of the objective function is not applicable to solve the problem. The Bayesian optimization is able to achieve accurate results in reasonable time compared to other optimization algorithms such as random search and evolutionary algorithms [28]. This algorithm outperforms other global optimization algorithms on challenging optimization problems [29].

Bayesian optimization algorithm can effectively model input-output relationships of a black-box model. The inputs of the model are the design variables and the outputs are the design costs evaluated with the Monte Carlo simulation. As the procedure to calculate the design is complex and consist of uncertain parameters, the design cost can only be evaluated with the Monte Carlo simulation. Considering uncertainty in the parameters in the pavement design frameworks requires the use of computationally expensive simulations to evaluate and calculate the objective function. Bayesian optimization generates candidate designs and inserts them into the model and then evaluates the resulting objective function to minimize

expected cost. This algorithm constitutes a powerful method for finding the optimal design d^*.

The Bayesian optimization algorithm creates a surrogate model for the objective function and exploits it in order to find the next evaluation points in the feasible solution space [30]. The Gaussian process is a powerful prior distribution for functions; therefore, we select it as the prior over the objective function [29]. Bayesian optimization estimates the objective function using J samples of the design variables d. The algorithm fits a prior multivariate normal with a mean of 0 and covariance matrix K over the J samples. After simulating J design alternatives to estimate $f_{1:J}$ - the expected cost assuming the J design alternatives - the posterior mean and variance of a new design alternative $d^{'}$ can be calculated using the Sherman-Woodbury-Morrison formula:

$$\mu(d^{'} \mid d_{1:J}) = k(d^{'}, d_{1:J}) K(d_{1:J}, d_{1:J})^{-1} f_{1:J} \tag{5.7}$$

$$\sigma^2(d^{'} \mid d_{1:J}) = k(d^{'}, d^{'}) - k(d^{'}, d_{1:J}) K(d_{1:J}, d_{1:J})^{-1} f_{1:J} \tag{5.8}$$

where $d_{1:J}$ is the J previously evaluated thicknesses used to predict the next point. The objective function at the new design alternative d' has the following form:

$$f(d' \mid d_{1:J}) \sim N\left(\mu(d' \mid d_{1:J}), \sigma^2(d' \mid d_{1:J})\right) \tag{5.9}$$

Bayesian optimization selects the $J+1$ design variable by maximizing the following utility (i.e., acquisition) function:

$$u(d^{'} \mid S_{1:J}) = E(\max\{0, f_{J+1}(d) - f(d^{+})\} \mid S_{1:J}) \tag{5.10}$$

where $d^{+} = \arg\max_{d \in \{d_{1:J}\}} f(d)$ is the current best design that results in the smallest expected design cost based on J evaluated alternatives. The set $S_J = \{d_{1:J}, f_{1:J}\}$ contains J design alternatives and their corresponding expected costs assessed via simulation. Maximizing the

acquisition function represents a trade-off between exploration and exploitation. When the algorithm chooses to exploit, it seeks to sample in solution spaces close to designs that already generate small expected costs. However, when it explores the solution space it chooses to simulate a design alternative with a larger uncertainty [31]. This procedure iterates until there is very little improvement in the objective function or the maximum number of iterations I is reached (i.e, termination criteria) [32], [33]. Algorithm 1 describes the Bayesian optimization procedure. The implementation procedure is adopted from the Random Embedding Bayesian Optimization (REMBO) algorithm developed by Wang et al. [34].

Algorithm 1 Implementation procedure of Bayesian optimization

1: **for** $i = 1$ to I **do**
2: Calculate $\mu(d^{'} \mid d_{1:J})$ and $\sigma^2(d^{'} \mid d_{1:J})$
3: Find d_{J+1} by optimizing the acquisition function
$u(d^{'} \mid d_{1:J}) = E(\max\{0, f_{J+1}(d) - f(d^{+})\} \mid d_{1:J})$
4: Use Monte Carlo simulation to calculate $f(d_{J+1})$
5: Augment data points $S_{J+1} = S_J \bigcup \{(d_{J+1}, f(d_{J+1}))\}$
6: **end for**
7: $d^{*} = \arg\max f(d_{1:J})$

8: Output: d^{*}: Optimal design variables (slab, base, and subbase thickness)

Pavement Design Optimization Case Study

The case study described in this section involved design of a nine-slab concrete pavement with base and subbase layers on top of a subgrade. Aircraft traffic assumed in this study included a B747-8, a B787-8, an A340-500 opt, and an A340-600 opt with 3,000, 3,000, 1,500, and 1,500 annual departures, respectively. The costs used for this case study were those for designing an airport in Des Moines, Iowa. [35].

Table 5.1 describes the parameters of the model along with the values used in the case study [35].

Table 5.1 *Input values used for the case study.*

Inputs		**Value**
PCC Slab	Modulus (psi)	3.0×10^{6}
	Poisson Ratio	0.15
Base	Modulus (psi)	5.0×10^{5}
	Poisson Ratio	0.2
Granular Subbase	Modulus (psi)	7.5×10^{4}
	Poisson Ratio	0.35
Subgrade	Modulus (psi)	2.0×10^{4}
	Poisson Ratio	0.4
Slab Dimension (ft.)		20×20
Loading Angle Θ_g (degree)		*Uniform*(5, 85)
Loading Position X		*Triangular*(0.47, 0.85, 1)
Loading Position Y		*Triangular*(0, 0.4, 0.5)
Temperature Gradient (^{o}F/in.)		*Normal*(0, 0.65^{2})
Thermal Coefficient (1/^{o}F)		5.1×10^{-6}
Equivalent Joint Stiffness (psi/in)		1.0×10^{5}
Concrete Strength (psi)		650
PCC Cost (6") (Sq. Yd.)		*Uniform*(55, 80)
Base Layer (6") (Sq. Yd.)		*Uniform*(20, 30)
Subbase layer (6") (Sq. Yd.)		*Uniform*(9.5, 14.5)

Based on the probabilistic distributions of uncertain parameters, 10,000 samples (enough for pavement design [14]) were generated using Monte Carlo simulation. Samples generated by the Monte Carlo simulation are then entered the ANN models to estimate the critical stress in the PCC slab.

The distribution of *TCDF* is estimated from 10,000 simulations of the inputs. If the design variables generated by algorithm 1 ensure that the reliability constraint is met, the expected cost would be recorded for that design (Equation 5.6), and this process is iterated until the optimization termination criteria has been met.

Table 5.2 shows the optimal design for different design life and reliability levels. For lives of 20, 25, and 30 years, a higher level of reliability is associated with thicker concrete pavement structure and consequent higher expected cost. For example, for a 20-year design life and 50% reliability, the total thickness is 38.3 in, while for 95% reliability it is 49.4 in., reflecting a 25% increase in the expected design cost. Figure 5.3 illustrates the rising trend in expected cost when the design life increases from 20 to 30 years and the reliability level increases from 50% to 95%.

Figure 5.4 shows the *TCDF* distribution (for 10,000 different combinations of inputs) of the optimal designs for a 20-year design life at various reliability levels. For example, the 0.95-reliability plot implies that, for 10,000 simulations, 9,500 of the designs meet the reliability constraint ($TCDF <= 1.05$). The pavement structures with the calculated optimum thicknesses withstand applied traffic and environmental loading during a 20-year design life without reaching the maximum fatigue damage level caused by the loading.

Table 5.2 *Optimal thicknesses for different design lives and reliability levels.*

Design Life	Reliability	Thickness (in)			Expected Cost
		Slab	Base	Subbase	
20	0.50	15.8	16.5	6.0	$11,446
	0.80	15.5	21.9	6.0	$12,310
	0.90	15.2	24.6	6.0	$12,642
	0.95	13.4	30.0	6.0	$12,784
25	0.50	15.9	16.2	6.0	$11,479
	0.80	15.4	22.2	6.0	$12,335
	0.90	14.6	26.7	6.0	$12,742
	0.95	13.6	30.0	6.0	$12,853
30	0.50	15.9	16.7	6.0	$11,565
	0.80	14.9	24.1	6.0	$12,422
	0.90	15.2	25.1	6.0	$12,765
	0.95	13.7	30.0	6.0	$12,951

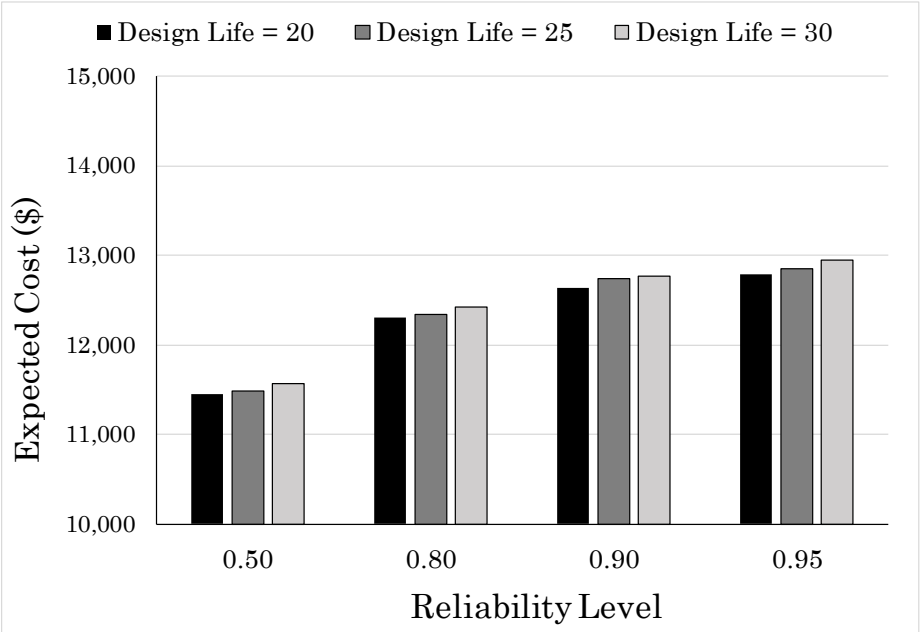

Figure 5.3 *Expected cost variation for different reliability level and design life.*

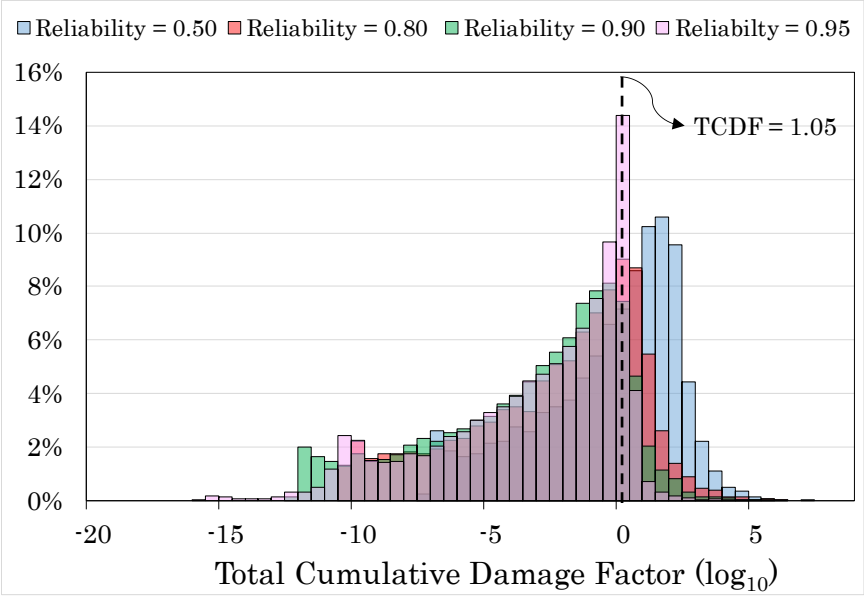

Figure 5.4 *The distribution of TCDF value for optimal design of 20 years design life.*

The expected cost for the optimal design at given different reliability levels and design lives are reported in Table 5.2. Figure 5.5 shows the distribution of the cost for the optimal design of the concrete pavement for 95% reliability and design life of 20 years. The figure shows that there is approximately a 90% probability that the design cost will be between \$10,951 and \$14,612 per 20×20 $ft.^2$ slab.

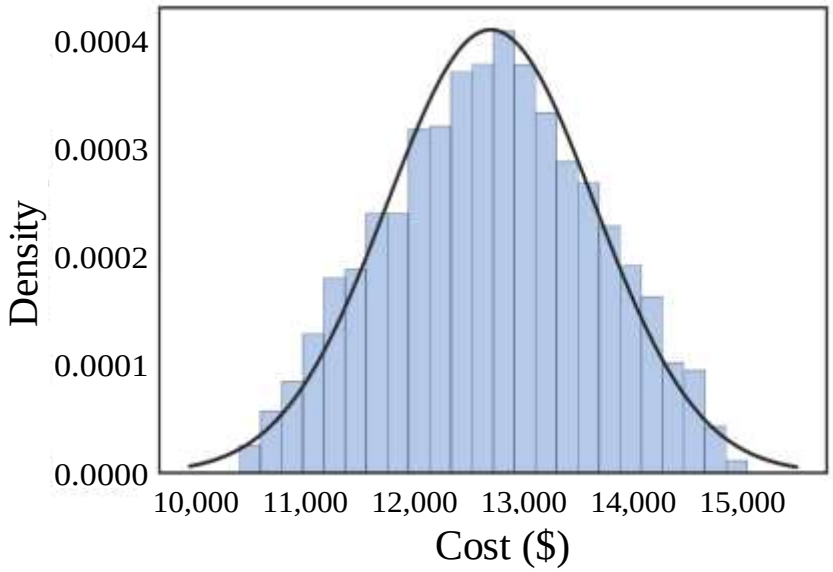

Figure 5.5 *Cost distribution of optimal design for reliability = 0.95 and design life = 20.*

Sensitivity Analysis

The sensitivity of the pavement thickness design to the PCC and subgrade elastic modulus variation will be demonstrated in this section. Although PCC and subgrade modulus were both considered constant, they are very effective in determining the responses and consequent design outcomes.

Sensitivity of total thickness to PCC flexural strength

Figure 5.6 is presented to illustrate the designed total thickness including PCC thickness (d_1), base layer thickness (d_2), and subbase layer thickness (d_3) for different PCC flexural strength values. In addition, Figure 5.6 displays the expected cost variation for various optimal design of SOARP obtained for different flexural strength. The figures show that increasing the strength of the PCC slab results in lower expected cost and total thickness ($d_1 + d_2 + d_3$) for the optimal designs. For example, increasing the flexural strength from 650 to 800 psi reduces the expected cost of a 20×20 ft slab from \$16,230 to \$11,760.

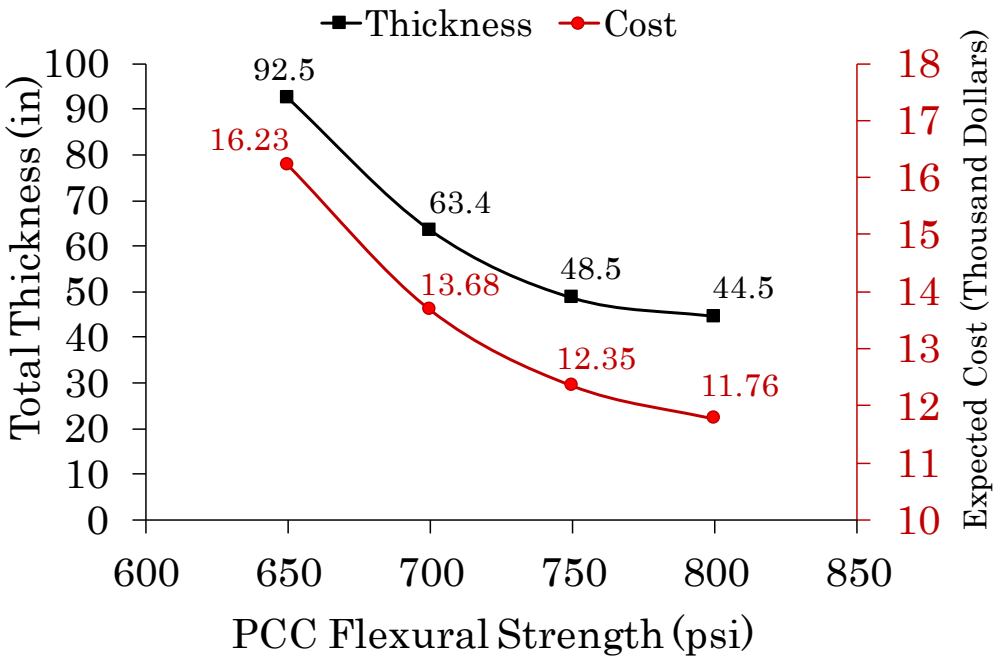

Figure 5.6 *Sensitivity analysis for PCC slab elastic modulus.*

Sensitivity of PCC thickness to subgrade elastic modulus

Figure 5.7 displays the optimum PCC thickness variation for various subgrade modulus. Figure 5.7 shows that increasing the subgrade strength will decrease the optimum PCC thickness, leading to the conclusion that stronger subgrades can afford to have thinner PCC slabs on them to be protected from load-induced deterioration. Also Figure 5.7 shows decrease of the expected cost when subgrade elastic modulus increases. In this study, variation of the subgrade modulus directly affects on critical stress occurred in the PCC slab. Higher elastic modulus results in lower critical stress and consequently lower required thickness.

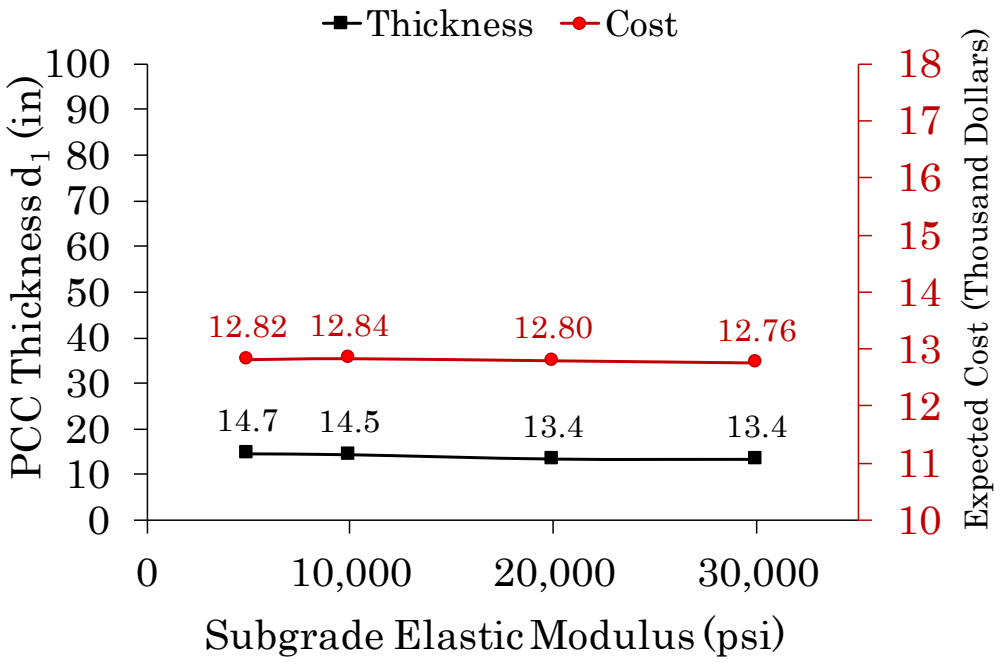

Figure 5.7 *Sensitivity analysis for subgrade elastic modulus.*

Design with FAARFIELD vs SOARP

This section compares results from the proposed design framework with those from the FAARFIELD design. FAARFIELD receives design inputs and determines the PCC slab thickness that results in CDF=1 for a given design life and traffic mix. FAARFIELD

considers the critical condition of edge loading when determining the PCC slab thickness. However, the proposed model considers 10,000 scenarios for the uncertain parameters and considers them all in the process of optimizing the thickness leading to consideration of many critical or non-critical conditions either in simulation or optimization. The proposed design has considered all possible conditions that could possibly affect the pavement.

The SOARP method is used to calculate the optimal PCC slab, base, and subbase thickness for different levels of flexural strength of the PCC. These thickness values for the base and subbase layers are used in FAARFIELD to calculate the slab thickness while assuming the same traffic loading mix, layer properties, and design life. Figure 5.8 shows FAARFIELD's design for $R = 700$ psi and reliability = 50% for a given base and subbase thickness determined with SOARP.

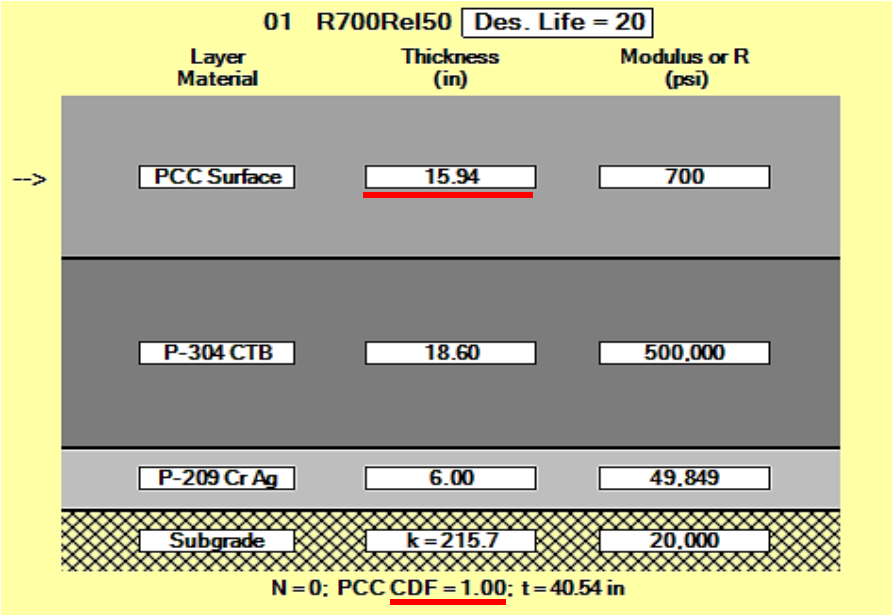

Figure 5.8 *FAARFIELD software's design thickness.*

Figure 5.9 compares the slab thickness calculated by FAARFIELD to that found by SOARP when flexural strength of the PCC slab is changed. Figures 5.9 (a) and 5.9 (b) display the PCC thickness corresponding to obtained reliabilities of 50% and 95%,

respectively. For a reliability of 50%, while FAARFIELD's designed PCC thicknesses is higher than those of SOARP's results except for $R = 800$. For a reliability of 95%, SOARP's optimal PCC thicknesses are higher than FAARFIELD's designed thicknesses. This suggests that if FAARFIELD's designed slab thickness is used in SOARP's framework the obtained reliability would likely be more than 50% and less than 95%. For example, when FAARFIELD's designed thickness of $d_1 = 15.9$ ($d_2 = 19$ and $d_3 = 6$) is used in 10,000 simulations of the SOARP, nearly 63% of them resulted in $TCDF <= 1.05$, corresponding to reliability of 0.63 (see Figure 5.9 (a)). Also, when FAARFIELD's designed slab thickness of $d_1 = 11.5$ ($d_2 = 30$ and $d_3 = 21$) is used for SOARP simulation, 70% of the simulations resulted in $TCDF <= 1.05$ (reliability = 0.7) (see Figure 5.9 (b)). It is indicating that FAARFIELD either recommends a more expensive design when there is a 50% reliability, or it recommends a design that does not achieve the 95% reliability. As the reliability increases, SOARP design tends to result in thicker PCC slabs than for FAARFIELD, and that the FAARFIELD's designed thickness very likely cannot withstand all of assumed conditions generated within the uncertain variables' ranges.

FAARFIELD does not include all the factors and uncertainty that SOARP considers. Also, FAARFIELD does not optimize over all three design parameters, but SOARP optimizes all three design parameters. By using ANN response models along with the Bayesian simulation optimization, the proposed SOARP method attempts to overcome some of the limitations from which current design methods suffer.

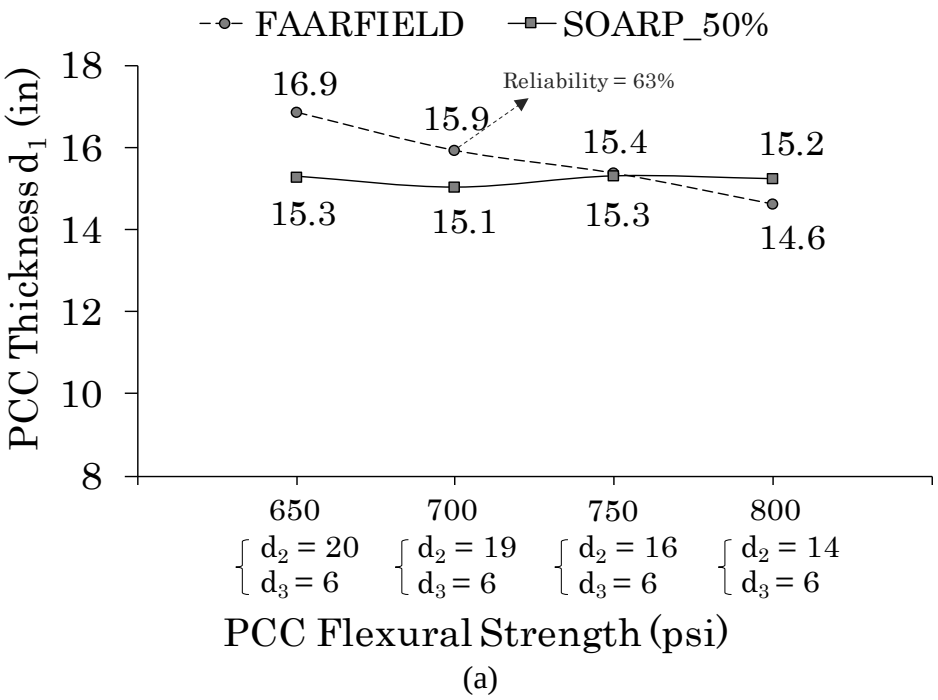

(a)

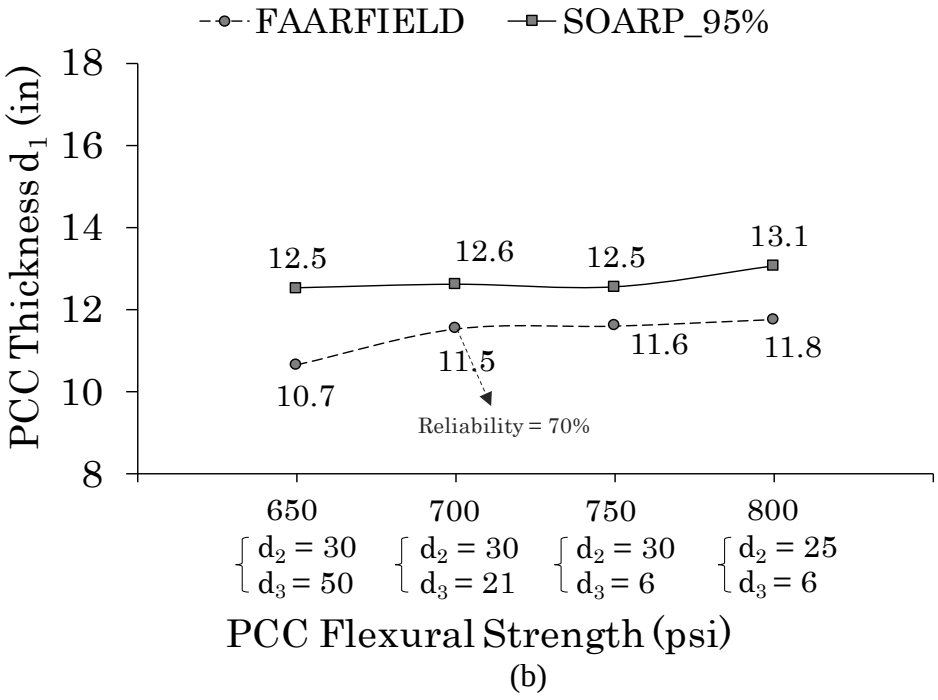

(b)

Figure 5.9 *Comparison of FAARFIELD results and SOARP (a) 50% reliability level (b) 95% reliability level for different flexural strength of the PCC.*

Summary and conclusions

This chapter describes the development of a comprehensive reliability-based simulation-optimization framework for finding the optimal design of airfield concrete pavement consisting of a nine-slab concrete pavement with base and subbase layers atop a subgrade. This study includes aircraft traffic consisting of a B747-8, a B787-8, an A340-500 opt, and an A340-600 opt. Thousands of scenarios were generated to simulate real-world conditions at for long-term usage of the assumed airfield. The design optimization was aimed at minimizing design cost while using a reliability constraint to keep pavement fatigue failure under an allowable amount. In this study ANNs were employed as analysis engines to replicate FEAFAA/NIKE3D-FAA pavement-response solution. Replicating critical stress responses associated with in airfield rigid pavement cracking would significantly make the design process more efficient by reducing total iteration time for calculation of critical responses for each type of aircraft in mixed-aircraft traffic loading.

The design optimization framework was optimized for multiple values of design life (20, 25, and 30 years) and multiple reliability levels (0.5, 0.8, 0.9, and 0.95). The results show that the expected design cost and optimal total thickness produced by 10,000 simulations of the inputs increased while the reliability level and design life increased. For a 80% reliability level and a 20-year design life, the expected cost is $12,310 per slab for a total thickness of 43.4, while for a 95% reliability level and 30-year design life, the total thickness is 49.7 in. It should be noted that by considering thousands of scenarios with uncertain inputs (e.g., loading position of the aircraft), and by estimating the critical stress level using ANN, the pavement structure with the calculated optimum thicknesses should withstand applied traffic and environmental loading during its design life without reaching the maximum fatigue damage level caused by the loading.

We also compared the optimal design found by SOARP with a FAARFIELD design that assumes default thicknesses for the base and subbase layers and then finds slab thickness using iteration, continuing the process until the CDF value becomes 1. In the SOARP framework, we first generated thousands of scenarios of pavement structure and loading conditions and calculated CDF values and an estimation of their distribution. By considering the uncertainty of inputs in CDF calculation, in contrast to FAARFIELD, a designer can simulate possible potential critical conditions. The results show that SOARP either results in more reliable or less expensive pavement designs.

References

[1] FAA, "150/5320-6F - Airport Pavement Design and Evaluation," U.S. Department of Transportation, Washington DC., 2016.

[2] A. Rezaei-Tarahomi, O. Kaya, H. Ceylan, K. Gopalakrishnan, S. Kim, and D. R. Brill, "Neural networks based prediction of critical responses related to top-down and bottom-up cracking in airfield concrete pavements," 2017.

[3] O. Kaya, A. Rezaei-Tarahomi, H. Ceylan, K. Gopalakrishnan, S. Kim, and D. R. Brill, "Developing Rigid Airport Pavement Multiple-Slab Response Models 2 for Top-Down Cracking Mode using Artificial Neural Networks 3," 2017.

[4] A. Rezaei-Tarahomi, O. Kaya, H. Ceylan, S. Kim, K. Gopalakrishnan, and D. R. Brill, "Development of rapid three-dimensional finite-element based rigid airfield pavement foundation response and moduli prediction models," Transp. Geotech., vol. 13, pp. 81–91, 2017.

[5] A. Rezaei-Tarahomi, H. Ceylan, K. Gopalakrishnan, S. Kim, O. Kaya, and D. R. Brill, "Artificial Neural Network Models for Airport Rigid Pavement Top-Down Critical Stress Predictions: Sensitivity Evaluation," in 2019 ASCE International Airfield and Highway Pavements Conference, 2019.

[6] A. Rezaei-Tarahomi, O. Kaya, H. Ceylan, K. Gopalakrishnan, S. Kim, and D. R. Brill, "Neural networks prediction of Critical Responses Related to Top-Down and Bottom-Up Cracking in Airfield Concrete Pavement," in 10th International Conference on the Bearing Capacity of Roads, Railways and Airfields, 2017.

[7] Gaurav, S. F. Wojtkiewicz, and L. Khazanovich, “Optimal design of flexible pavements using a framework of DAKOTA and MEPDG,” Int. J. Pavement Eng., vol. 12, no. 02, pp. 137–148, 2011.

[8] J. Santos and A. Ferreira, “Pavement design optimization considering costs and preventive interventions,” J. Transp. Eng., vol. 138, no. 7, pp. 911–923, 2011.

[9] J. Mikolaj, L. Remek, and M. Macula, “Asphalt Concrete Overlay Optimization Based on Pavement Performance Models,” Adv. Mater. Sci. Eng., vol. 2017, 2017.

[10] M. N. S. Hadi and Y. Arfiadi, “Optimum rigid pavement design by genetic algorithms,” Comput. Struct., vol. 79, no. 17, pp. 1617–1624, 2001.

[11] M. S. Mamlouk, J. P. Zaniewski, and W. He, “Analysis and design optimization of flexible pavement,” J. Transp. Eng., vol. 126, no. 2, pp. 161–167, 2000.

[12] M. Li, M. Sadoughi, C. Hu, Z. Hu, A. T. Eshghi, and S. Lee, “High-Dimensional Reliability-Based Design Optimization Involving Highly Nonlinear Constraints and Computationally Expensive Simulations,” J. Mech. Des., vol. 141, no. 5, p. 51402, 2019.

[13] M. Sadoughi, M. Li, and C. Hu, “Multivariate system reliability analysis considering highly nonlinear and dependent safety events,” Reliab. Eng. Syst. Saf., vol. 180, pp. 189–200, 2018.

[14] D. H. Timm and D. E. Newcomb, “Perpetual pavement design for flexible pavements in the US,” Int. J. Pavement Eng., vol. 7, no. 2, pp. 111–119, 2006.

[15] A. Noshadravan, M. Wildnauer, J. Gregory, and R. Kirchain, “Comparative pavement life cycle assessment with parameter uncertainty,” Transp. Res. Part D Transp. Environ., vol. 25, pp. 131–138, 2013.

[16] E.-B. Lee and C. W. Ibbs, “Computer simulation model: Construction analysis for pavement rehabilitation strategies,” J. Constr. Eng. Manag., vol. 131, no. 4, pp. 449–458, 2005.

[17] C. A. MacKenzie and C. Hu, “Decision making under uncertainty for design of resilient engineered systems,” Reliab. Eng. Syst. Saf., 2018.

[18] Y. Dinegdae, I. Onifade, B. Birgisson, R. Lytton, and D. Little, “Towards a Reliability-Based Pavement Design using Response Surface Methods,” Transp. Res. Rec., p. 0361198118783163, 2018.

[19] I. E. C. D. ARA, “Guide for Mechanistic-Empirical Design OF NEW AND REHABILITATED PAVEMENT STRUCTURES,” Transportation Research Board of the National Academies, Washington D.C., 2003.

[20] P. Dalla Valle, “Reliability in pavement design,” University of Nottingham, 2015.

[21] J. Q. Retherford and M. McDonald, “Reliability Methods Applicable to Mechanistic--Empirical Pavement Design Method,” Transp. Res. Rec., vol. 2154, no. 1, pp. 130–137, 2010.

[22] M. Sanchez-Silva, O. Arroyo, M. Junca, S. Caro, and B. Caicedo, “Reliability based design optimization of asphalt pavements,” Int. J. Pavement Eng., vol. 6, no. 4, pp. 281–294, 2005.

[23] D. R. Brill, Calibration of FAARFIELD Rigid Pavement Design Procdure. Federal Aviation Administration William J. Hughes Technical Center, 2010.

[24] I. Kawa, “Pass-to-Coverage Computation for Arbitrary Gear Configurations in the FAARFIELD Program,” 2012.

[25] FAA, “Airport Pavement Design and Evaluation. AC 150/5320-6F,” 2016.

[26] D. R. Brill and I. Kawa, “Advances in FAA Pavement Thickness Design Software: FAARFIELD 1.41,” in Airfield and Highway Pavements 2017, 2017, pp. 92–102.

[27] Z. Zhang et al., “Opening the black box of neural networks: methods for interpreting neural network models in clinical applications,” Ann. Transl. Med., vol. 6, no. 11, 2018.

[28] C. Thornton, F. Hutter, H. H. Hoos, and K. Leyton-Brown, “Auto-WEKA: Combined selection and hyperparameter optimization of classification algorithms,” in Proceedings of the 19th ACM SIGKDD international conference on Knowledge discovery and data mining, 2013, pp. 847–855.

[29] J. Snoek, H. Larochelle, and R. P. Adams, “Practical bayesian optimization of machine learning algorithms,” in Advances in neural information processing systems, 2012, pp. 2951–2959.

[30] D. J. Lizotte, Practical bayesian optimization. University of Alberta, 2008.

[31] E. Brochu, V. M. Cora, and N. De Freitas, “A tutorial on Bayesian optimization of expensive cost functions, with application to active user modeling and hierarchical reinforcement learning,” arXiv Prepr. arXiv1012.2599, 2010.

[32] P. I. Frazier, “A tutorial on Bayesian optimization,” arXiv Prepr. arXiv1807.02811, 2018.

[33] A. Klein, S. Falkner, S. Bartels, P. Hennig, and F. Hutter, “Fast bayesian optimization of machine learning hyperparameters on large datasets,” arXiv Prepr. arXiv1605.07079, 2016.

[34] Z. Wang, M. Zoghi, F. Hutter, D. Matheson, and N. De Freitas, “Bayesian optimization in high dimensions via random embeddings,” in Twenty-Third International Joint Conference on Artificial Intelligence, 2013.

[35] W. S. P. | P. Brinckerhoff, “Bid Tabulation for Reconstruction of Runway 13-31 Phase 1,” 2016.

CHAPTER 6. CONCLUSIONS, RECOMMENDATIONS AND CONTRIBUTIONS OF THIS STUDY

Conclusions

Through sensitivity analysis, influence of critical input parameters on 3D finite-element (FE) simulation outputs were identified. For simultaneous temperature and mechanical loading conditions, the five most effective parameters related to top tensile stresses are Portland cement concrete (PCC) thickness, PCC modulus, thermal coefficient, temperature gradient, and base thickness. With respect to combined loading conditions, PCC slab properties and the temperature inputs make the greatest contribution, while with respect to mechanical loading, only the PCC slab properties and sublayer thickness variation make a significant contribution to advancement of top-down cracking.

An automation process was devised for database development, artificial neural networks (ANN) training, and exporting and using the models, and, finally, a program for rapid analysis of the rigid pavements was proposed. The proposed program, called ANNFAA, is used for utilizing models developed for all aircraft. ANNFAA can predict critical tensile stresses for 1 million cases in 6 to 16 seconds, while analyzing the same cases using 3D FE simulation would take several weeks.

For ANN model accuracy assessment, independent testing and sensitivity analysis were conducted for each model, and those exhibiting the best performance in independent testing were selected as optimum models. Sensitivity analysis was then conducted to assure accuracy and generalization capability of the models. Accuracy assessments showed that ANN models predict top tensile stress responses reasonably well, and they can significantly help with analyzing top-down cracks by predicting the most critical associated stress responses. Sensitivity analysis also determined effective parameters for both FE solutions

and ANN models, with results that exhibited a perfect match between the most effective parameters obtained by the FE solutions and those from the ANN models.

Finally, a comprehensive simulation-optimization framework was developed to determine the optimal design of a specific type of airfield concrete pavement. a nine-slab concrete pavement with base and subbase layers atop a subgrade. The design optimization was aimed at minimizing design cost while pavement fatigue failure remains under an allowable amount controlled by a reliability constraint. In this design method, trained ANN models have been used as analysis engines to replicate a pavement's bottom-up critical stress for a given aircraft traffic mix. Monte Carlo simulation generated 10,000 samples using the given design factors, and ANN was used for predicting critical stresses for all the samples. A total cumulative damage factor (TCDF) was calculated for the samples, while attempting to find the optimum design with minimum cost that met the reliability constraint. The results show that the expected design cost and optimal total thickness resulting from 10,000 simulations of the inputs increases along with both the reliability level and the design life.

Recommendations

Based on the results of this study, the following recommendations for enhancing various aspects of existing rigid airfield pavement structural design methodology in pursuance of an extended pavement life design concept (from 20 to 40 years) are made:

Since next-generation rigid airport pavement design procedures are expected to account for both top-down failure mode and bottom-up cracking failure mode, they should reflect validated failure equations that would differ depending on whether top-down or bottom-up cracking is driving thickness design as it evolves toward more fully mechanistic-empirical design.

To predict cracks, determining the locations of the most critical stresses for top-down and bottom-up cracking modes for each gear type would obviously be very helpful, and ANN models are recommended for that purpose.

Bottom-up bending stresses currently considered in pavement design practices represent an important type of response to be considered in future studies aimed at developing ANN-based surrogate response models for prediction of such stresses. Rather than using pre-determined load locations (as is done in current design methodology) and calculating design stress based on them, ANN response models can be utilized for predicting critical locations by placing a mechanical load on one of several potentially-critical load locations, allowing maximum stresses to be automatically calculated on both slab top and bottom, with the values obtained to be used as design stresses.

Determination of foundation responses such as vertical deflection and vertical stresses on top of base and subgrade layers, that make significant contribution to pavement deflection and distresses, could become an active field of research for developing surrogate response models for predicting critical foundation responses.

While FAARFIELD represents one crucial structural design aspect, there are other aspects of integrated design procedures that potentially should be modified to achieve an extended-life design concept. For example, the BAKFAA structural evaluation back-calculation tool currently uses layered elastic analysis in its iterative forward calculation routine. To further enhance the computational efficiency of the entire inverse analysis process, the feasibility of developing and implementing Artificial Intelligence (AI)-based models (using ANN and/or evolutionary optimization) for airfield concrete pavement back-calculation analysis should be investigated.

Considering the various sources of uncertainty in the rigid-pavement design process, the feasibility of integrating reliability into the design using reliability-based design optimization also should be investigated.

Design engineers often criticize ANNs as comprising a black-box model that doesn't directly allow for physical understanding and interpretation. ANNs typically don't produce practical prediction equations, they have complex structure, and they are prone to over-fitting. Genetic Programming (GP) is a systematic, domain-independent evolutionary computation technique that stochastically evolves populations of computer programs to perform a user-defined task. Similar to Genetic Algorithms (GA) that evolve a population of individuals into better versions, GP iteratively transforms a population of computer programs into a new generation of programs by applying biologically-inspired operations such as crossover, mutation, etc. It has been shown that prediction models evolved through GP are reasonably compact and contain both linear terms and low-order non-linear transformations of input variables for simplification. In other words, the greatest advantage of GP would be that a final prediction model is transparent in that it can be represented in the form of a regression equation capable of being directly plugged into a larger computational pipeline. However, transparency of GP based models often comes at the cost of loss of accuracy, and this should be investigated, along with investigating the feasibility of developing transparent surrogate response prediction models (using GP) for determining top-down and bottom-up cracking modes in rigid airport pavement.

Contributions

The demand for high quality pavement capable of withstanding loads produced by the new generation of heavy aircraft with minimum deterioration and longer service life justifies the need for more advanced pavement analysis and design techniques. This study will

contribute greatly to the methodology of using new AI approaches in pavement analysis and design, so that engineers applying the proposed methods of this study will be able to more quickly analyze complex pavement structures and design better pavements. The following is a summary of this study's key contributions:

3D FE Simulation Database

I created a comprehensive database from hundreds of thousands of 3D FE simulations of airfield rigid pavement. This database, that includes much valuable information, including critical stress and strain responses, deflections, and their locations for all Airbus and Boeing airplane landing gear loadings, will help researchers and engineers in future study of complex rigid pavement structures.

Critical Response Predictions

Artificial intelligence (AI)-based alternatives such as ANN have been proposed to replace 3D-FE models by producing sufficiently accurate pavement response predictions needed for top-down cracking analysis in a small fraction of the time required for FE modeling. Previous ANN success in predicting pavement responses has been well-documented and, specifically, successful ANN prediction of pavement responses associated with top-down cracking in rigid airfield pavements has been proven.

A new ANN-based FAA rigid-pavement analysis tool (ANNFAA), provides very powerful, useful, fast, and easy-to-use utility for researchers and engineers to use in prediction of the most critical stresses in an airfield rigid pavement and for a specific aircraft loading.

Future studies can use the outcomes of this research for development and inclusion of a protocol/framework with steps specifying how top stress should be considered in determining final slab thickness.

Integrated ANN-Simulation Optimization Design

By using ANN response models along with Bayesian simulation optimization, the proposed simulation optimization for airfield rigid pavement design (SOARP) method attempted to resolve some of the limitations that burden current design methods. Considering different reliability levels in the pavement design optimization enables decision-makers to determine optimal design options including different expected costs of design, and to choose the particular design that satisfies their budget constraints and their risk-aversion needs. This framework empowers designers with a comprehensive reliability-based simulation-optimization framework for critical stress-response prediction that benefits from AI. This method can determine optimal design of a complex nine-slab pavement with significant time reduction.

This study should contribute to making pavement design and analysis more practical, especially when a significantly large number of different cases that include aspects like top-down cracking failure mode are investigated, as well as when bottom-up cracking mode, currently used in the FAA standard rigid pavement design procedures, is being considered.